

ON THE STRUCTURE OF LITHIUM AND STRONTIUM BORATE
GLASSES MODIFIED WITH YTTRIUM AND RARE-EARTH CATIONS
INVESTIGATED BY VIBRATIONAL SPECTROSCOPY

BY

BRIAN TOPPER

A THESIS
SUBMITTED TO THE FACULTY OF

ALFRED UNIVERSITY

IN PARTIAL FULFILLMENT OF THE REQUIREMENTS
FOR THE DEGREE OF

MASTER OF SCIENCE

IN

MATERIALS SCIENCE AND ENGINEERING

ALFRED, NEW YORK

NOVEMBER, 2020

ON THE STRUCTURE OF LITHIUM AND STRONTIUM BORATE
GLASSES MODIFIED WITH YTTRIUM AND RARE-EARTH CATIONS
INVESTIGATED BY VIBRATIONAL SPECTROSCOPY

BY

BRIAN TOPPER

B.S. UNIVERSITY OF RICHMOND (2015)

SIGNATURE OF AUTHOR _____

APPROVED BY _____

DORIS C. MÖNCKE, ADVISOR

ALEXIS G. CLARE, ADVISORY COMMITTEE

SCOTT MISTURE, ADVISORY COMMITTEE

EFSTRATIOS I. KAMITSOS, ADVISORY COMMITTEE

STEVEN C. TIDROW, ORAL THESIS DEFENSE

ACCEPTED BY _____

GABRIELLE G. GAUSTAD, DEAN
KAZUO INAMORI SCHOOL OF ENGINEERING

Alfred University theses are copyright protected and may be used for education or personal research only. Reproduction or distribution in part or whole is prohibited without written permission from the author.

Signature page may be viewed at Scholes Library, New York State College of Ceramics, Alfred University, Alfred, New York.

ACKNOWLEDGMENTS

To my grandparents, Patricia and Joseph Topper, who made it possible to begin graduate study at Alfred University.

Thanks go out to those that helped make this work possible: Dr. William LaCourse, Dr. Alexis Clare, Dr. Scott Misture, Jim Thiebaud, Dr. Darren Stohr, Dr. Andreas Herrmann, Sahar Mohktari, Charles Bellows, Dr. Konstantinos Chatzipanagis, Dr. Randall Youngman, Dr. Jesse Kohl, , and Dr. Matthew Trawick.

Special thanks goes out to the Bernstein Family whose generosity helped make possible a month of study in Athens, Greece at the *Theoretical and Physical Chemistry Institute (TPCI)* of the *National Hellenic Research Foundation (NHRF)* under the tutelage of Dr. E.I. Kamitsos.

Special thanks to Stratos Kamitsos for perhaps the most dense, formative experience of my graduate studies so far. And enormous gratitude is owed to Nagia Tagiara, for patiently training and working with me daily while at NHRF as well as providing some samples and measurements used in this work.

To Dr. Doris Möncke- your enthusiasm, spirit, and vast knowledge are beyond inspiring. For your patience in my absent chemistry background to helping support a month of study abroad. For your open door and the long discussions that follow to your encouragement to live a balanced life. My gratitude for your support and reassurance cannot be stated adequately.

TABLE OF CONTENTS

	Page
<i>Acknowledgments</i>	<i>iii</i>
<i>Table of Contents</i>	<i>iv</i>
<i>List of Tables</i>	<i>vii</i>
<i>List of Figures</i>	<i>viii</i>
<i>List of Schematics</i>	<i>xii</i>
<i>List of Images</i>	<i>xiv</i>
<i>Abstract</i>	<i>xv</i>
I. INTRODUCTION	1
 Chapter 1 - "Background: Structure and Properties of Borate Glasses"	
Abstract.....	5
1. INTRODUCTION.....	6
2. BORON OXIDE GLASS.....	8
2.1. GENERAL PROPERTIES OF PURE VITREOUS B ₂ O ₃	8
2.2. VIBRATIONAL SPECTROSCOPY	10
2.3. NMR SPECTROSCOPY.....	12
3. MODIFIED BORATE GLASSES	13
3.1. THE BORON OXIDE ANOMALY	13
3.2. DEPOLYMERIZATION OF THE BORATE NETWORK.....	19
4. BINARY GLASS FORMING BORATES	21
4.1. MONOVALENT MODIFIER, M ₂ O	21
4.2. DIVALENT MODIFIER, MO	22
4.3. TRIVALENT MODIFIER, M ₂ O ₃ (M = AL, BI, REE)	25
5. TEMPERATURE DEPENDENCE OF THE BORATE MELT STRUCTURE	27
6. THE METAL CATION ENVIRONMENT	29
7. NON-OXYGEN ANIONS IN BORATE GLASSES.....	33
8. SECOND BORON ANOMALY.....	34
CONCLUSION.....	35

Chapter 2 - "A Quest for Tetrahedral Orthoborate Units in Glasses"

1.	HYPOTHESIS.....	37
2.	EXPERIMENTAL.....	38
	2.1. MATERIALS.....	38
	2.1.1. REFERENCE MATERIALS.....	38
	2.1.2. LITHIUM YTTRIUM BORATE GLASSES (LYB).....	38
	2.1.3. STRONTIUM YTTRIUM BORATE GLASSES (SYB).....	38
	2.1.4. $45 \text{ Li}_2\text{O} - 20 \text{ R}_2\text{O}_3 - 35 \text{ B}_2\text{O}_3$ (LRB).....	40
	2.2. METHODS.....	41
	2.2.1. X-RAY DIFFRACTION.....	41
	2.2.2. VIBRATIONAL SPECTROSCOPY.....	41
	2.2.2.1. RAMAN SPECTROSCOPY.....	41
	2.2.2.2. INFRARED REFLECTANCE SPECTROSCOPY.....	45
	2.2.3. DIFFERENTIAL SCANNING CALORIMETRY.....	47
	2.2.4. TIME-DEPENDENT FLUORESCENCE SPECTROSCOPY.....	48
	2.3. SOFTWARE.....	49
3.	RESULTS.....	50
	3.1. ORTHOBORATE REFERENCE MATERIALS.....	50
	3.1.1. X-RAY DIFFRACTION.....	50
	3.1.2. RAMAN SPECTROSCOPY.....	50
	3.1.3. INFRARED SPECTROSCOPY.....	51
	3.2. LITHIUM YTTRIUM BORATES (LYB).....	52
	3.2.1. LYB SAMPLES WITH CONTAMINATED LITHIUM CARBONATE.....	52
	3.2.2. LYB GLASSES.....	57
	3.3. LYB SAMPLES WITH CONTAMINATED LITHIUM CARBONATE.....	61
	3.3.1. STRONTIUM EUROPIUM ORTHOBORATE (SEB).....	61
	3.3.2. STRONTIUM YTTRIUM BORATES (SYB).....	63
	3.3.3. OVERMODIFIED STRONTIUM YTTRIUM BORATES (OM-SYB).....	67
	3.4. ORTHOBORATE $\text{Li}_2\text{O} - \text{R}_2\text{O}_3 - \text{B}_2\text{O}_3$ (LRB).....	69
4.	DISCUSSION.....	71
	4.1. LITHIUM YTTRIUM BORATES.....	71
	4.2. STRONTIUM YTTRIUM BORATES.....	72
	4.2.1. BORATE NETWORK – RAMAN SPECTROSCOPY.....	72
	4.2.2. BORATE NETWORK – INFRARED SPECTROSCOPY.....	76
	4.2.3. METAL CATIONS – VIBRATIONAL SPECTROSCOPY.....	79

4.3. OVERMODIFIED STRONTIUM YTTRIUM BORATES	81
4.4. ORTHOBORATE $\text{Li}_2\text{O} - \text{R}_2\text{O}_3 - \text{B}_2\text{O}_3$	81
5. CONCLUSION	83
6. OUTLOOK.....	84
7. REFERENCES	85
APPENDIX	93
A1. INFORMAL DERIVATION OF RAMAN INTENSITY EXPRESSION	93
A2. GLASS TRANSITION TEMPERATURE DETERMINATION IN SYB GLASSES.....	96
A3. CONTAMINATION OF Li_2CO_3	101
A4. IR SPECTRA OF GLASSES WITH CONTAMINATED Li_2CO_3	109

LIST OF TABLES

	Page
Chapter 1	
Table 1. Some Properties of Boron Oxide Glass and Modified Borate Glasses.....	9
Chapter 2	
Table 2. Composition and Preparation Parameters for Strontium-Yttrium-Borate Glasses.....	39
Table 3. Composition and Preparation Parameters for Overmodified Strontium-Yttrium-Borate Glasses, with X=33 and 30.....	40

LIST OF FIGURES

		Page
Chapter 1		
Figure 1.	Absorption coefficient spectrum (top) and Raman spectrum (bottom) for pure boron oxide glass obtained from melting B ₂ O ₃ at 1200 °C for 15 minutes in a platinum crucible.....	11
Figure 2.	¹¹ B NMR spectrum of modified borate glass displaying the convoluted trigonal boron band and its separation from the tetrahedral boron band.....	13
Figure 3.	Short range and intermediate range order borate units with all bridging oxygens.....	15
Figure 4.	Anomalous trends in physical properties of borate glasses as a function of modifier content expressed as molar ratio, R, the ratio of M ₂ O (or MO) content to B ₂ O ₃ content- (top) glass transition temperature over the range of the anomalous behavior, (middle) coefficient of thermal expansion, and (bottom) isothermal viscosity at 1073 K. In the top and bottom figure, the fitted lines are guides for the eyes only.....	16
Figure 5.	Four-coordinated boron and glass transition temperature for binary lithium borate glasses. N ₄ fraction (left axis) determined by NMR (data from Kroeker (squares) and Yun (triangles)), Equation 1 (solid black line), T _g Experimental from Feller and Affatigato (open circles), and T _g Model from Takeda (solid red line).....	18
Figure 6.	SRO and IRO borate units containing non-bridging oxygens.....	20
Figure 7.	Temperature dependence on the fraction of four-coordinated boron, determined by Raman spectroscopy, in (x) Na ₂ O - (1-x) B ₂ O ₃ glasses for x=15 mol% (squares, R=0.18), x=20 mol% (circles, R=0.25), and x=25 mol% (triangles, R=0.33).....	28

Figure 8.	Force constant versus glass transition temperature for varying modifier types in borate glasses. Some 50 MO – 50 B ₂ O ₃ (metaborates) and 20 M ₂ O – 80 B ₂ O ₃ (tetraborates).....	30
Figure 9.	Infrared absorption coefficient spectra for the lithium borate system. Arrow drawn to bring attention to the increasing frequency of the lithium ion motion band.....	32
 Chapter 2		
Figure 2-1.	As measured Raman spectra, offset for clarity.....	43
Figure 2-2.	Normalized Raman spectra offset for clarity.....	43
Figure 2-3.	Yttrium oxide free, 47 SrO – 53 B ₂ O ₃ normalized Raman spectrum (top) and first derivative (bottom) with dashed lines indicating band positions in normalized spectrum corresponding to the positions where the first derivative is equal to zero.....	44
Figure 2-4.	25 Y ₂ O ₃ – 37.5 SrO – 37.5 B ₂ O ₃ normalized Raman spectrum (top) and first derivative (bottom) with dashed lines indicated band positions in normalized spectrum corresponding to the positions where the first derivative is equal to zero.....	44
Figure 2-5.	Example of FIR extrapolation required for KK transformation.....	46
Figure 2-6.	Comparison of the reflectance spectrum (bottom) and the obtained absorption coefficient spectrum after KK transformation.....	47
Figure 2-7.	Example of intercept method applied to first endotherm in the measured heat flow.....	48
Figure 2-8.	Fluorescence lifetime set-up by Andreas Herrmann.....	49
Figure 3-1.	X-Ray diffraction data of prepared polycrystalline orthoborates.....	50
Figure 3-2.	Raman spectra of prepared polycrystalline orthoborates.....	51
Figure 3-3.	Infrared absorption coefficient spectra of prepared polycrystalline orthoborates.....	52
Figure 3-4.	X-Ray diffraction results for glasses containing an increasing amount of yttrium oxide.....	53

Figure 3-5.	Glass transition temperature of glasses plotted versus nominal Y_2O_3 content.....	54
Figure 3-6.	Raman spectra of spots in Image 1 with respect to YBO_3 reference compound spectra.....	56
Figure 3-7.	Raman spectra of spots in Image 1 with borate units identified.....	56
Figure 3-8.	Raman spectra of lithium yttrium borate glasses and their crystallization encountered during quenching compared to $LaBO_3$ and YBO_3 reference material spectra.....	58
Figure 3-9.	IR absorption coefficient spectra of lithium yttrium orthoborate glasses compared to $LaBO_3$ reference compound.....	59
Figure 3-10.	Raman spectra of lithium yttrium orthoborate glasses compared to $LaBO_3$ reference compound.....	60
Figure 3-11.	Spectra of strontium europium orthoborates melted under different atmospheric conditions and in different crucibles.....	62
Figure 3-12.	Normalized Raman spectra of strontium yttrium borate glasses.....	63
Figure 3-13.	Normalized infrared absorption coefficient spectra of strontium yttrium borate glasses.....	64
Figure 3-14.	Differential scanning calorimetry data for strontium yttrium borate glasses over the range 500-1000 °C.....	66
Figure 3-15.	Differential scanning calorimetry data for strontium yttrium borate glasses over the range 600-700 °C.....	67
Figure 3-16.	Raman spectra of overmodified strontium yttrium borates.....	68
Figure 3-17.	Infrared spectra of overmodified strontium yttrium borates.....	69
Figure 3-18.	Raman spectra of 45 Li_2O – 20 R_2O_3 – 35 B_2O_3 orthoborates.....	70
Figure 3-19.	Infrared spectra of 45 Li_2O – 20 R_2O_3 – 35 B_2O_3 orthoborates.....	70
Figure 3-20.	Fluorescence decay of Tb^{3+} doped Li_2O – R_2O_3 – B_2O_3 samples.....	71
Figure 4-1.	Overlapped normalized Raman spectra of Strontium Yttrium Borate glasses.....	73
Figure 4-2.	Raman spectra, overlapped and normalized, of Strontium Yttrium Borate glasses over the interval 400 – 800 cm^{-1}	73

Figure 4-3.	Raman spectra of Strontium Yttrium Borate glasses over the interval 770 – 1050 cm ⁻¹	74
Figure 4-4.	Raman spectra of Strontium Yttrium Borate glasses over the interval 1075 – 1550 cm ⁻¹	75
Figure 4-5.	Overlapped Infrared absorption coefficient spectra of Strontium Yttrium Borate glasses.....	76
Figure 4-6.	Tetrahedral boron IR band in Strontium Yttrium Borates.....	77
Figure 4-7.	A ₄ vs A ₃ in Infrared spectra of Strontium Yttrium Borate Glasses shown over 800-1650 cm ⁻¹	78
Figure 4-8.	Plot of A ₄ vs Y ₂ O ₃ content of Strontium Yttrium Borate Glasses. Line is drawn as a guide for the eye.....	78
Figure 4-9.	Cation motion bands in Strontium Yttrium Borate glasses.....	79
Figure 4-10.	Plot of apparent (combined Sr ²⁺ /Y ³⁺) cation motion band maximum vs Y ₂ O ₃ content. Line is drawn as a guide for the eye.....	80
Figure 4-11.	Low frequency range (100-400 cm ⁻¹) of the Raman spectra for Strontium Yttrium Borate glasses.....	80
Figure A-1.	T _g SYB with 5 mol% Y ₂ O ₃	96
Figure A-2.	T _g SYB with 10 mol% Y ₂ O ₃	97
Figure A-3.	T _g SYB with 15 mol% Y ₂ O ₃	97
Figure A-4.	T _g SYB with 20 mol% Y ₂ O ₃	98
Figure A-5.	T _g SYB with 25 mol% Y ₂ O ₃	98
Figure A-6.	First derivative of DSC signal for SYB glasses.	100
Figure A-7.	Plot of different T _g values in strontium yttrium borate glasses. Error of +/- 3 °C displayed on ‘onset’ data points.....	101
Figure A-8.	Back Scatter image of the contaminated lithium carbonate raw material. The grey spots are lithium carbonate and the white spots are an impurity.....	102
Figure A-9.	Location of Figure A-8 with increased contrast to show impurity population.....	103
Figure A-10.	SEM image of one of the larger impurities seen in Figure A-8.....	103
Figure A-11.	Back Scatter image of typical contaminant (lithium carbonate is grey)...	104

Figure A-12. EDS Site - Spot 1 and 2 are on one of the 'bright spots' observed in Figure A-11. Spots 3 and 4 are on the bulk of the material.....	104
Figure A-13. EDS spectra for impurity site. EDS was performed on multiple spots and multiple sites) all showing the same elements of Si, O, Ba, Na.....	105
Figure A-14. EDS spectra for the majority of the material. The presence of only carbon and oxygen are taken as indication that this represents a lithium carbonate site.....	105
Figure A-15. Spots for EDS in LYB with nominal composition 57 Li ₂ O - 12 Y ₂ O ₃ - 31 B ₂ O ₃	106
Figure A-16. All three spots had an EDS spectrum as the one shown above. The program quantified the atomic percentage of the impurities as Na= ~1%, Ba = 0.1%, Si = ~2-2.5%. Keep in mind the lithium content is not taken into consideration and no standards were prepared for this analysis.....	106
Figure A-17. Spots for EDS in LYB glass with nominal composition 48 Li ₂ O - 18 Y ₂ O ₃ - 34 B ₂ O ₃	107
Figure A-18. All three spots had an EDS spectrum as the one shown above. The quantified impurity concentrations were slightly lower than the glass in Fig A-16 & A-16 which agrees with the lower Li ₂ CO ₃ used in preparation of the glass. Additionally, a trace amount of aluminum was observed, on the order of 0.1 atomic%.....	107
Figure A-19. YBO ₃ crystalline compound for EDS. Closer investigations revealed the material to be homogenous. There was a small population of structures that appeared different than the bulk population. EDS at these locations showed the same spectra as the bulk so it was concluded these apparently different sites were YBO ₃ with trigonal structure. Indeed, an NMR measurement of the material quantified about 5% of the borate units to be trigonally configured.....	108
Figure A-20. EDS spectra that appeared at all spots investigated. No contaminants present- only B, O, and Y were detected at multiple sites. The boric acid and yttria used in the preparation of this compound were the same as	

	used for the glasses.....	108
Figure A-21.	IR spectra of contaminated LYB glasses.....	109
Figure A-22.	IR spectra of binary lithium borate glasses from Kamitsos.....	110
Figure A-23.	IR spectra of a series of LYB glasses with constant Y ₂ O ₃ in the nominal composition.....	111
Figure A-24.	IR spectra of a series of LYB glasses with constant Y ₂ O ₃ in the nominal composition shown over the range 800-1200 cm ⁻¹	112

LIST OF SCHEMATICS

	Page
Schematic 1. Fundamental borate units - trigonal or three-fold coordinated boron (left) for boron with sp ² electron configuration and tetrahedral or four-fold coordinated boron (right) for boron with sp ³ electron configuration for the highest degree of polymerization. Non-bridging oxygen ions can form on either units in crystals, though glasses favor nbO formation on the trigonal unit.....	7
Schematic 2. H ₂ O reacting with a borate network segment to form hydroxyl groups bonded to boron atoms.....	10
Schematic 3. Conversion of two trigonal borate units into two tetrahedral borate units after the addition of one unit of alkali oxide.....	14
Schematic 4. Isomerization between a single trigonal unit and single tetrahedral unit at the orthoborate stoichiometry.....	21
Schematic 5. Bi-diborate poly-anion found in crystalline 6 PbO – 5 B ₂ O ₃	24
Schematic 6. [B ₅ O ₁₁] ⁷⁻ poly-anion present in bismuth borate crystals and possibly glasses.....	26
Schematic 7. Disproportionation of several orthoborate triangles into the pyroborate unit and the isolated BO ₄ ⁵⁻ unit.....	33
Schematic 8. Equilibrium of orthoborate triangles with the orthoborate ring composed of tetrahedral borates.....	35

LIST OF IMAGES

	Page
Image 1 (a – f). Spots of partially crystallized glass corresponding to locations that the Raman spectra in Figure 3-6 and Figure 3-7 were recorded at.....	55

ABSTRACT

The thesis begins with a comprehensive review of the structure and properties of borate glasses. This is followed by a predominantly qualitative assessment of highly modified lithium and strontium borates containing yttrium and rare-earth oxide additions that have been prepared by the traditional melt-quenching technique. To the author's knowledge, reports on the ternary glasses studied here are not available in the literature. The feasibility of glass formation for these new compositions is discussed and the structures of the resulting materials have been studied, primarily, with vibrational spectroscopy as well as selectively with differential scanning calorimetry, X-Ray diffraction, and time-resolved fluorescence spectroscopy.

Raman and Infrared spectroscopies suggest the glasses formed in the vicinity of the orthoborate stoichiometry are structurally similar to the high temperature phase of the related yttrium or rare-earth orthoborate crystals, regardless of whether the glass transition temperature lies above or below the corresponding phase transformation temperature. A relationship between the crystal phase transformation temperature and the glass transition temperature has been observed through the partial devitrification of borate melts containing relatively high yttrium content. That is, for glasses where the glass transition temperature is above the phase transformation temperature, only short-range order structural units akin to the high temperature phase will be present in both the glass and any crystallization products. For glasses where the glass transition temperature is below the phase transformation temperature, the bulk glass is also made up of the short-range order structural units found in the high temperature phase; however, low temperature phase crystallites are detected with XRD. These crystallites, comprised only of tetrahedral orthoborate units arranged in B_3O_6 rings, are seen also as well-defined structures approximately 30 microns in diameter using confocal Raman microscopy.

The addition of oxides with the high field strength trivalent yttrium ion to strontium borate glasses was found to depolymerize the borate network into ionic species while simultaneously increasing the glass transition temperature. In this series, the increase of the cation motion band frequency from 180 cm^{-1} to 323 cm^{-1} indicates the trivalent yttrium ions form stronger bonds with network oxygen than the divalent strontium ions. This correlates with the onset of the glass transition temperature increasing non-linearly from $630.7\text{ }^\circ\text{C}$ to $652.2\text{ }^\circ\text{C}$ for glasses containing 5 mol% and 25 mol% Y_2O_3 , respectively.

Lithium yttrium/rare-earth orthoborate glasses were found to consist solely of isolated trigonal borate units and to be insensitive to the use of either yttrium or other rare-earth

elements, all of which have a well-known tetrahedral orthoborate crystalline phase. The absence of isomerization or disproportionation at the orthoborate stoichiometry implies the driving mechanism for glass formation in these glasses can be viewed as having a physical rather than chemical origin. This is to say, vitrification is dependent on the freezing-in of highly distorted, isolated trigonal borate structures - which are favored at high temperatures and in the melt compared to their tetrahedral counterpart.

Several of the lithium yttrium/rare-earth orthoborate glasses were doped with Tb^{3+} and the measured lifetime of the 543 nm emission using 375 nm excitation was ~ 2.2 ms. Measured lifetime decays, in conjunction with the relevant literature, suggest that even if trivalent rare-earth cations are present in small quantities, in a partially or fully depolymerized borate glass, the Tb^{3+} ions will seek out local sites whose short range order corresponds to that of the high temperature crystalline phase. Indeed, this observation is in excellent agreement with the qualitative Raman interpretation of bulk strontium yttrium borate glasses where the introduction of the small quantities of Y_2O_3 is seen to induce the formation of trigonal orthoborate units below the pyroborate stoichiometry. Overall, the results obtained from the Tb^{3+} doped orthoborate glasses here permit interpretation of previously unexplained published results. This is framed in the context of experimental and computational results pertaining to alkali and alkaline-earth borates that show that metal cations with high field strength will determine their local environment to a greater degree than metal cations present whose field strength is lower.

I. INTRODUCTION

This thesis has two parts. First, a general review on the structure and properties of borate glasses that was compiled to be a book chapter in “Phosphate and Borate Bioactive Glasses; Biomaterials Science Series” to be published by The Royal Society of Chemistry (“the RSC”). Second is the experimental quest for tetrahedral orthoborate units in glasses.

The review details first the structure and properties of pure boron oxide glass, which from the 1930s to the 1990s remained the subject of continuous debate. After establishing the framework for glassy B_2O_3 the effect of modifier oxides is looked at in depth. This brings about a discussion on the most striking feature of borate glasses, *The Boron Oxide Anomaly*, the phenomena whereby the coordination of boron changes from three (3) to four (4) with the introduction of a modifier to pure boron oxide. The variables impacting the equilibrium that governs the change in coordination arising from experimental evidence, empirical models, and theoretical considerations are discussed.

The resulting structure, both short range (<0.5 nm) and intermediate range (0.5-2 nm), that have been determined by spectroscopic and diffraction methods applied to borate crystals, glasses, and melts over the past century are discussed in the context of our current understanding of many binary borate glasses. Examples are given of how the borate network structures and connectivity correlate with physical and thermal properties.

The experimental quest for tetrahedral orthoborate glasses is primarily motivated by fundamental scientific curiosity. There is an extensive library of work on pure boron oxide and glasses modified to the metaborate stoichiometry. This has likely stemmed from this region of composition space being most relevant to current uses of boron oxide containing glasses. Indeed, the technical advantages of

borosilicate glasses have been known for over 100 years, but structural investigations and models are still conducted and put forth to this day.

Much less attention has been paid to the highly modified and invert borate glasses. Some systems have attracted attention for specific applications such as fast ion conducting or optically active glasses. Others have been looked at by workers dedicated to the understanding of borate glasses. Many remain unexamined, due to the limitations imposed by time and funding.

Fortunately, the pursuit of basic glass science is made possible by the New York State College of Ceramics at Alfred University.

“The scientist does not study nature because it is useful; he studies it because he delights in it, and he delights in it because it is beautiful.” – Henri Poincaré

Dedicated to the Memory of Dr. Cornelius Beausang,

“Glass! That’s exciting!” - Con

Chapter 1

Background:

Structure and Properties of Borate Glasses

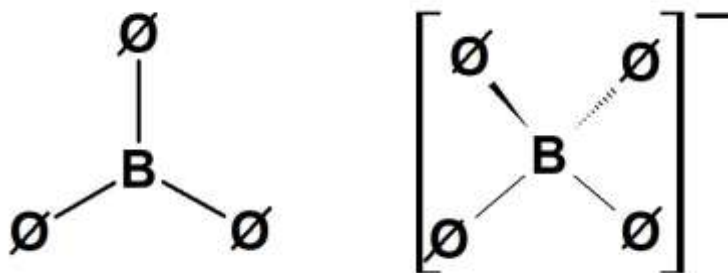
Abstract

The role of boron oxide in glass science is broad, spanning from borate glasses used as bioactive materials, sealing agents, dosimeters, and radiation shielding glasses - to an additive in chemically durable or nuclear waste immobilizing borosilicate glasses. The structure of borate glasses from pure boron oxide glass up to highly modified compositions is discussed in this chapter, covering the full range of borate chemical structures in glasses and melts. The *boron anomaly*, the conversion of trigonal borate units to tetrahedral borate units, is introduced and the impact this has on the structure and properties of modified borate glasses is outlined. The factors influencing the equilibrium between three and four coordinated boron, such as modifier type and quantity, synthesis temperature, as well as the number of non-oxygen anions are looked at to demonstrate the highly tunable nature of borate glasses for diverse applications.

1. Introduction

Boron oxide is one of the classic glass formers along with silicon dioxide and phosphorous pentoxide – and a couple of less common glass forming oxides such as GeO_2 or TeO_2 . Boron atoms in B_2O_3 have the electronic configuration $1s^2 2s^2 2p^1$. Most boron compounds are not following the octet rule. In boron oxide, boron takes on an sp^2 hybridized electron configuration, leaving an empty p_z orbital, positioning the boron atom at the center of a planar triangle with oxygen at the vertices (see Schematic 1). The notation \emptyset is used to denote **bridging** oxygen (bO) and O to denote **non-bridging** oxygen atoms (nbO).

Boron in borate glasses has the lowest coordination number of any glass former in oxide glasses. The structure of borate glasses has been subject to much debate and continual development since Zachariasen and Warren introduced the concept of a continuous random network in the 1930s [1, 2]. By the 1960s, there were numerous spectroscopic experiments performed and several theories put forth regarding the structure of borate glasses. Krogh-Moe reviewed these results and ideas and concluded that a modified Zachariasen and Warren model was most suitable [3]. That is, the borate glass is comprised of a continuous random network of well-defined short-range order (SRO) borate units and intermediate range order (IRO) superstructures, expressing no long-range order or periodicity, as is characteristic of the glassy state. The modification of the borate structure is based on the short and intermediate range order units found in crystalline borate compounds. A comprehensive review on the comparison between crystalline and vitreous borates by Wright expounds on this relationship [4].



Schematic 1. Fundamental borate units - trigonal or three-fold coordinated boron (left) for boron with sp^2 electron configuration and tetrahedral or four-fold coordinated boron (right) for boron with sp^3 electron configuration for the highest degree of polymerization. Non-bridging oxygen ions can form on either units in crystals, though glasses favor nbO formation on the trigonal unit.

Structure and properties of pure boron oxide glass are discussed first in **Section 2**. The most fascinating aspect of borate glasses is the ability of boron to convert between trigonal and tetrahedral coordination in modified borate glasses, branded *The Boron Oxide Anomaly*, which is treated in **Section 3**. The impact of *The Boron Oxide Anomaly* on several properties and the rich IRO arising from superstructural units is also found in **Section 3**. The equilibrium governing the boron coordination change as a function of composition is discussed in **Section 4** and as a function of temperature in **Section 5**. The local environment of modifier cations in the glass structure is examined in **Section 6**. Mixed anion borate glasses are briefly reviewed in **Section 7**. Finally, a second boron anomaly has recently been discovered and is summarized in **Section 8**.

2. Boron Oxide Glass

Krogh-Moe's thorough analysis led to the conclusion that a significant fraction of the boron atoms are found in boroxol rings, consisting of three boron and three oxygen. The six-membered boroxol ring was originally observed as a highly symmetric sharp band in Raman spectra [5]. NMR studies conducted by Bray and co-workers gave strong support for the Krogh-Moe model, as well as suggested models in agreement with experimental data that predicted well the systematic evolution of the borate glass structure in binary alkali borate glasses [6-11]. A Raman investigation of O and B isotopically substituted B_2O_3 contributed strong evidence for the boroxol ring model [12]. Neutron diffraction and scattering experiments further provided support for the boroxol ring and the Krogh-Moe model [13, 14]. Today, it is well accepted that most of the boron atoms in vitreous B_2O_3 exist in planar six-membered rings- the boroxol ring. Further, the number of boroxol rings has been found to be approximately equivalent to the number of lone BO_3 entities –the number of boron in boroxol rings lies in the range of 60-85% [15]. Thus, about three times as many boron atoms exist in the ring structures as exist in isolated units, termed “loose” BO_3 triangles. In most cases, these “loose” BO_3 triangles – or better non-ring BO_3 units - are found as bridges between the superstructures, crosslinking the boroxol rings to one another.

2.1. General Properties of Pure Vitreous B_2O_3

Pure B_2O_3 forms a glass from the melt very easily. Attempts to cool molten B_2O_3 slowly as to induce crystallization have been unsuccessful, even with seed crystals planted in the melt [16]. In silica, the ease of glass formation might be attributable to the various crystalline polymorphs of SiO_2 such as tridymite, quartz, and cristobalite [17]. The analogous reasoning can actually be applied to borate glasses. Although there exist no known crystalline compounds that contain the boroxol ring - formed under the same ambient pressure conditions vitreous B_2O_3 is formed under - the boroxol ring is present in some binary borate compound such as cesium enneaborate, $Cs_2O \cdot 9 B_2O_3$ [18]. A computational investigation by Ferlat *et al.* calculated numerous crystalline polymorphs of pure B_2O_3 containing boroxol rings [19]. These “hidden polymorphs” could be the driving

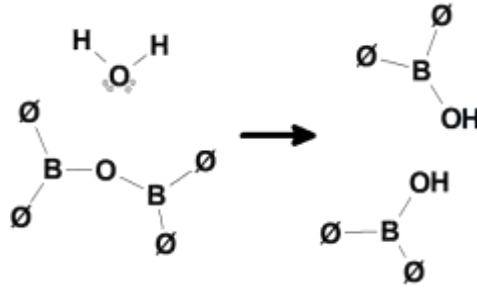
mechanism behind the ease of glass formation for pure B₂O₃ though they have not yet been realized in the laboratory.

Table 1. Some Properties of Boron Oxide Glass and Modified Borate Glasses.
References: A= Ehrt 2006 [20] , B= Shibata [21], C= Donohoe & Shelby 2005 [22], D= Jaccani 2016 [23], E= Yoshida 2009 [24], F= Ehrt 2013 [25]

Composition	T _g (°C)	Density (g cm ⁻¹)	Refractive Index <i>n_e</i>	Vickers Hardness (GPa)	Poisson Ratio
B₂O₃	230-240 (A)	1.81-1.84 (A,B)	1.4663 ^(A)	-	-
10 Na₂O – 90 B₂O₃	363 ^(C)	2.05 ^(C)	1.4955 ^(D)	2.99 ^(E)	0.279 ^(D)
15 Na₂O – 85 B₂O₃	408 ^(C)	2.12 ^(C)	1.5065 ^(D)	3.28 ^(E)	0.281 ^(D)
20 Na₂O – 80 B₂O₃	459 ^(C)	2.20 ^(C)	1.51 ^(D)	3.83 ^(E)	0.275 ^(D)
25 Na₂O – 75 B₂O₃	473 ^(C)	2.28 ^(C)	1.516 ^(D)	4.2 ^(E)	0.273 ^(D)
30 Na₂O – 70 B₂O₃	473 ^(C)	2.35 ^(C)	1.5225 ^(D)	4.44 ^(E)	0.27 ^(D)
35 Na₂O – 65 B₂O₃	463 ^(C)	2.46 ^(C)	1.526 ^(D)	4.2 ^(E)	0.273 ^(D)
17.5 Na₂O – 17.5 CaO- 65 B₂O₃	515 ^(C)	2.59 ^(C)	-	-	-
35 CaO – 65 B₂O₃	639 ^(C)	2.60 ^(C)	-	-	-
25 La₂O₃ – 75 B₂O₃	680 ^(A)	3.97 ^(A)	1.7525 ^(A)	-	-
48 Bi₂O₃ – 52 B₂O₃	400 ^(A)	6.37 ^(A)	2.024 ^(A)	-	-
56 ZnO – 44 B₂O₃	560 ^(F)	3.55 ^(F)	1.6954 ^(F)	-	-

Alone, vitreous boron oxide is very hygroscopic and readily attacked by water in the air. A vitreous sample of pure B₂O₃ will have a visibly affected surface within hours of formation if left exposed to the atmosphere. BO₃ units are strong Lewis acids while H₂O acts as a Lewis base. The H₂O causes the dissociation of the B-O-B bond to form hydroxyl groups bonded to the boron atom, B-OH (see Schematic 2). The fully hydrated BO₃ molecule is known as boric acid, B(OH)₃ (again by acting as Lewis acid rather than a classical Brønsted acid: B(OH)₃ + H₂O → B(OH)₄ + H⁺, pK_s=9.14 [26]) This hygroscopic

nature of boron oxide prohibits any practical applications of pure borate glasses and requires the careful engineering of borate glass compositions; however, the relatively quick and complete dissolution of a borate network in the presence of water allows the use of multicomponent borate glasses for wound healing applications [27]. Moreover, the entirety of the borate network may dissolve in the body leaving no trace of boron, contrary to silicate materials leaving behind silica rich regions in the body after dissolution [28].



Schematic 2. H_2O reacting with a borate network segment to form hydroxyl groups bonded to boron atoms.

2.2. Vibrational Spectroscopy

Raman spectroscopy provided the strongest early evidence for the existence of the boroxol ring [5]. The planar boroxol rings are readily identifiable in Raman spectroscopy by a strong, highly symmetric band at 805 cm^{-1} . The band arises from the symmetric stretch of the bridging oxygen atoms of the ring breathing mode and has been shown to be independent of the boron atoms by investigation using isotopic $^{10}\text{B} \leftrightarrow ^{11}\text{B}$ substitution [29]. Because of its sharpness and strong intensity, this characteristic band is visible in the Raman spectra of many modified borate glasses. Aside from the ring breathing of the boroxol ring, other features observable in the Raman spectra of vitreous B_2O_3 are the symmetric stretch of the oxygen bridging two boroxol rings ($\sim 460\text{ cm}^{-1}$) and less so the bending modes of the loose BO_3 triangles between $620\text{--}760\text{ cm}^{-1}$ as well as B-O stretching modes above 1200 cm^{-1} (see Figure 1 black).

The absorption coefficient spectra of the same $\nu\text{-B}_2\text{O}_3$ glass is shown in the same figure above the Raman spectra. Infrared spectroscopy is well suited for borate materials as the light mass and low coordination of the boron atoms result in high frequencies of the normal vibrations. Thus, as other elements added to a borate network often show

vibrational modes below 1200 cm^{-1} , overlapping with bands of the trigonal borate network bands is no issue. However, bands of other network formers such as silica will overlap with the bands of boron tetrahedra. The glassy boron oxide IR spectrum displays the three infrared active fundamental vibrational modes of the trigonal borate unit from Schematic 1 and without added modifier oxides, no sign of B_4 units. The main feature in the bending region at 725 cm^{-1} arises from the out-of-plane bending, ν_2 , mode while the feature at $\sim 660\text{ cm}^{-1}$ is due to the in-plane bending, ν_4 , mode. The high frequency envelope results from the asymmetric stretch of the boron-oxygen bonds of B_3 structures.

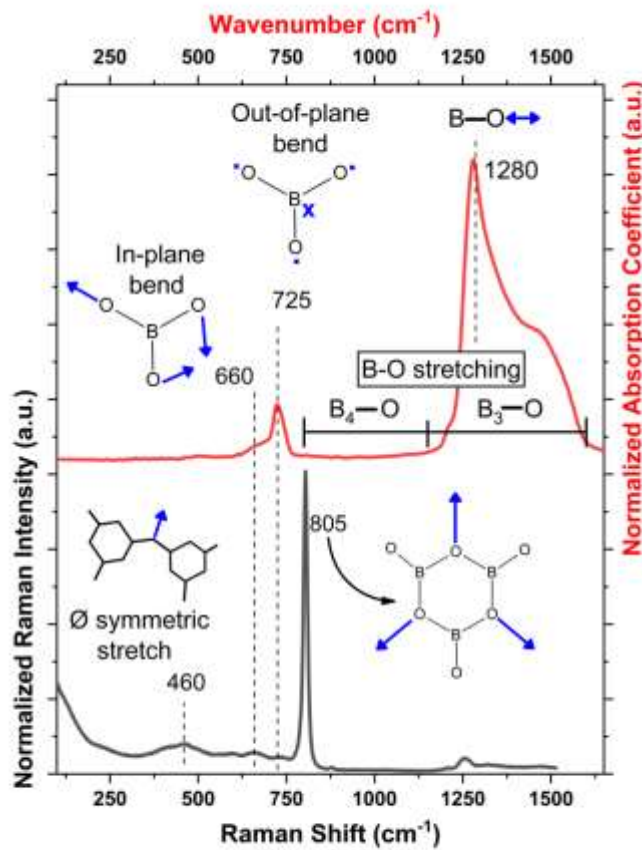


Figure 1. Absorption coefficient spectrum (top) and Raman spectrum (bottom) for pure boron oxide glass obtained from melting B_2O_3 at $1200\text{ }^\circ\text{C}$ for 15 minutes in a platinum crucible.

Binary Borate Glasses

Borate glasses can exhibit a wide range of properties, which depend strongly on the type and quantity of modifier oxides or other additives. Borates have a good solubility and wide glass forming region with many oxides. The transparency in the UV region is good when mixed with cations of low polarizability. High loads of highly polarizable modifiers are known to give glasses with low melting point and a low glass transition temperature (see Table 1) [30]. Borate glasses can be readily formed by casting into molds or fiber drawing [31].

Structural studies often use vibrational or NMR spectroscopy. The infrared spectra for borate glasses can usually be split into three main regions: trigonal unit bending vibrations between 600-800 cm^{-1} , boron-oxygen bending and stretching in tetrahedral boron (B_4) between 800-1150 cm^{-1} , and boron-oxygen stretching in trigonal boron (B_3) between 1150-1600 cm^{-1} (discussed later in detail in Section 3 on modified borate glasses). The fraction of four coordinated boron can be quantified from either infrared or NMR spectroscopy [32].

2.3. NMR Spectroscopy

NMR spectroscopy has been utilized most extensively to provide quantitative information regarding the bulk structure of borate glasses and boron speciation using ^{10}B and ^{11}B NMR [6-11, 33-40]. Early on, ^{17}O NMR on pure boron oxide glass identified two distinct oxygen sites arising from different B-O-B bond angles from oxygen atoms in rings and non-ring borate units [10]. In modified borate glasses, NMR has been widely used to quantify the fraction of four-coordinated boron. While trigonal BO_3 units may have zero, one, two, or three bridging oxygen atoms, their signals contribute to a single convoluted band (see Figure 2). Trigonal units with all bridging oxygens or all non-bridging oxygens are termed symmetric B_3 units, while trigonal units with one or two non-bridging oxygens are termed asymmetric B_3 units. Symmetric and asymmetric B_3 units give rise to different signals. Thus, NMR spectroscopy permits the quantification of symmetric B_3 , asymmetric B_3 , and B_4 as well as ring and non-ring boron. Small isotopic shifts can provide additional information on the next neighbors, as can more complex correlation experiments.

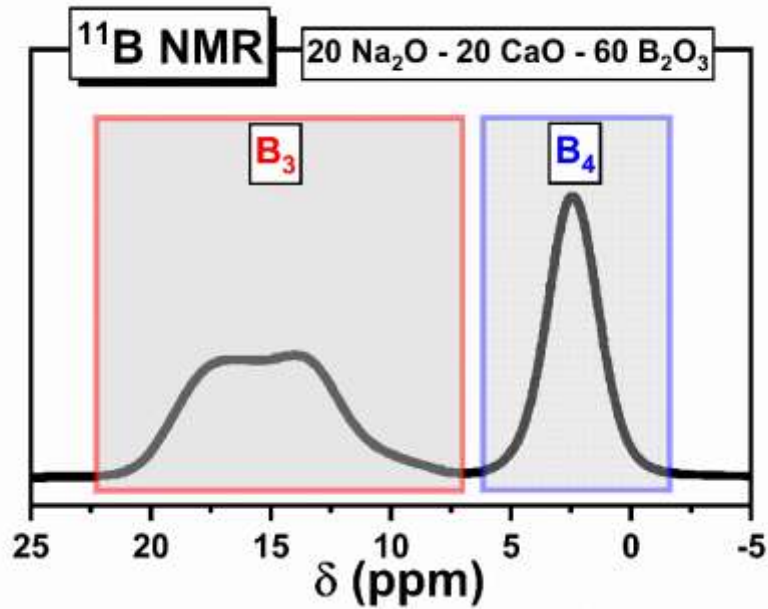


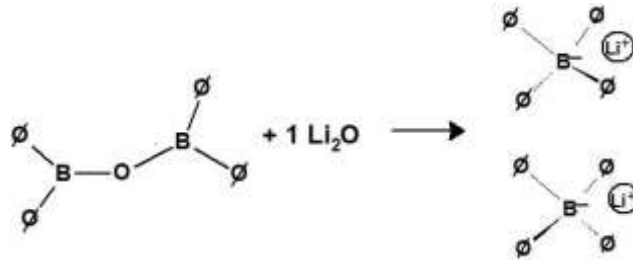
Figure 2. ^{11}B NMR spectrum of modified borate glass [41] displaying the convoluted trigonal boron band and its separation from the tetrahedral boron band.

3. Modified Borate Glasses

3.1. The Boron Oxide Anomaly

Though the hygroscopicity of B_2O_3 impedes any significant applications of pure vitreous boron oxide, contrary for example to SiO_2 glasses, combining B_2O_3 with other components, from network former to network modifier oxides, can result in very stable glasses with a wide range of structures and properties. Many binary borate glasses of B_2O_3 with other oxides, exhibit large and continuous binary glass forming regions (Li_2O , PbO) while others are narrow or discrete (MgO , La_2O_3 , ZnO), due to crystallization or liquid-liquid phase separation. The response of the borate network in the presence of modifying cations is truly what makes borate glasses unique and sets them apart from the most common classical glass formers P_2O_5 or SiO_2 (though GeO_2 and TeO_2 glasses also show interesting changes of glass former coordination). In contrast to the depolymerization of the network observed in silicate or phosphate glasses, the addition of an alkali metal oxide, M_2O , to pure B_2O_3 increases initially the network connectivity [42]. The trigonal boron sites (sp^2 hybridized) with three bridging oxygen (bO) convert to tetrahedral boron sites

(sp^3 hybridized) with four bO and a negative charge delocalized across the tetrahedra (see Schematic 3).



Schematic 3. Conversion of two trigonal borate units into two tetrahedral borate units after the addition of one unit of alkali oxide.

For the binary system $x M_2O - (1-x) B_2O_3$ where M is an alkali element (Li, Na, K, etc.), increasing x yields the formation of $[B\emptyset_4]^-$ (recall \emptyset denotes bridging oxygen) that exist in well-defined superstructure units (see Figure 3). Penta-borate and tri-borate units appear first at the expense of boroxol rings. Penta-borate and tri-borate units may connect to form tetraborate groups. Increasing modifier content results in additional tetrahedral units in these superstructures giving di- & tri- pentaborates and di-triborates, all increasing the dimensionality of the borate network. As boroxol rings disappear, diborate groups and non-ring borate tetrahedra form as the fraction of tetrahedrally coordinated boron with all bO approaches a maximum. Figure 3 displays SRO and IRO ($5 \text{ \AA} - 20 \text{ \AA}$) borate structures with all bridging oxygen atoms. Because of the equilibrium between tetrahedral $B\emptyset_4^-$ and trigonal $B\emptyset_2O^-$ metaborate, which depends on the amount and type of added modifier oxide, a non-bridging oxygen atom may form on a trigonal unit of the superstructure [4].

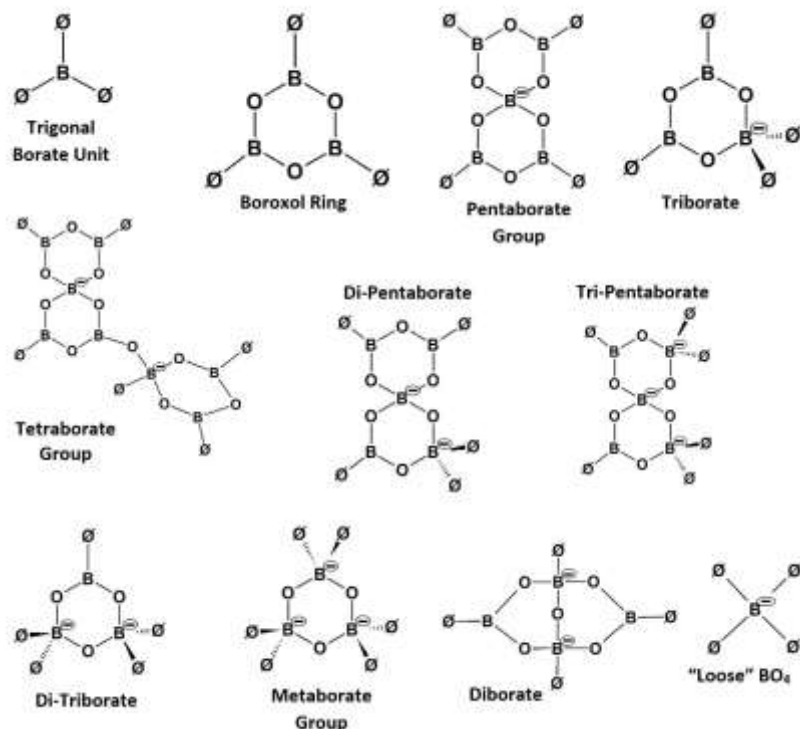


Figure 3. Short range and intermediate range order borate units with all bridging oxygens.

The co-presence of the four coordinated boron and formation of superstructural units with fixed internal degrees of freedom is responsible for the non-monotonic evolution of many physical properties. This includes for example a maximum in the glass transition temperature, a minimum in the coefficient of expansion, and a local maximum in the isothermal viscosity (see Figure 4). Other properties such as density [21, 43], hardness [24], and dissolution rate [44] display similar non-linear behavior.

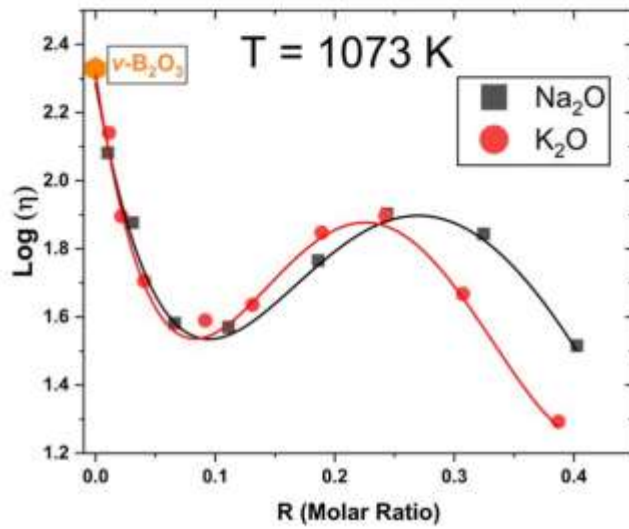
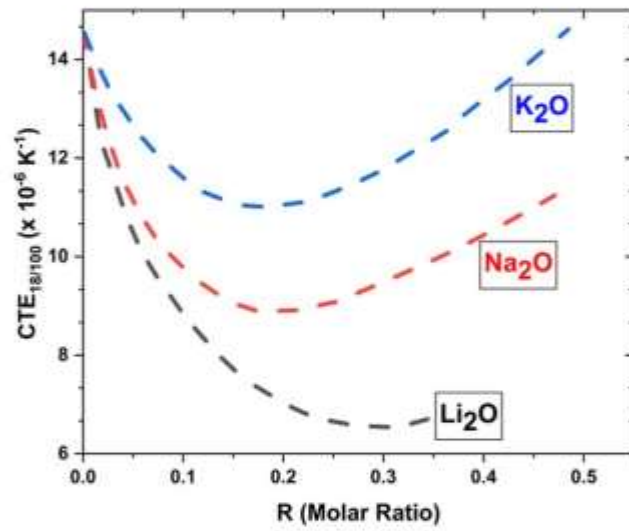
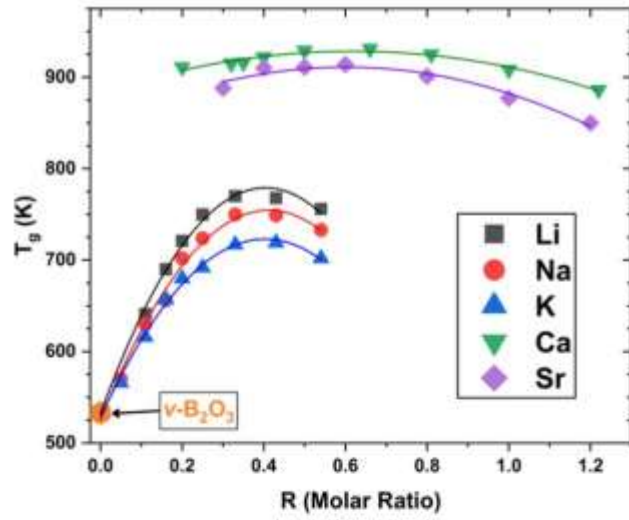


Figure 4. Anomalous trends in physical properties of borate glasses as a function of modifier content expressed as molar ratio, R, the ratio of M₂O (or MO) content to B₂O₃ content- (top) glass transition temperature over the range of the anomalous behavior [45, 46], (middle) coefficient of thermal expansion [47], and (bottom) isothermal viscosity at 1073 K [48]. In the top and bottom figure, the fitted lines are guides for the eyes only.

The fraction of four-coordinated boron, $N_4 = B_4 / (B_3+B_4)$, that forms with the addition of modifier oxide in the system $x \text{M}_2\text{O} - (1-x) \text{B}_2\text{O}_3$ can be predicted for low M₂O content by

$$N_4 = \frac{x}{1-x} \quad (1)$$

The expression accurately predicts N_4 for up to ~30 mol% alkali content, then diverges rapidly from the real structure (see Figure 5).

Several models have been proposed and have been refined over the years, to predict the occurrence of structural units as a function of composition with Bray & co-workers leading the way [4, 6-9, 11, 49]. More recently, topological constraint theory (TCT) shows promise as a model to predict the evolution of borate structure and properties such as glass transition temperature [50] though the validity of this approach has received criticism [51]. Recently, TCT was applied to lithium borate glasses where the occurrence of alkali clusters were considered [52]. The predicted structure agreed very well with the experimental NMR model of Feller and Bray [8]. Shortly after, the glass transition temperatures were calculated with the model and the predicted values trend very well with experimental T_g data up to relatively high lithia contents [53].

While interest in TCT models stems from their potential to be able to predict properties and thus offer a more economical alternative to the experimental approach, thermodynamic modelling has been more successful in the prediction of structural units – both SRO and IRO- for the case of the sodium borate binary and the sodium borosilicate ternary over the entire glass forming range. Vedishcheva’s model is built upon the concept of chemical structures derived from the composition of the melt into stoichiometric groupings that correspond to the respective crystals [51].

It should be noted that NMR spectroscopy is a bulk technique for selective structural studies. And while technical advancements have increased the sensitivity of the instruments significantly over the past decades, NMR spectroscopy is not very sensitive to very small populations of certain units. Probe ions such as Ni^{2+} and Co^{2+} change their coordination from octahedral in glasses without non-bridging oxygen ligands to tetrahedral for glasses that do offer non-bridging oxygen ions for complexation. Doped borate glasses show the presence of tetrahedral Co^{2+} ions for R values exceeding $R=0.2$ [54], and not only for $R=0.5$, where NMR spectroscopy sees the onset of nbO formation.

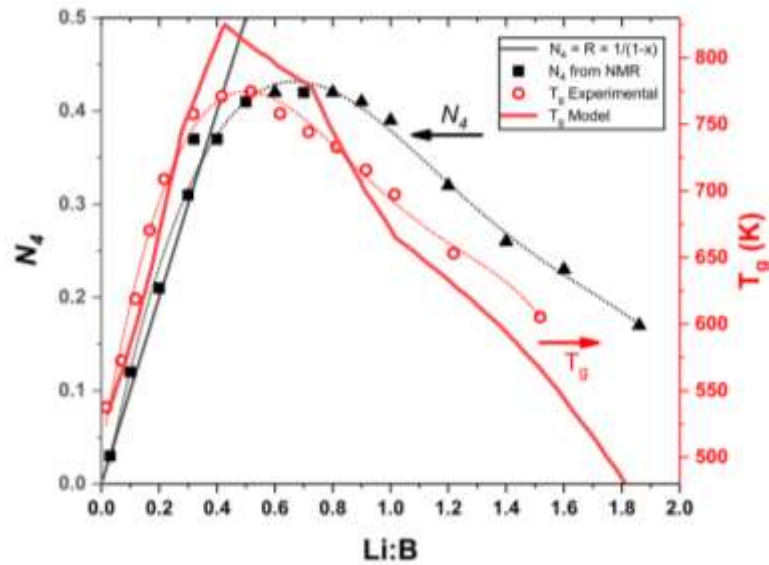


Figure 5. Four-coordinated boron N_4 and glass transition temperature T_g for binary lithium borate glasses. N_4 fraction (left axis) determined by NMR (data from Kroeker [38] (squares) and Yun [11] (triangles)), Equation 1 (solid black line), T_g Experimental from Feller and Affatigato [55] (open circles), and T_g Model from Takeda [53] (solid red line)

Figure 5 plots experimental NMR data for N_4 [11, 38] alongside Equation 1 which is indeed seen to follow the straight line and then diverge at the diborate composition. The trend for the glass transition temperature as a function of alkali content follows closely the trend for four-coordinated boron where T_g increases up to the diborate composition and then decreases as the population of non-bridging oxygens becomes significant. The predicted T_g from a recent topological constraint theory model [53], shown as the solid red line, agrees well with the experimental T_g [55].

The fraction of four-coordinated boron is directly related to the degree of connectivity of the network. As mentioned earlier in this section, many properties go through an extremum that is intimately related to N_4 and thus the connectivity of the network. The Vickers hardness of binary sodium borate glasses increases with Na_2O content and reaches a maximum around 30 mol% Na_2O [24]. The dissolution rate of binary lithium borate glasses was observed to go through a minimum around 25-30 mol% alkali content [44]. More recently, the dissolution rate of ternary alkali-alkaline earth-borate glasses was also found to be tied to the fraction of four-coordinated boron, as expected with slower dissolution rates associated with higher N_4 [41].

3.2. Depolymerization of the Borate Network

For binary lithium or sodium borates, only after the complete destruction of the boroxol groups (~25 mol% M_2O) do a small fraction of trigonal boron with non-bridging oxygen appear and the depolymerization of the borate network with increased modifier content begins. Trigonal metaborates may exist in ring arrangements, $\text{B}_3\text{O}_6^{3-}$, or as chains, $[\text{BO}_2]_n^{n-}$. Further modification yields pyroborate dimers, $[\text{B}_2\text{O}_5]^{4-}$, and eventually orthoborate monomers, $[\text{BO}_3]^{3-}$ [56]. Figure 8 displays short range and intermediate range borate structures containing one or more non-bridging oxygen atoms.

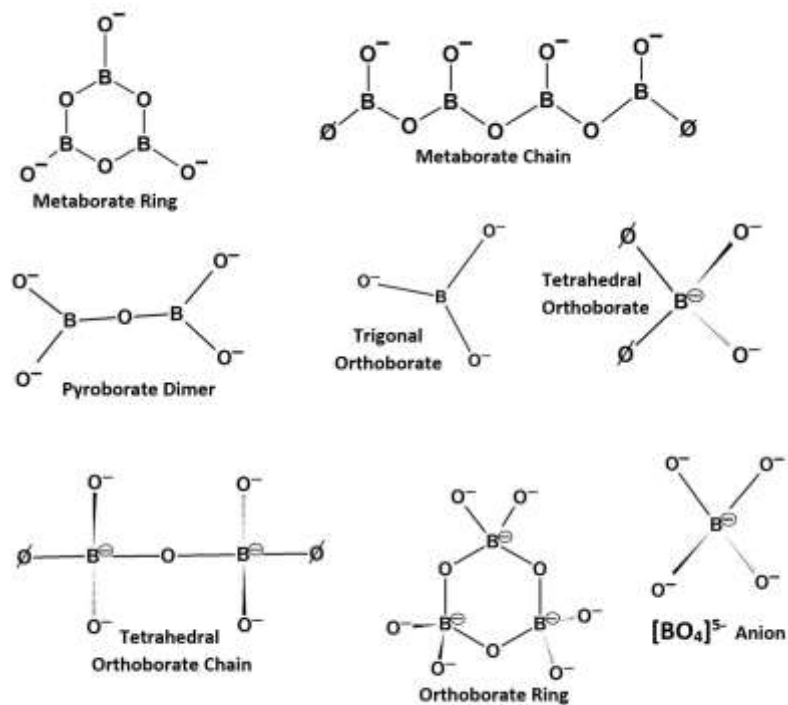
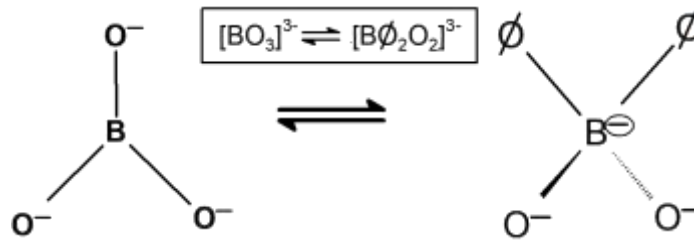


Figure 6. SRO and IRO borate units containing non-bridging oxygens.

Kamitsos *et al.* have demonstrated that the borate network modification by alkali ions depends on both the amount of alkali content as well as the type of alkali [57, 58]. Through systematic Raman investigations of alkali borates, it was suggested that while highly modified lithium and sodium borate glasses favor the formation of trigonal orthoborate units, the glass of the same stoichiometry containing either rubidium or caesium consist of the tetrahedral orthoborate species, possibly in chains or cyclic $B_3O_9^{9-}$ anions [59]. The potassium analogue presented evidence of both trigonal and tetrahedral orthoborate units. The orthoborate species are isomeric according to the equilibrium reaction:



Schematic 4. Isomerization between a single trigonal unit and single tetrahedral unit at the orthoborate stoichiometry.

4. Binary Glass Forming Borates

4.1. Monovalent Modifier, M_2O

The modification of the borate network is highly dependent on the type and amount of constituents added. As is the case for glasses, the driving mechanism for vitrification is the prevention of crystallization, often supported by a higher degree of disorder and confusion, which is in turn supported by isomerization and disproportionation equilibria. Studies of alkali, alkaline- earth, transition metal, and post-transition metal ions in borate glasses suggest correlations between the size and charge of the ion and the



equilibrium [32, 56-68]. For the binary alkali borate series $M_2O - 2 B_2O_3$, the fraction of four-fold coordinated boron, N_4 , was seen to decrease as the field strength¹ of the modifier decreased. The glasses of the same stoichiometry favoring the right side of Equation 2 will have a higher degree of connectivity, determined by the number of bridging oxygens per boron, than those that favor the left side of Equation 2. The glass transition temperature displays this with T_g decreasing linearly with decreasing network connectivity from $Li > Na > K > Rb > Cs$ for the same $M_2O - 2 B_2O_3$ glasses [58]. Mixed alkali glasses with fixed modifier content, $(x) M_2O - (1 - x) M'_2O - B_2O_3$ favor the left hand side of Equation 2 relative to single alkali glasses for $R < 1$ and have a non-linear T_g variation between $x=0$ and $x=1$ [56].

¹ The field strength (F_s) of a cation is $F_s = Z_C / a^2$ where Z_C is the valence of the cation and a is the distance between the cation and oxygen

The dependence of Equation 2 on the type of alkali has been explained in terms of charge density and Lewis acid-base behavior [69]. As the alkali size increases the alkali-oxygen bond distance increases resulting in lower charge densities for larger M^+ . Though the $[B\emptyset_4]^-$ unit has a delocalized negative charge, the charge is confined to the tetrahedron. Meanwhile, the negative charge associated with the $[B\emptyset_2O]^-$ unit is not restricted to the trigonal polyhedron and can be delocalized beyond the first coordination sphere. Thus entails that the smaller M^+ , with their higher charge density, will prefer the boron tetrahedra with its confined delocalized charge, while the larger M^+ with lower charge density will prefer the trigonal borate unit with the more diffuse negative charge. In terms of the Lewis acid-base behavior, the $[B\emptyset_2O]^-$ unit is a soft Lewis base while the $[B\emptyset_4]^-$ unit is hard Lewis base. The Lewis acidity decreases with increasing alkali size. The hard Lewis acid Li^+ preferring the hard Lewis base $[B\emptyset_4]^-$ and as the Lewis acidity of the alkali decreases from $Na > K > Rb > Cs$ the soft Lewis base $[B\emptyset_2O]^-$ becomes favored.

4.2. Divalent Modifier, MO

When comparing alkaline earth borate glasses, a contrary trend in borate speciation near the metaborate stoichiometry $0.45 MO - 0.55 B_2O_3$ is reported for the variation of the alkaline-earths than earlier discussed for the alkali borates of similar stoichiometry (the pure alkaline-earth metaborate 50:50 composition tends to crystallize and does not form glasses, except for $M=Mg, Ca$ [63]). The borate network favors the right side of Equation 2 with decreasing modifier field strength. Moreover, for $x MO - (1 - x) B_2O_3$ glasses, the value of x that gives the highest N_4 decreases from $Mg > Ca > Sr > Ba$ as the field strength decreases [32].

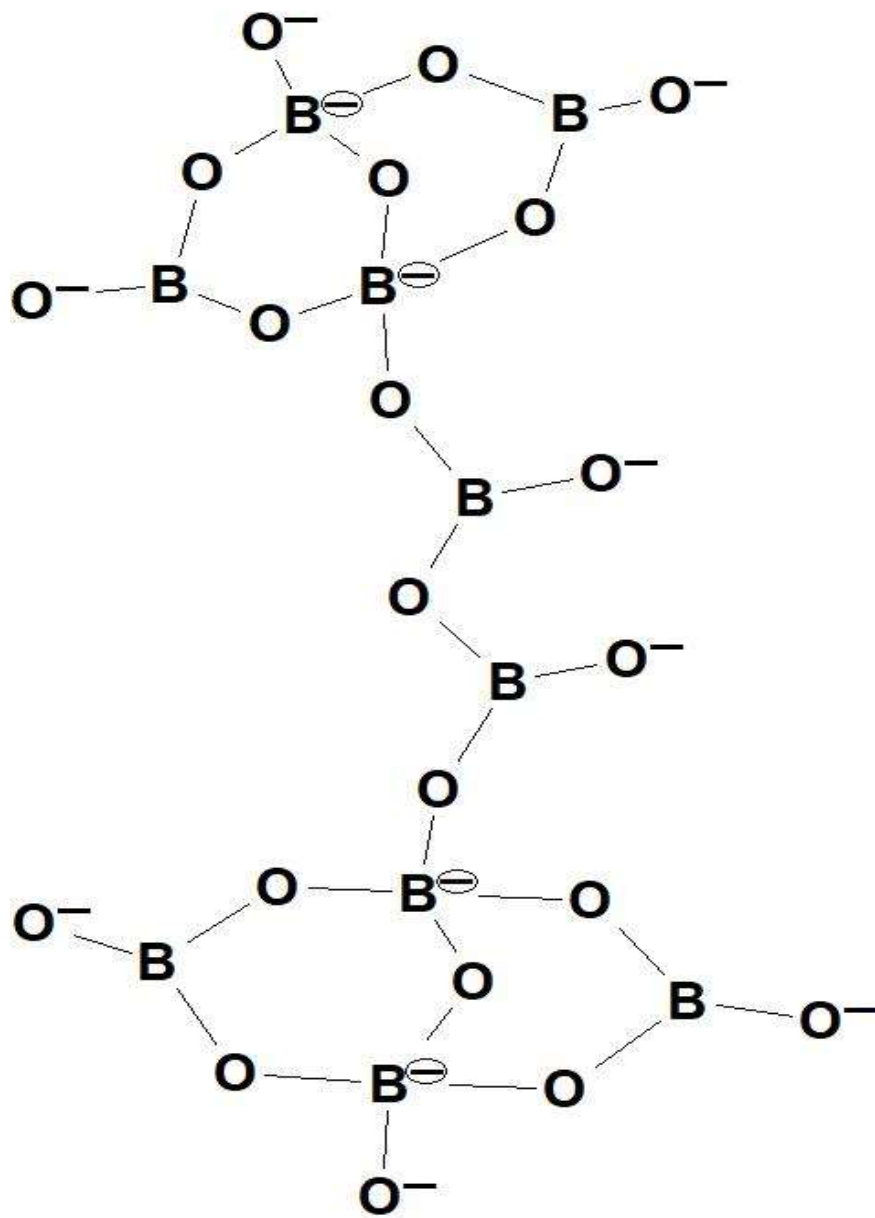
The correlation between the glass transition temperature and the fraction of four-coordinated boron observed for modification via alkali ions does not translate directly to alkaline earth modified borates. The T_g of alkaline earth borates, which is on the order of 150-200 °C higher than that of alkali borates, results from the cations strong cross-linking ability of these M^{2+} cations with their higher field strength.

Actually, the T_g increases steadily with increasing field strength of the M^{2+} cations despite the fact, that Mg^{2+} favors trigonal over tetrahedral borate units (see Section 5) [56]. When looking only at the degree of polymerization within the glasses near the metaborate

composition, T_g does increase with increasing N_4 fraction from Ba < Sr < Ca ($N_4 \sim 0.4$). However, as mentioned before, Mg-metaborate has the highest T_g of the alkaline earth metaborates and the lowest fraction of tetrahedral boron, $N_4 \sim 0.2$ [32, 45]. The field strength of Mg is the highest of the alkaline earths, thus the correlation between increasing T_g with increasing N_4 is not universally applicable and the crosslinking strength of the cation can have a significant impact.

ZnO – B₂O₃ near the metaborate ratio, like MgO – B₂O₃ [55, 63], displays an interesting case of a high degree of disproportionation. Completely unmodified BØ₃ and boroxol rings are observed to coexist alongside the high charge density pyroborate BØO₂²⁻ and orthoborate BO₃³⁻ species [60]. For SrO – B₂O₃ near the metaborate composition, such highly charged units are not observed and the glass structure primarily consists of trigonal metaborate chains as well as the tetrahedral boron containing di-triborate and diborate superstructures.

The PbO – B₂O₃ system lies outside the norm in that there is a high fraction of tetrahedral boron while the glass displays a low glass transition temperature. High density glasses such as lead and bismuth borate find application by way of their radiation shielding capabilities [70, 71]. Lead and bismuth borates form glasses over a wide composition range with evidence of PbO_n and BiO_n pseudo-phases forming, consisting of Pb-oxygen and Bi-oxygen polyhedra with a considerable degree of covalency that remove oxygen available to the boron atoms, resulting in the apparent under modification of the borate network [72]. Lead metaborate glass has been suggested to contain the large bi-diborate poly-anion, [B₁₀O₂₁]¹²⁻ that was originally found in crystalline 6 PbO – 5 B₂O₃ (Schematic 5), one of the few known examples of tetrahedral with on nbO [60, 73, 74].



Schematic 5. Bi-diborate poly-anion found in crystalline $6 \text{ PbO} - 5 \text{ B}_2\text{O}_3$ [71].

4.3. Trivalent Modifier, M_2O_3 ($M = Al, Bi, RE$)

The interaction of rare earth elements in borate glasses is of particular importance for optimizing the process of nuclear waste immobilization in borosilicate glasses. Several studies have looked at the binary $x La_2O_3 - (1 - x) B_2O_3$ system where glass formation is only possible in a small window around the metaborate composition [20, 75-77]. Liquid-liquid phase separation occurs in the crucible for $x < \sim 0.22 La_2O_3$ down to less than 1 mol% La_2O_3 [75]. The glasses formed with trivial amounts La_2O_3 are essentially pure boron oxide glass doped with La^{3+} ions and are comprised of boroxol rings and non-ring $- BO_3$ triangles, as there does not exist enough modifier to impact the structure. The vibrational spectra of the lanthanum metaborate glass, 25 $La_2O_3 - 75 B_2O_3$, was seen to be very similar to the corresponding crystal which is known to be comprised of borate tetrahedra linked via trigonal borate units to form infinite chains that are crosslinked by the 10-coordinated La^{3+} ions [75]. Clear, homogenous glasses with high refractive index ($n = 1.70-1.77$) form in the binary between 25-28 mol% RE_2O_3 ($RE = La, Sm, Nd$) though clear glasses containing 22-28 mol% La_2O_3 have been reported [75, 78, 79]. Binary borate glasses containing 20, 25, and 30 mol% R_2O_3 for La, Nd, Pr, and Sm were studied with Raman spectroscopy suggesting glasses of the same composition were structurally similar for different RE^{3+} , although no comment was made on the homogeneity of the melts and glasses [77].

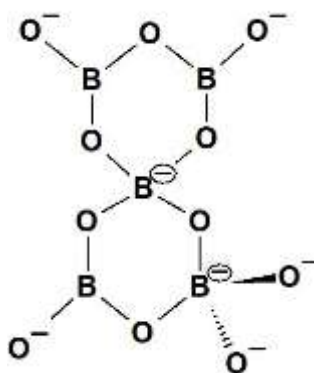
Interesting is the case of europium borates, where binary Eu-borates and ternary Eu-aluminoborates may form with up to 33 mol% and 43 mol% EuO, respectively [80]. This increased range of glass formation is attributed to a significant fraction of divalent Eu^{2+} present, acting similar to Ca^{2+} [80].

The cessation of glass formation for RE^{3+} elements smaller than Sm^{3+} is due to the instability that arises from the increased O-O repulsion between the ladder-like borate chains [76]. However, substitution of smaller ions such as Gd^{3+} or Y^{3+} for up to $\sim 5\%$ La^{3+} is possible before phase separation is observed. The interchain spacing can be increased by substituting Al_2O_3 or Ga_2O_3 for up to 25 mol% B_2O_3 where the Al or Ga take on a glass forming nature as they occupy the sites of the borate tetrahedra in the structure. The increased chain spacing with this substitution decreases interchain repulsion thereby

allowing glass formation with elements smaller than samarium. Indeed, yttrium aluminoborates may be prepared with 10-25 mol% Y_2O_3 as studied with vibrational spectroscopy by Chakraborty [81] and, more recently, comprehensively with NMR and EPR by Deters [35, 36].

The effects of melting in an alumina crucible on structure and properties of phosphates and tellurites has been investigated recently revealing the profound impact that dissolution of alumina crucible material into the melt can have on the resulting glass [82-84]. Alumina readily mixes with the borate melt, whether added intentionally or by melting in an alumina crucible [85]. In aluminoborates, alumina will compete with the boron for oxygen, decreasing N_4 [37].

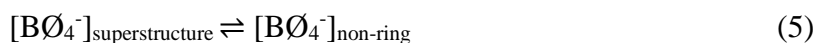
Bismuth borates have applications as high-density radiation shielding materials like their neighbor lead borates, without the environmental toxicity. Bismuth borates are structurally quite interesting as neutron diffraction and infrared spectroscopy have revealed a significant fraction of B_4 across a broad glass forming range (31-67 mol% Bi_2O_3), though the known form of crystalline $2 Bi_2O_3 - B_2O_3$ contains only trigonal B_3 species [86]. Like lead-borates, bismuth-borates possess a low glass transition temperature despite their high fraction of tetrahedral boron (see Table 1). Similarly to their heavy metal oxide neighbor, bismuth metaborate glasses are thought to contain the $[B_5O_{11}]^{7-}$ poly-anion which is essentially a di-pentaborate group where the non-central B_4 unit has 2 bO and 2 nbO (Schematic 6) [60, 87].



Schematic 6. $[B_5O_{11}]^{7-}$ poly-anion present in bismuth borate crystals and possibly glasses [85].

5. Temperature Dependence of the Borate Melt Structure

The final structure of the borate network can also be influenced by the preparation route. High temperature experiments show that for pure B₂O₃, at high temperatures the boroxol rings breakdown into non-ring trigonal borate units [88-93]. Yano *et al.* carried out in-situ Raman scattering experiments on vitreous boron oxide and binary sodium borates over the range from room temperature up to 1200 °C. For pure boron oxide glass, their results agreed with earlier high temperature experiments by Walrafen [88] and Hassan [89]. Yano *et al.* analyzed the Raman spectra of borate glasses at different temperatures by comparing the high frequency region, between 1100 cm⁻¹ and 1600 cm⁻¹, related to the B-O stretch of trigonal units in both ring and non-ring (“loose”) configurations, to the signal in the middle frequency range of the spectrum, between 700 cm⁻¹ and 850 cm⁻¹, where superstructure units appear. The broad high frequency band was deconvoluted into modes associated with the BØ₃ in boroxol rings, “loose” BØ₃, and BØ₂O⁻ by comparing the pure boron oxide glass, the binary sodium borate glasses, and previous Raman work correlating the B-O bond length and Raman frequency of metaborate crystals [94]. Based on the physical phenomena whereby the Raman scattering intensity is proportional to the concentration of the scattering species, Yano *et al.* showed quantitatively the effect of temperature on the short-range order and intermediate range order by comparing relative intensities with increasing temperature and sodium content. The results can be considered in the following set of equilibrium reactions:



Pure boron oxide glass, in agreement with the aforementioned previous work, favored the right-hand side of Equation 3 with increasing temperature. Equation 4 showed weak temperature dependence for sodium borate compositions with low alkali, ≤ 20 mol%, where nbO are not observed in the glasses at room temperature by NMR spectroscopy and the structures consist primarily of boroxol, tetraborate, and pentaborate groups. For ≥ 20

mol% alkali, Equation 4 becomes strongly temperature dependent, favoring the right-hand side with increasing temperature (See Figure 7).

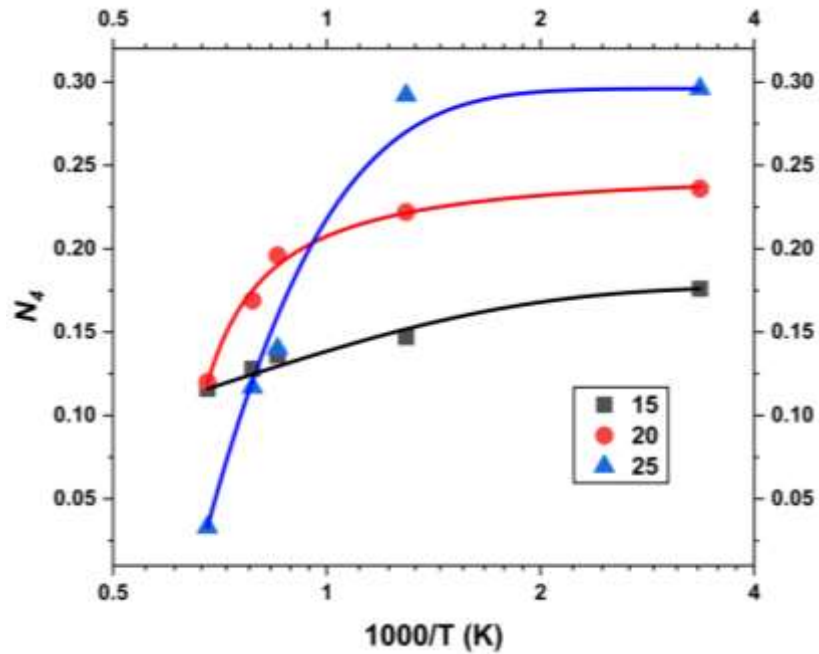


Figure 7. Temperature dependence on the fraction of four-coordinated boron, determined by Raman spectroscopy, in $(x) \text{Na}_2\text{O} - (1-x) \text{B}_2\text{O}_3$ glasses for $x=15$ mol% (squares, $R=0.18$), $x=20$ mol% (circles, $R=0.25$), and $x=25$ mol% (triangles, $R=0.33$). For more detailed information, see the cited texts [91-93].

The temperature at which the short range order structures rearrange in Equation 4 was observed to have a highly nonlinear alkali content dependence, ranging between $T_g + 50$ °C to $T_g + 400$ °C. Contrastingly, the rearrangement of superstructures was seen to take place at approximately the glass transition temperature regardless of the alkali content, with Equation 5 being prevalent between the glass transition temperature and the composition dependent temperature that the short range order reconfiguration occurs. In this range, the intermediate range order structures undergo reconfiguration or decomposition but the fractions of BO_4 and BO_3 units remain unchanged. More recently, Alderman's high temperature X-Ray diffraction experiments support the Raman data for alkali borate systems with the right side of Equation 4 being favored at high temperature [95].

Highly modified alkali borates showed a similar temperature dependence. Kamitsos and Karakassides studied the effect of melt temperature on the resulting structure of $0.70 \text{ Na}_2\text{O} - 0.30 \text{ B}_2\text{O}_3$ by melting at 800°C , 1100°C , and 1400°C and quenching glasses from these temperatures [96]. They reported an increased relative population of trigonal orthoborate units for glasses quenched from melts of 1400°C indicating the decomposition of pyroborate dimers and rings containing BO_4 tetrahedra, analogous to the breakdown of the boroxol ring for pure boron oxide.

6. The Metal Cation Environment

As previously mentioned, infrared spectroscopy provides an excellent probe of the borate network due to the relatively high fundamental frequencies of borate units associated with their low mass. In most spectra of alkali containing binary glass systems, a broad band in the far infrared region arises from overlapping network deformation modes and from the cation vibrations. However, in borate glasses both band systems are distinct and allow for in depth study of the cation environment [97]. The frequency of the cation band correlates directly with the inverse square root of the mass of the cation [32]. The force constant quantifying the strength of the cation-oxygen ionic interactions can be derived directly from the cation-motion frequency in the far-infrared, and gives a better parameter than the field strength when comparing the effect of modifier cations in glasses. In addition, it allows the comparison of transition metal cations with alkaline earth cations, that is cations for which the mass and radius are not changing systematically, and not only between elements of the same period of the periodic table of the elements [60, 72, 74].

The glass transition temperature has been shown to be linearly dependent on the effective cation-oxygen force constant for alkali borate glasses containing up to 30 mol% alkali oxide [46]. The higher the force constant, the stronger the interaction between the alkali metal cation and the glass network. For a fixed composition (i.e., alkali oxide content), the calculated force constant and experimentally measured glass transition temperature were seen to decrease linearly with increasing size of the alkali. Figure 9 plots the force constant versus the glass transition temperatures for tetraborate alkali glasses (20 mol% M_2O) and various metaborate glasses. The glass transition temperature is seen to correlate directly with the effective force constant for all compositions.

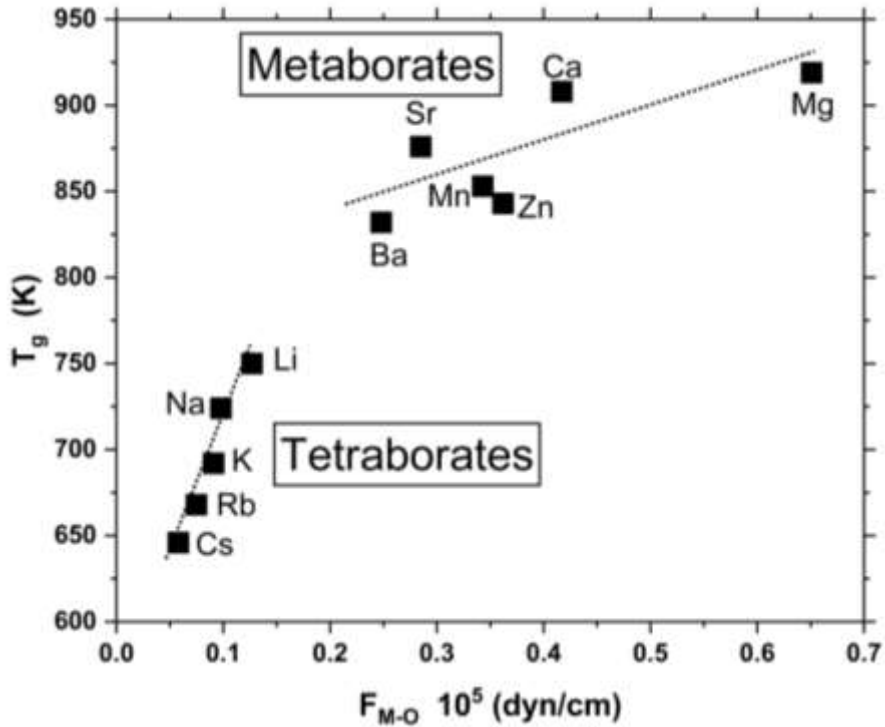


Figure 8. Force constant versus glass transition temperature for varying modifier types in borate glasses. Some 50 MO – 50 B₂O₃ (metaborates) [72] and 20 M₂O – 80 B₂O₃ (tetraborates) [46].

As in silicates, Li₂O and MgO tetrahedra can occur in borate glasses as conditional network formers. For lithium borate glasses modified beyond the metaborate composition, formation of [LiO₄]³⁻ tetrahedra have been observed displaying a high degree of covalency with the borate network, implying the role of Li₂O in the binary alkali system changes from a network modifier to a conditional network former as non-bridging oxygens, not (BØ₄)⁻, become the majority of the network's charged sites [56]. Similarly, magnesium acts as a modifier in Na-Mg-borates containing ≤ 15% MgO but enters the network as [MgO₄]²⁻ tetrahedra at ≥ 20 mol% MgO [34].

Deconvolution of the cation motion band for borate glasses of varying alkali content led to the proposition of the two-site model by Kamitsos *et al.* [62]. In contrast to the random site model, they propose that the alkali cation population is distributed between, at least, two distinct sites, one of high frequency and one of low frequency, where the frequency is related to the depth of the potential well for a given site. Molecular dynamics

simulations of lithium borate glass showed the two sites arise from different charge environments leading to formation of isolated (low frequency) and neighboring or aggregated (high frequency) Li ion sites [63, 98, 99].

The low frequency sites hold metal cations in higher coordination, situated between BO_4^- and BO_3 units. Conversely, the high frequency sites contain metal cations bonded to fewer oxygen atoms, that belong to BO_3 , BO_4^- and BO_2O^- units, where the M-O average separation distance in isolated sites was found to be smaller than the M-O distance in aggregated sites. For mixed alkali glasses, the lower field strength cation is accommodated mainly by the low energy, low basicity sites, while the high field strength ion occupies the high energy, high basicity sites [66]. The smaller of the alkali ions have a stronger interaction with the network oxygen dwelling in more covalent sites, while the larger ions with already lower field strength have weaker M-O interactions in more ionic sites [56].

The cation site change with composition, and thus with the nature of the charge offered by the oxygen environment, is well displayed in the binary lithium borate glass absorption coefficient spectra (see Figure 8) [68]. The frequency of the cation motion band maximum increases from below 400 cm^{-1} at low alkali content up to 540 cm^{-1} approaching the orthoborate composition. The infrared spectra become increasingly convoluted with the addition of alkali and subsequent formation of tetrahedral units (refer back to Section 2.2 and Figure 1). At high alkali content, the spectra regain the simplicity seen in the pure boron oxide spectra as N_4 approaches zero and isolated trigonal orthoborate units become the dominant “network” former. A thorough interpretation and discussion can be found in the original text [68].

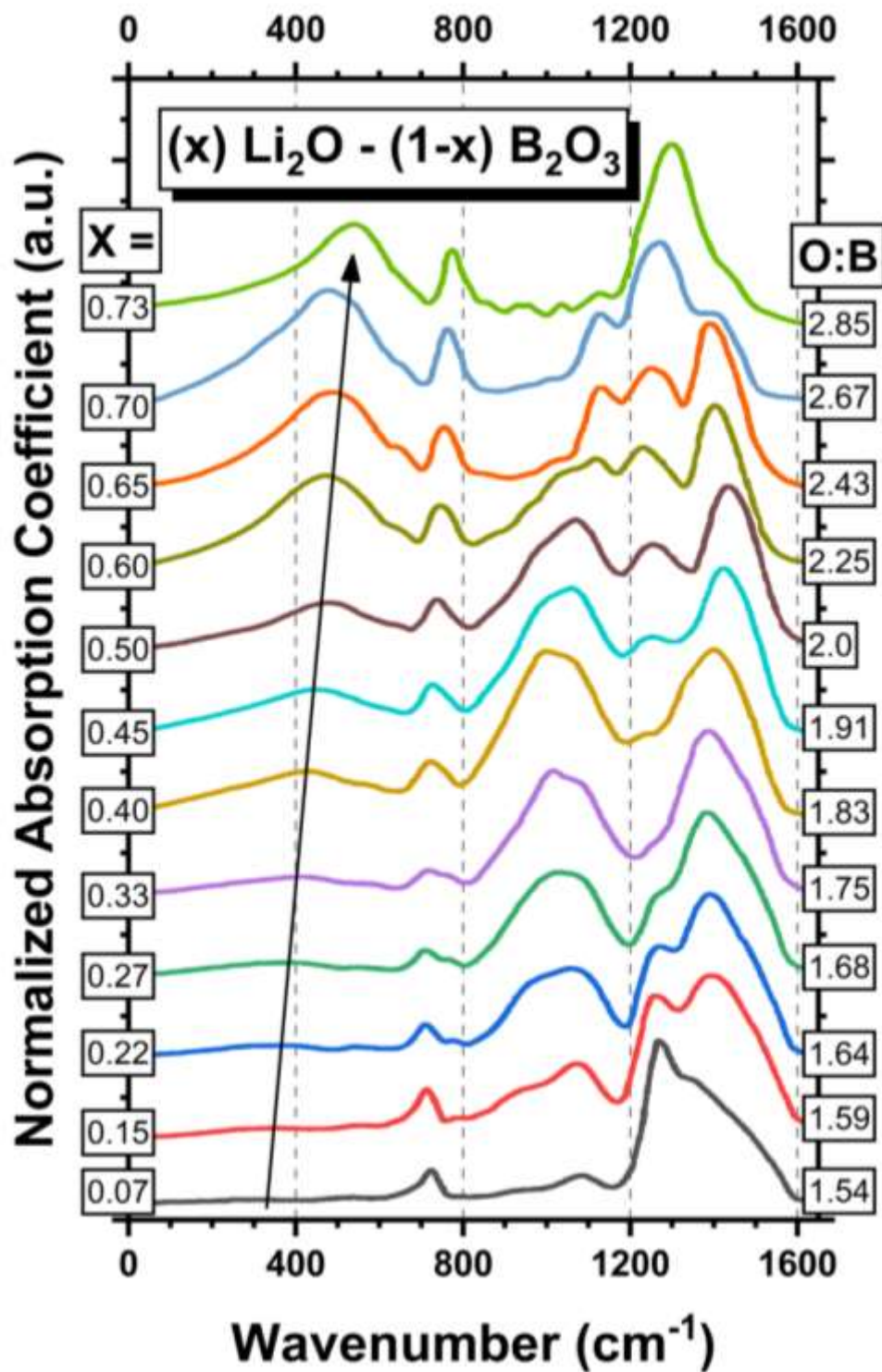
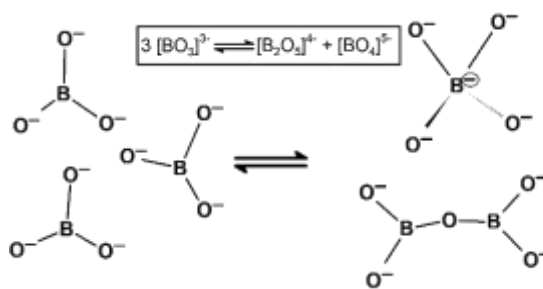


Figure 9. Infrared absorption coefficient spectra for the lithium borate system [68]. Arrow drawn to bring attention to the increasing frequency of the lithium ion motion band.

7. Non-oxygen Anions in Borate Glasses

Borate glasses prepared with high alkali contents have been reported to retain carbonates [21, 43], easily identifiable in the Raman spectra by a sharp peak around 1060 cm^{-1} [59]. Carbonate retention in high basicity borate melts has been reported to be a function of both melt time and temperature, with CO_3^{2-} ion population in the final glass decreasing with either longer melt time or higher melt temperature [100].

The modification of silver borates, $\text{Ag}_2\text{O} - \text{B}_2\text{O}_3$, resembles the modification by monovalent alkali ions discussed earlier up to around the diborate composition. Silver borate glasses doped with AgI were studied as fast ion conduction (FIC) glasses. The pyroborate $2\text{Ag}_2\text{O} - \text{B}_2\text{O}_3$ composition does not form a glass, though addition of AgI induced disproportionation and allowed glass formation [101, 102]. The highly charged borate tetrahedra, $[\text{BO}_4]^{5-}$, known to occur in several minerals (TaBO_4 , NbBO_4) [103, 104], have been reported by Varsamis to exist in $(x)\text{AgI} - (1-x)[0.75\text{Ag}_2\text{O} - 0.25\text{B}_2\text{O}_3]$ orthoborate glasses [105]. The infrared study of silver iodide containing orthoborate glasses displayed presence of both tetrahedral units as well as pyroborate dimers at the orthoborate stoichiometry, $3\text{Ag}_2\text{O} - 1\text{B}_2\text{O}_3$. The occurrence of pyroborate units would necessitate the existence of highly charged species to satisfy the charge valence rule. The existence of the tetrahedra and pyro-dimers was therefore explained by disproportionation at the orthoborate stoichiometry (see Schematic 7). Infrared spectroscopy revealed the silver was coordinated by both oxygen and iodide ions.



Schematic 7. Disproportionation of orthoborate triangles into the pyroborate unit and the isolated BO_4^{5-} unit.

Chloride, like iodide, has been introduced to lithium borate glasses as LiCl for FIC applications [106]. The chloride ions were determined to occupy interstices of the glass network whereby the activation energy governing the mobility of the Li^+ ions decreases resulting in increased conductivity with increased Cl^- content [33].

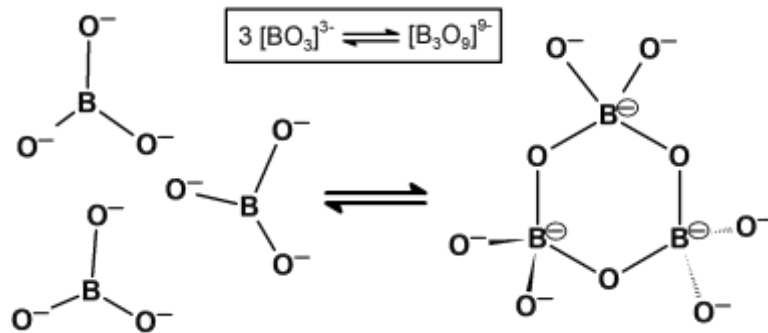
Fluorine on the other hand, forms covalent bonds with boron resulting in mixed oxyfluoride species [107, 108]. Vibrational spectroscopy showed that B-F bonds change bridging oxygen sites and that ring oxygen ions were not replaced. The monovalent F⁻ does not link borate entities together, creating isolated species and decreasing network connectivity. Unlike the higher conductivity observed by addition of other halogens like Cl or I, fluorine addition decreases conductivity as the alkali ion mobility is reduced due to creation of high potential energy sites. The presence of fluorine extends the UV transparency to shorter wavelengths when fluorine atoms substitute for nbO atoms since ultraviolet absorption due to the excitation of the valence electrons of the nbOs is decreased.

The sulphate anion can be dispersed in the interstices of the borate network where its size and charge impact the borate speciation [109]. Vibrational spectroscopy of Li₂O – B₂O₃ glasses containing 17% and 36% Li₂O with Li₂SO₄ added showed the sulphate anion induced the formation of more polar borate groups in both cases. Later study of lithium meta- and pyro- borates augmented with Li₂SO₄ supported the earlier findings [110]. It was concluded that B-O-S connections do not form, but that the pseudospherical SO₄²⁻ anion does effect equilibrium between trigonal and tetrahedral metaborate units (Equation 2). With initial introduction of small amounts of Li₂SO₄ to the Li₂O-B₂O₃ system, the [BØ₄]⁻ population increases but further addition results in the formation of BØ₂O⁻.

8. Second Boron Anomaly

Recently, Winterstein-Beckmann *et al.* reported on two series of strontium borate glasses nominally modified to beyond the orthoborate composition. The (1 – 2x) MO - x[SrO-B₂O₃] (M = Mn, Eu_{2/3}) glasses were observed to contain both trigonal orthoborate monomers, BO₃³⁻, and tetrahedral orthoborate rings, B₃O₉⁹⁻, at high levels of modification [111, 112]. Glass transition temperature measurements for Winterstein-Beckman's highly modified glasses display a second boron anomaly. As x progresses from ~0.5 to 0.25, T_g decreases with increasing modifier and then increases for x=0.2. The increase in the glass transition temperature beyond the orthoborate stoichiometry in the MnSrB system is attributed to the re-establishment of network connectivity in some capacity, as the crosslinking strength of the Mn and Sr ions alone is unlikely to give rise to such

phenomena. The increase in the glass transition temperature at $x=0.2$ coincides with an increase in the relative intensity of the BO_4 band in the infrared spectra. Along with the Raman spectroscopy measurements, the anomalous behavior was concluded to arise from the formation of orthoborate rings comprised of 3 tetrahedral boron each with 2 bO and 2 nbO, $[\text{B}_3\text{O}_6]^{3-}$. These ring structures are well known to occur in the low temperature phase of yttrium orthoborate (YBO_3) as well as in rare earth orthoborates of larger REs, Sm to Yb [113-115]. The formation of the orthoborate ring is made possible by the equilibrium reaction in Schematic 8.



Schematic 8. Equilibrium of orthoborate triangles with the orthoborate ring composed of tetrahedral borates [108].

Conclusion

From bioactive calcium containing glasses to radiation shielding heavy metal oxide glasses and to low melting point sealant glasses, borate glasses provide the answer to a broad range of technical problems. From chemically durable borosilicates to rapidly dissolving borophosphates, boron oxide is an essential additive to complex multicomponent systems. The recent discovery of a second boron anomaly indicates there is still more to discover about the fundamental structure and properties of borate glasses and how these may be utilized as material solutions remains widely open.

Chapter 2

A Quest for Tetrahedral Orthoborate Units in Glasses

1. Hypothesis

The objective of this work was to find diamagnetic glasses containing tetrahedral orthoborate species. Trigonal and tetrahedral orthoborate units are known to exist in crystals, and the trigonal orthoborate unit's occurrence in glasses is well known. Earlier work has shown strong evidence for the existence of tetrahedral orthoborate species based on vibrational spectroscopy and glass transition temperature measurements. These glasses were paramagnetic, prohibiting further investigation with nuclear magnetic resonance spectroscopy.

As discussed in the Background (Chapter 1), the structure of borate glasses usually consists of the basic structural units observed in the corresponding or related crystals. In this work, compositions have been selected based on crystals known to have tetrahedral orthoborate structures. For example, the low temperature phase of yttrium orthoborate consists of the tetrahedral orthoborate rings and yttrium oxide's diamagnetic nature would make glasses containing Y^{3+} measurable by NMR [113, 116].

The melting temperature of YBO_3 is excessively high, and so modifier cations were selected to help glass preparation and to improve glass formation. The binary lithium borate system exhibits the largest glass forming range of the alkali ions. The structure and property data have been reported for decades. Li^+ favors the tetrahedral metaborate more so than the larger alkali ions [8, 32, 46, 55, 56, 58, 59, 64, 68, 99, 117]. There is also a crystalline phase of lithium metaborate that consists of only tetrahedral boron [117].

The binary strontium borate system is also well understood and has a high fraction of tetrahedral boron at the metaborate composition [65]. Strontium diborate consists of all boron in tetrahedral coordination with three coordinated oxygen [118]. Importantly, earlier work evidencing tetrahedral orthoborate units consisting of modifying a binary strontium borate glass with an increasing modified load [111, 112].

Lithium and strontium borates favor B_4 formation in crystalline and vitreous state. $Li_2O - Y_2O_3 - B_2O_3$ and $SrO - Y_2O_3 - B_2O_3$ glasses were thus two systems that might allow for the formation of the tetrahedral orthoborate species.

2. Experimental

2.1 Materials

2.1.1. Reference Materials

Crystalline compounds of LaBO₃, YBO₃, and GdBO₃ were prepared as reference materials. Lanthanum orthoborate is known to consist of only trigonal orthoborate entities while the low temperature phase of yttrium and gadolinium orthoborates is known to consist of only tetrahedral orthoborate entities. Compounds were produced according to the procedure reported by Ren *et al.* [119] with some modification. The La₂O₃ (or Y₂O₃ or Gd₂O₃) was mixed with boric acid in a 1:2.05 molar ratio and placed in a platinum crucible. The crucible was placed in an electrically heated furnace at 550 °C for 30 minutes to decompose the boric acid (Ren *et al.* carried out the decomposition of the boric acid at 500 °C for 2 hours). The crucible was then transferred to a high temperature electrically heated furnace at 1200 °C for 2 hours. The crucible was removed from the furnace and allowed to cool in air. The samples were not further annealed (extended annealing was carried out by Ren *et al.*).

2.1.2. Lithium Yttrium Borate Glasses (LYB)

Samples were prepared by traditional melting between 1150 °C and 1450 °C in a platinum crucible in an electrically heated furnace and then quenched between two metal plates. Initially, many lithium yttrium borates were prepared but the lithium carbonate used, turned out to be contaminated (Appendix A1). The real orthoborate LYB glasses in Section 3.2.2 were later prepared and measured by Nagia Tagiara at NHRF and the absorption coefficient spectra and Raman spectra are reported here.

2.1.3. Strontium Yttrium Borate Glasses (SYB)

Traditional melting of the samples was conducted at temperatures between 1350 °C and 1550 °C in a platinum crucible in an electrically heated furnace and splat quenched between two metal plates. Compositions were chosen according to the formula $(100 - 2x) \text{Y}_2\text{O}_3 - x [\text{SrO} - \text{B}_2\text{O}_3]$, using the melting parameters given in Table 1. For the yttria free sample, $x=50$ corresponds to the stoichiometric strontium metaborate; however, due to the tendency of the this melt to crystallize, 47 SrO – 53 B₂O₃ is taken as the approximate metaborate glass. Throughout this document, especially in figures, this will be designated as $x = 50^*$ where the asterisk denotes the approximation.

Table 2. Composition and Preparation Parameters for Strontium-Yttrium-Borate Glasses.

Y ₂ O ₃ (mol%)	SrO (mol%)	B ₂ O ₃ (mol%)	O:B ratio	Melting Temperature (°C)	Melting Time (min)	T _g (°C)
0	47	53	1.94	1350	20-30	613 ²
5	47.5	47.5	2.16	1350	20-30	630.7
10	45	45	2.33	1350	20-30	631.7
15	42.5	42.5	2.53	1350	20-30	631.5
20	40	40	2.75	1450	20-30	635.3
25	37.5	37.5	3.00	1550	20-30	652.2

Two highly modified SYB glasses were prepared to investigate the impact of higher yttria content and of oxygen to boron ratios exceeding the orthoborate stoichiometry. The formula used was $(100 - 2x) [0.75 \text{ Y}_2\text{O}_3 - 0.05 \text{ BaO} - 0.05 \text{ Cs}_2\text{O} - 0.05 \text{ Rb}_2\text{O} - 0.05 \text{ K}_2\text{O} - 0.05 \text{ Na}_2\text{O}] - (x) [0.9 \text{ SrO} - 1.1 \text{ B}_2\text{O}_3]$ with x selected to be 30 and 33 (see Table 3).

² DSC measurements were conducted in March 2020 during the onset of the COVID-19 shutdown. The T_g measurement of the 47 SrO – 53 B₂O₃ glass was the last to be measured but unfortunately the shutdown prohibited the measurement. This also means that all measurements were only taken once, and thus the reproducibility of the T_g values here is unknown.

The tabled value is from Reference 65. Yiannopoulos, Y.D., G.D. Chryssikos, and E.I. Kamitsos, *Structure and Properties of Alkaline Earth Borate Glasses*. Phys. Chem. Glasses, 2001. **42**(3): p. 164-172.

Table 3. Composition and Preparation Parameters for Overmodified Strontium-Yttrium-Borate Glasses, with x=33 and 30.

Y ₂ O ₃	BaO	Cs ₂ O	Rb ₂ O	K ₂ O	Na ₂ O	SrO	B ₂ O ₃	O:B	Melt Temp (°C)	Melting Time (min)
(mol%)										
25.5	1.7	1.7	1.7	1.7	1.7	29.7	36.3	3.1	1540	15
30	2.0	2.0	2.0	2.0	2.0	27	33	3.4	1540	15

2.1.4. 45 Li₂O – 20 R₂O₃ – 35 B₂O₃ Glasses (LRB)

Orthoborate glasses containing lithium oxide and differing R³⁺ oxides were prepared for R = Y, La, Gd, Eu, and Yb. Some compositions were doped with Tb³⁺ by addition of ~0.5 mol% Tb₄O₇ for time-dependent fluorescence measurements. 5 gram batches were melted in a platinum crucible at 1300 °C and splat quenched between two metal plates.

2.2 Methods

2.2.1 X-Ray Diffraction

XRD was performed using a Bruker D2 Diffractometer with a coupled two theta scan carried out over the range 5° to 75° with a step size of 0.02 at a rate of 1 sec/step.

2.2.2 Vibrational Spectroscopy [120-124]

The complementary techniques of Infrared and Raman spectroscopy were used to investigate the structure. Infrared activity will occur if there is a change in the dipole moment as the structural unit, e.g. molecule, vibrates. If there is a change in the dipole moment, then the molecule will be excited to a higher vibrational energy state by the absorbed infrared radiation. Vibrational modes are Raman active if there is a non-zero value for the change in the polarizability at the equilibrium position of the normal vibration. A vibrational mode may be either Raman active, IR active, both, or neither. The activity is related to the structure's symmetry and so a given molecule will display different vibrational spectra for different structural configurations.

As non-metallic and non-crystalline solids, vibrational spectroscopy is well suited for inorganic oxide glasses because the optical response of the material sheds light on the primary features of the phonon density of states, $g(\nu)$. Single crystals have periodic atomic positions resulting in the so-called Brillouin zones that require the conservation of momentum (\mathbf{k}) in a scattering event. The requirement of \mathbf{k} conservation in single crystals is not applicable to glasses, permitting all local structures in a vitreous material to have an active response to incident light (absorbed photons). First order approximations of optical processes dictate that the energy of the photon absorbed is equal to the energy of the excitation created. For Raman spectroscopy, this means that the shift in frequency is equivalent to the vibrational energy if the mode were IR active. For IR spectroscopy, this means the frequency is linearly proportional to the atomic displacement.

2.2.2.1 Raman Spectroscopy

A molecular vibrational mode is Raman active if the incident light induces a change in the polarizability of the bond. The spectra are measured as the intensity of the scattered light as function of the frequency (energy) shift. The intensity is inversely proportional to the excitation wavelength, such that higher energy (short wavelength) excitation sources

yield a higher intensity signal. The intensity is directly proportional to the number or concentration of scattering molecules as well as the change in polarization. The intensity of the signal given:

$$I \sim I_0 (\tilde{\nu}_o - \tilde{\nu}_j)^4 N \left(\frac{\partial \alpha}{\partial q} \right)^2 \quad (6)$$

Where I_0 is the intensity of the excitation source, $\tilde{\nu}_o$ is the frequency of the laser used to excite the sample, $\tilde{\nu}_j$ is the frequency of the j^{th} vibrational mode, N is the number of molecules (concentration) scattering at a given frequency, and $\left(\frac{\partial \alpha}{\partial q} \right)$ is the change in polarization α with respect to the normal coordinate q . (See Appendix A1 for details regarding Equation 1.)

Two different instruments were used either, (1) Renishaw Raman Spectrometer, $\lambda_{\text{EX}} = 514$ nm, or (2) WITech Alpha300 Raman Spectrometer, $\lambda_{\text{EX}} = 488$ nm. An excitation wavelength of 633 nm was used for Tb³⁺ doped samples as 488 nm was observed to induce strong fluorescence bands. All spectra presented herein are unpolarized. Resolution varied depending on the instrument and configuration.

The SYB glasses are compared to one another by subtracting the minimum intensity value of the measured spectra and then normalizing the area under the curve. Figure 2-1 displays the measured spectra and Figure 2-2 displays the normalized spectra. Band positions were identified by the first derivative of the spectra in OriginLab. Examples are shown for the end member of the SYB glasses in Figures 2-3 and 2-4.

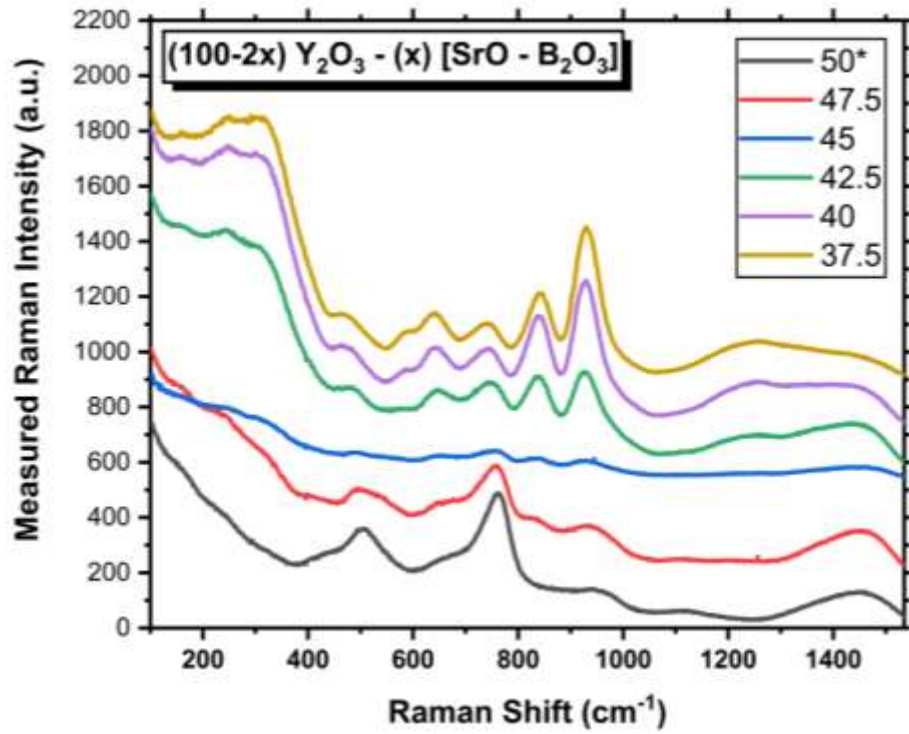


Figure 2-1. As measured Raman spectra, offset for clarity.

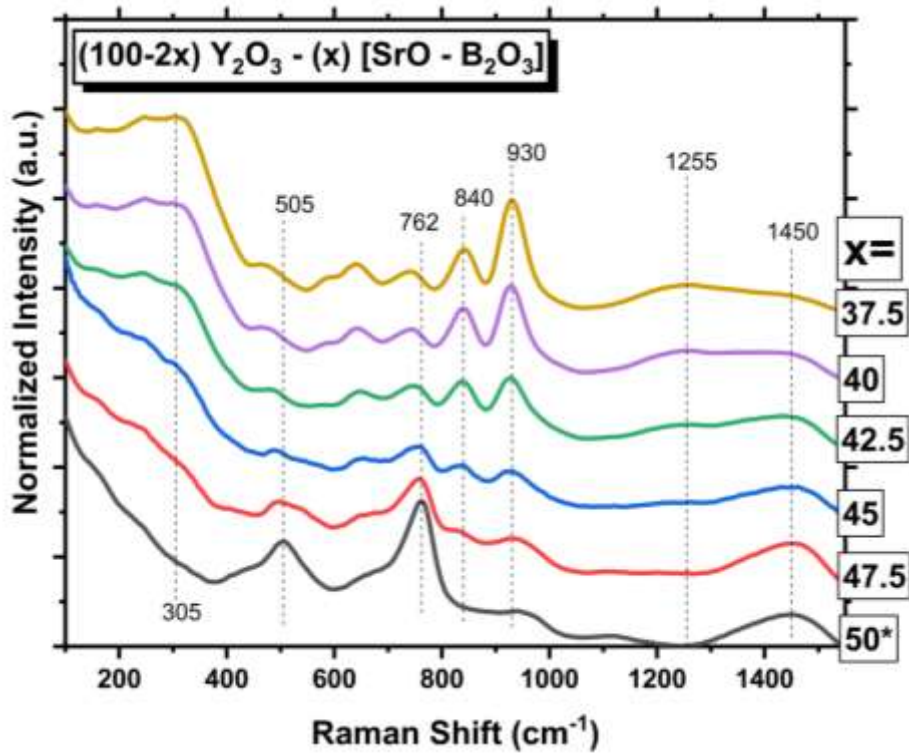


Figure 2-2. Normalized Raman spectra, offset for clarity.

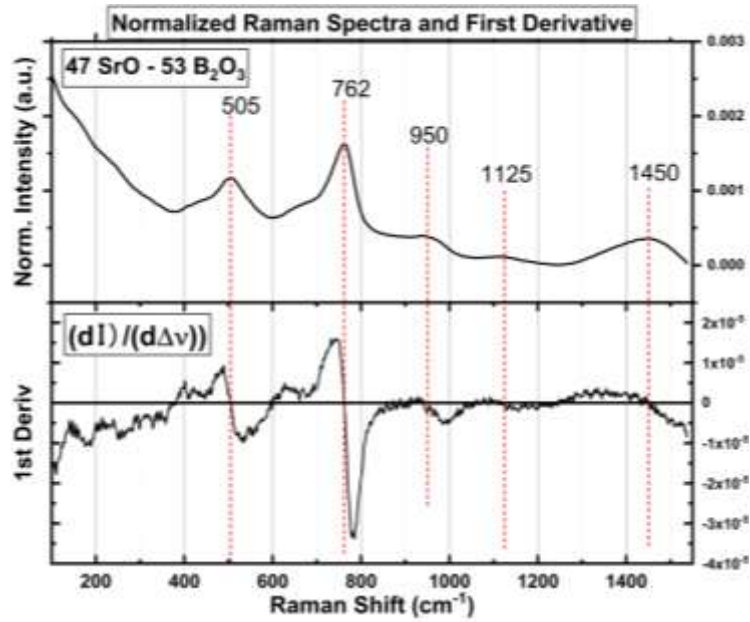


Figure 2-3. Yttrium oxide free, 47 SrO – 53 B₂O₃ normalized Raman spectrum (top) and first derivative (bottom) with dashed lines indicating band positions in the normalized spectrum corresponding to the positions where the first derivative is equal to zero.

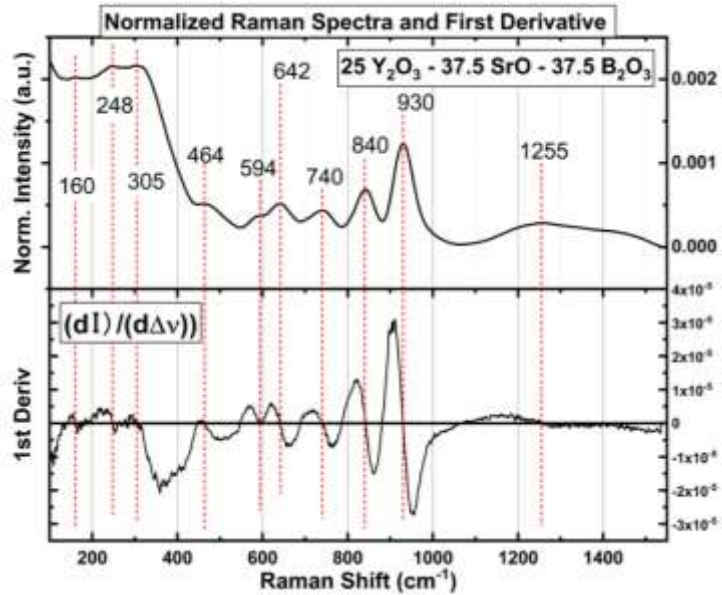


Figure 2-4. 25 Y₂O₃ – 37.5 SrO – 37.5 B₂O₃ normalized Raman spectrum (top) and first derivative (bottom) with dashed lines indicated band positions in normalized spectrum corresponding to the positions where the first derivative is equal to zero.

2.2.2.2 Infrared Reflectance Spectroscopy

Two different infrared spectrometers were used either a Bruker Vortex80 Vacuum IR Spectrometer or Bruker Invenio R Air Purge IR Spectrometer. For the Vortex80, FIR (30-400 cm^{-1}) and MIR (400-7000 cm^{-1}) spectra were measured and merged. For the Invenio R, a single wide range scan between 30-6000 cm^{-1} was measured. In both cases, the resolution was 4 cm^{-1} and many scans (>200) were acquired and averaged. The spectra were recorded in the reflectance mode with an 11° angle of incidence. The resulting spectra are a measure of the reflectivity as a function of frequency, $R(\nu)$, which is the ratio of the intensity of the reflected light to the intensity of the incident light.

$$R(\nu) = \frac{I(\nu)_{\text{reflected}}}{I(\nu)_{\text{incident}}} \quad (7)$$

Interaction between the incident light and a material determine the intensity of the reflected light. Spectral functions of the form

$$fn(\nu) = a(\nu) + i b(\nu) \quad (8)$$

describe the optical response of a solid, where the real part ($\text{Re}[fn(\nu)] = a(\nu)$) is related to the amplitude of the response and the imaginary part ($\text{Im}[fn(\nu)] = b(\nu)$) is related to the phase of the response.

The complex dielectric function is given as

$$\epsilon^C(\nu) = \epsilon_1(\nu) + i \epsilon_2(\nu) \quad (9)$$

The imaginary component, $\epsilon_2(\nu)$, is a dimensionless quantity that is related to the materials microscopic electronic and vibrational modes. The complex quantity $\epsilon^C(\nu)$ relates the polarization wave induced in the solid, $P(\nu)$, with the electric field amplitude of the incident light wave, $E(\nu)$, by

$$P(\nu) = \frac{1}{4\pi} [\epsilon^C(\nu) - 1] E(\nu) \quad (10)$$

The propagation of a light wave in an absorbing solid is dependent on the solid's complex index of refraction, $n^C(\nu)$, which is the square root of the complex dielectric function,

$$n^C(\nu) = \sqrt{\epsilon^C(\nu)} \quad (11)$$

The complex index of refraction is related to the reflectivity, $R(\nu)$, at non-normal incidence angle by the phase-factor component of the reflection, $\theta(\nu)$,

$$R(\nu) = e^{-i2\theta} \left(\frac{n^C-1}{n^C+1} \right)^2 \quad (12)$$

The phase-factor can be determined by the Kramers-Krönig (KK) transformation which was carried out in Bruker *OPUS* software after extrapolating the frequency of the measured reflectance spectra to 0 and ∞ as in Figure 2-5.

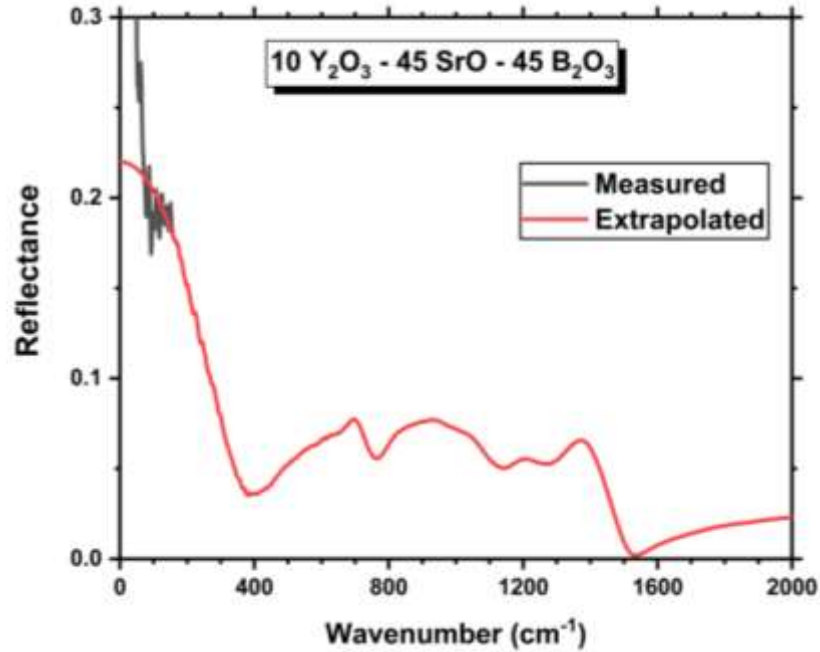


Figure 2-5. Example of FIR extrapolation required for KK transformation.

The KK integral relations give the real and imaginary components of the complex index of refraction when the reflectivity is known for all frequencies,

$$n^c(\nu) = n(\nu) + i \kappa(\nu) \quad (13)$$

This identification allows the calculation of the absorption coefficient as a function of frequency, $\alpha(\tilde{\nu})$, where

$$\alpha(\tilde{\nu}) = 4 \pi \tilde{\nu} \kappa(\tilde{\nu}) \quad (14)$$

Where $\tilde{\nu}$ denotes the frequency expressed in wavenumbers (cm^{-1}) and $\kappa(\tilde{\nu})$ is the extinction coefficient.

The absorption coefficient spectra were calculated using the Bruker *OPUS* software. An example of the relation between the reflectance spectra and the absorption coefficient spectra is given in Figure 2-6 using the extrapolated curve in Figure 2-5 as the reflectance data used for the KK transformation.

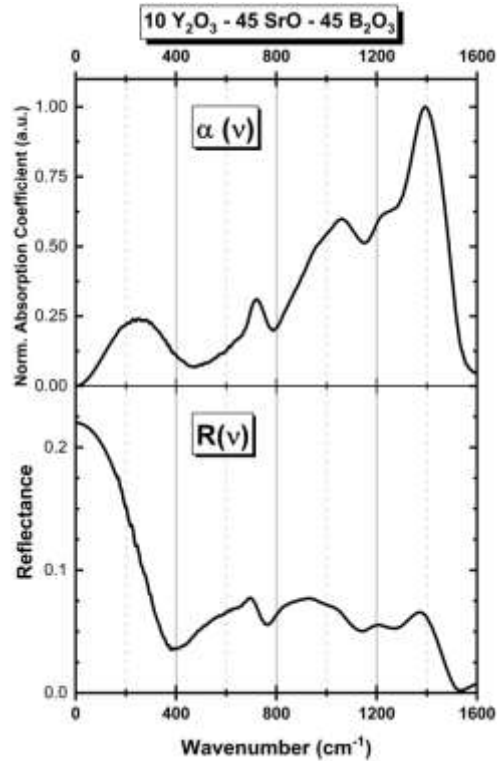


Figure 2-6. Comparison of the reflectance spectrum (bottom) and the obtained absorption coefficient spectrum after KK transformation.

2.2.3 Differential Scanning Calorimetry

Glass transition temperatures were obtained for the series of contaminated LYB glasses on a TA Instruments Q100 DSC using aluminum pans over the temperature range 20 to 550 °C with a heating rate of 10 °C/min. The onset T_g was identified by the *TA Universal* software with an estimated error of +/- 3 °C.

Transition temperatures were obtained for the series of SYB glass using a TA Instruments SDT600 DSC TGA using platinum pans over the temperature range 20 to 1000 °C with a heating rate of 10 °C/min. The onset of the glass transition temperature was determined using the intercept method applied in OriginLab with an estimated error of +/- 3 °C. An example of the intercept method applied to the heat flow data measured by the instrument is shown in Figure 2-7.

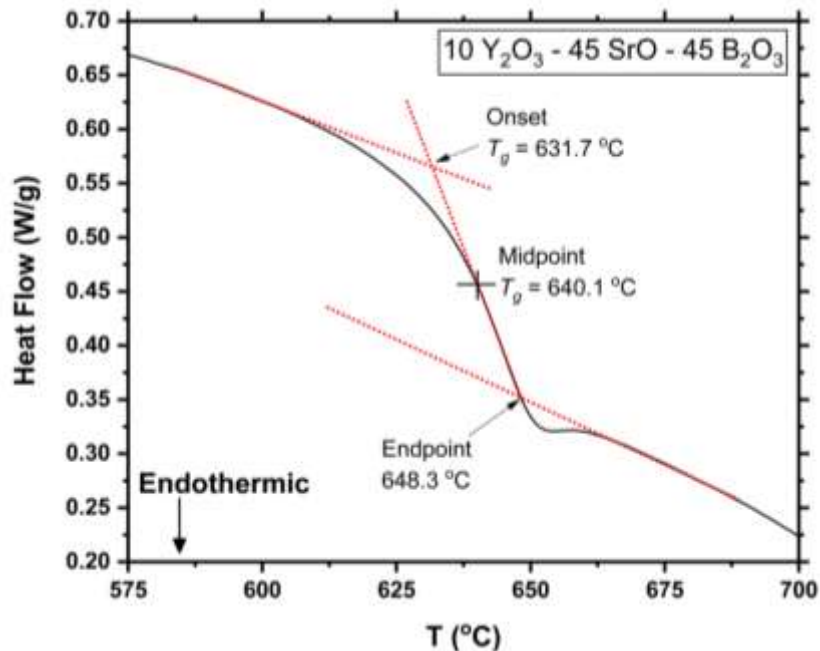


Figure 2-7. Example of intercept method applied to first endotherm in the measured heat flow.

To confirm that the intercept method provided reasonable results, the derivative of the heat flow was taken to identify the inflection point. More information on the results of this procedure along with the complete group of figures pertaining to identification of the transition temperatures can be found in the Appendix (A2).

2.2.4 Time-Dependent Fluorescence Spectroscopy

Fluorescence lifetime measurements were made on a homemade set up constructed by Dr. Andreas Hermann when visiting Alfred in 2019 (Figure 2-8). The set up consists of a UV LED (Roithner LaserTechnik 375 nm LED), LED Power Supply (Roithner LaserTechnik PTDCC/10/ series), Function Generator (Agilent 33120A 15 MHz Function/Arbitrary Waveform Generator), Oscilloscope (Siglent SDS 1000X-E Series Digital Oscilloscope), Computer (SPEX), Monochromator (SPEC), and a Photomultiplier (SPEX).

The SPEC Monochromator is capable of tuning to wavelengths between 400 and 800 nm to observe emissions. The UV LED can be readily swapped out. At the time of this thesis, a 395 nm LED is also available in the lab. The fluorescent intensity is displayed in real time on the oscilloscope. If the sample is visibly fluorescent, excellent lifetime

measurements with low noise can be made by allowing the oscilloscope to average several hundred cycles. The measurements are saved to a USB inserted into the oscilloscope. The user then simply has to subtract the baseline and normalize the intensity. Plotting the intensity on a \log_{10} scale permits the identification of the fluorescent lifetime by selecting the time passed for the intensity to reach $(1/e)$ the initial intensity, where e is the natural number.

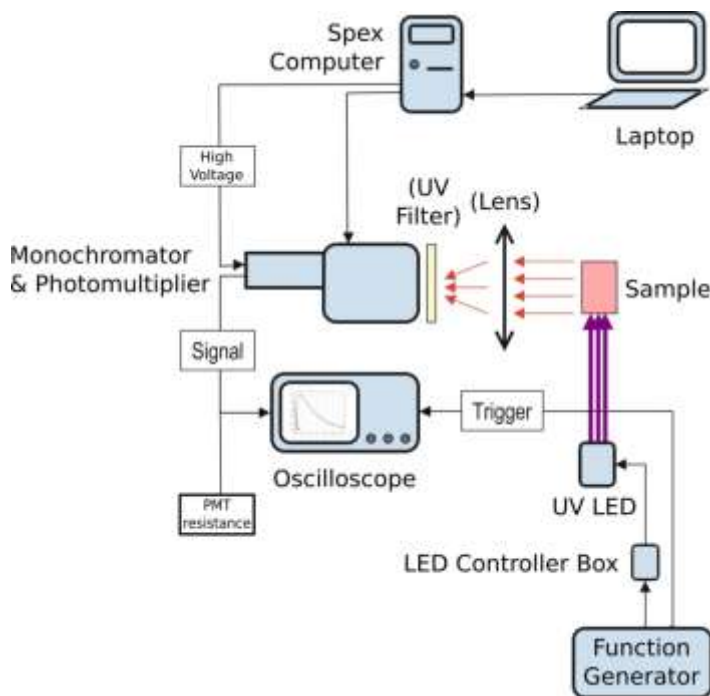


Figure 2-8. Fluorescence lifetime set-up by Andreas Herrmann.

2.3 Software

The following software were used throughout this thesis for the stated purposes:

2.3.1 Origin Lab- Graphing, Analysis, Differentiation, Integration

2.3.2 Bruker OPUS- Infrared data acquisition and handling, KK Transformation

2.3.3 TA Universal- DSC data acquisition and analysis

2.3.4 Project Five- WITech Spectrometer measurements and data conversion

2.3.5 WiRE- Renishaw Spectrometer measurements and data conversion

2.3.6 PDF-4 - Crystallography database software

2.3.7 SPEX Instrument Control – Time-dependent fluorescence measurements

3. Results

3.1 Orthoborate Reference Materials

3.1.1 X-Ray Diffraction

The crystallographic phases of the orthoborate references were confirmed by X-Ray diffraction. Figure 3-1 contains the measured powder diffraction patterns. The PDF that the measured data was checked for agreement with, is given above the measured pattern, on the right-hand side.

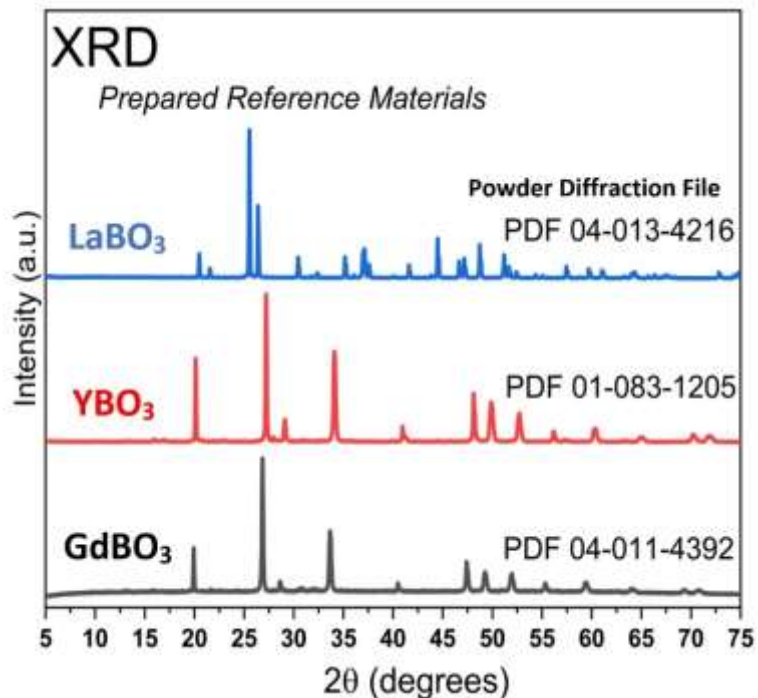


Figure 3-1. X-Ray diffraction data of the prepared polycrystalline orthoborates.

3.1.2 Raman Spectroscopy

The Raman spectra of the orthoborate reference materials are shown in Figure 3-2. The prominent feature of LaBO₃ is the sharp band at around 930 cm⁻¹ belonging to the symmetric stretch of the BO₃³⁻ unit. The bending modes of the trigonal orthoborate unit are observed around 600 cm⁻¹ while the asymmetric stretch is seen above 1200 cm⁻¹. YBO₃ and GdBO₃ have spectral features characteristic of the B₃O₉⁹⁻ ring. These features are the

terminal stretch $\sim 1000\text{ cm}^{-1}$, ring stretching $\sim 830\text{ cm}^{-1}$, ring breathing at $\sim 410\text{ cm}^{-1}$ and $\sim 510\text{ cm}^{-1}$, and terminal bending at $\sim 260\text{ cm}^{-1}$ [111, 112].

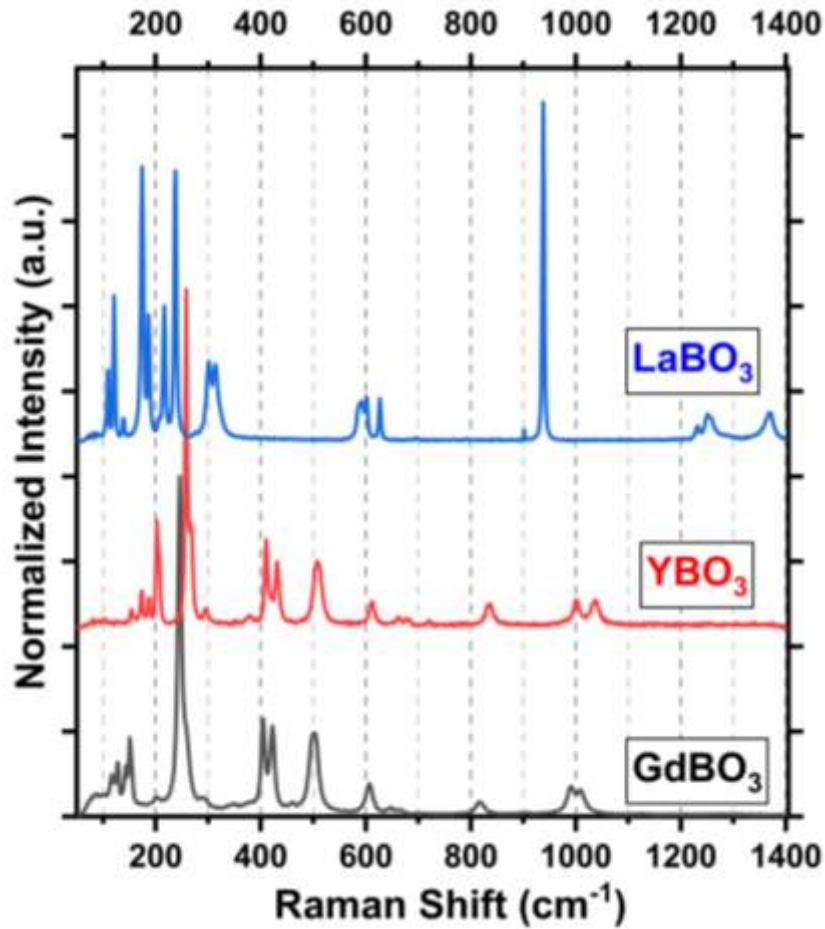


Figure 3-2. Raman spectra of the prepared polycrystalline orthoborates.

3.1.3 Infrared Spectroscopy

The infrared absorption coefficient spectra of the orthoborate reference compounds are shown in Figure 3-3. LaBO_3 contains only trigonal boron-oxygen units as suggested by the absence of spectral activity in the $800\text{--}1200\text{ cm}^{-1}$ range. The characteristic asymmetric stretch of BO_3^{3-} is indicated by the maximum at 1326 cm^{-1} while the in-plane bending and out-of-plane bending are seen at 612 cm^{-1} and 730 cm^{-1} , respectively. Both YBO_3 and GdBO_3 contain only tetrahedral boron-oxygen units, $[\text{B}\text{O}_2\text{O}_2]^{3-}$, arranged in $\text{B}_3\text{O}_9^{9-}$ rings, as seen by the absence of spectral activity above 1200 cm^{-1} where the asymmetric stretch of $\text{B}_3\text{--O}$ bonds appears. The ring stretching and terminal stretching modes are contained in

the high frequency band between 800-1200 cm^{-1} while the ring and terminal bending modes are observed in the low frequency region between 250-450 cm^{-1} .

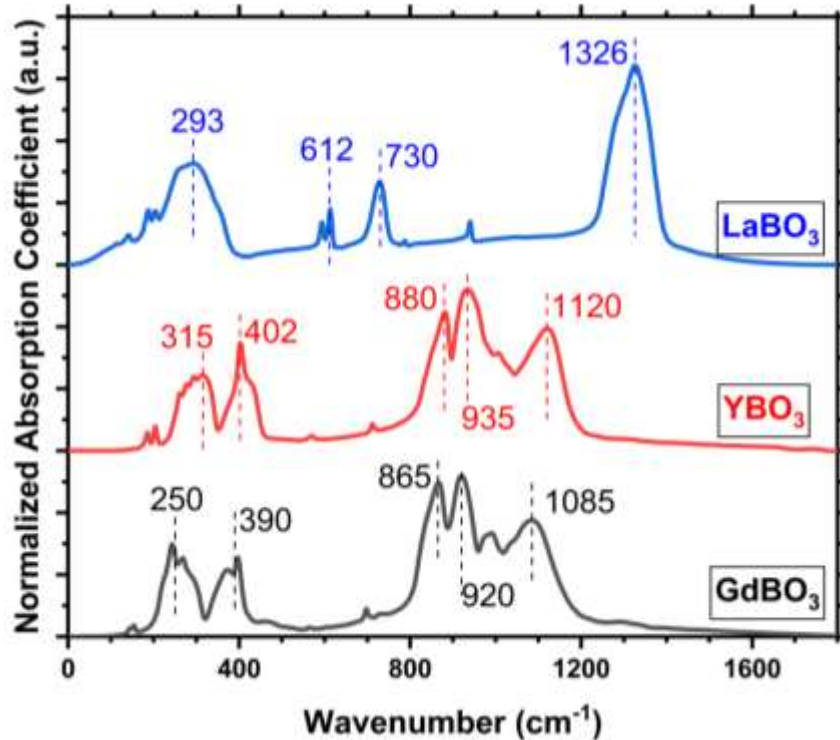


Figure 3-3. Infrared absorption coefficient spectra of the prepared polycrystalline orthoborates.

3.2 Lithium Yttrium Borates (LYB)

3.2.1 LYB samples with contaminated lithium carbonate

Details regarding the contaminated lithium carbonate can be found in the Appendix (A3). There was some deviation from the expected form for the IR spectra and a brief discussion on this matter can also be found in the Appendix (A4). The X-Ray diffraction measurements on the series of glasses that were prepared to be orthoborate glasses are shown in Figure 3-4. As seen in the Appendix figures, the glasses are under modified and the real modification level is most probably between a metaborate and pyroborate composition. At any rate, Figure 3-4 shows that for low levels of Y_2O_3 the materials are amorphous. For the sample with the highest yttria content, “x=18”, the glass was partially

crystallized. The crystallite peaks match those of the YBO_3 reference compound as illustrated in Figure 3-4.

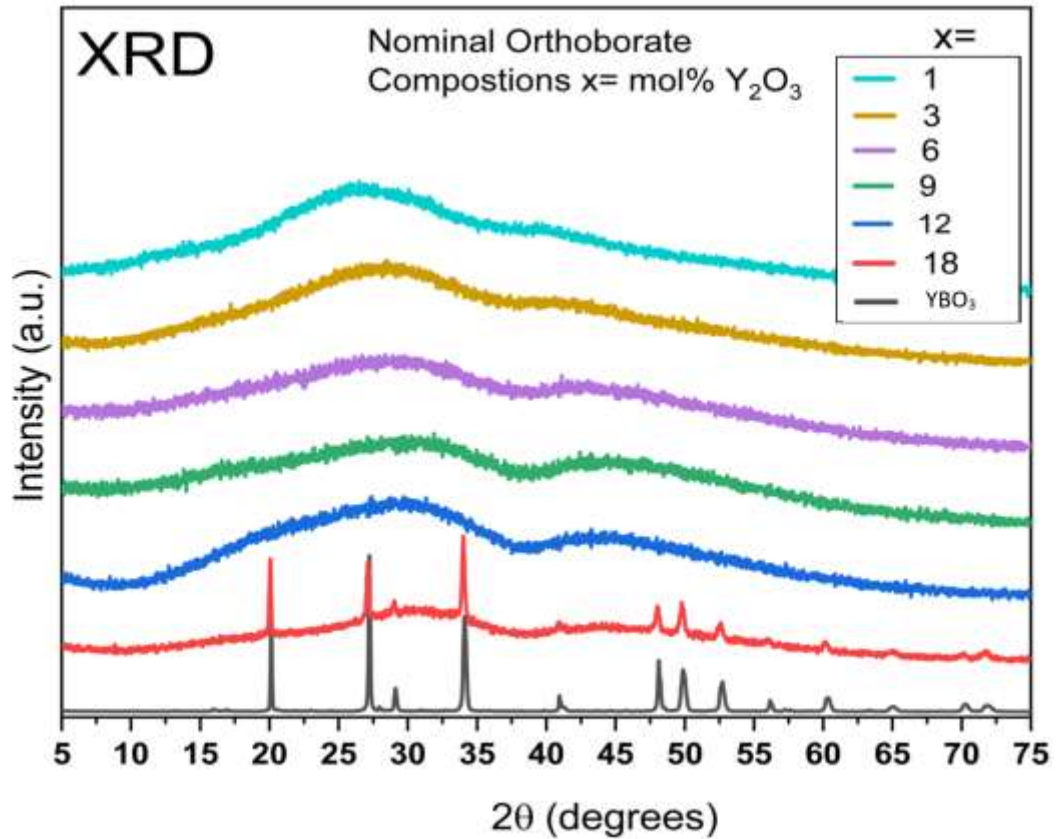


Figure 3-4. X-Ray diffraction results for LYB glasses containing an increasing amount of yttrium oxide.

Figure 3-5 plots the glass transition temperatures for the same samples in Figure 3-4 as a function of Y_2O_3 content in the nominal composition. Increasing the yttria content is seen to increase the glass transition temperature for all compositions. The highest T_g recorded corresponds to the glass with the highest yttria content that was partially crystallized. The T_g is still below 475 °C.

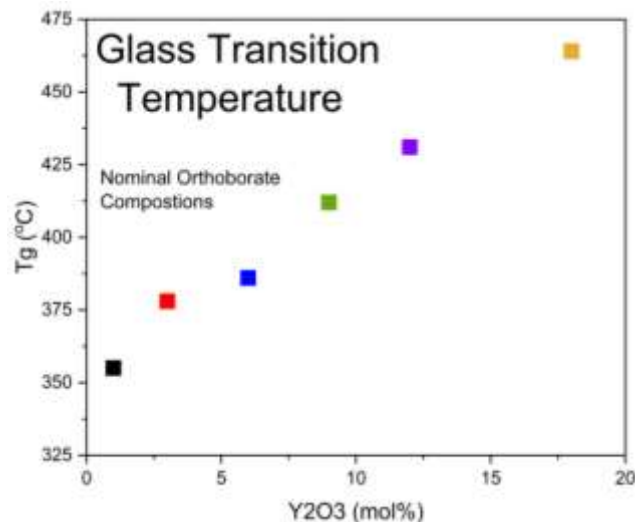


Figure 3-5. Glass transition temperature of glasses plotted versus nominal Y_2O_3 content.

The crystallization was apparent to the unaided eye. The crystallites and the surrounding vitreous material were investigated with Raman spectroscopy. Image 1a – 1f show the spots at which Raman spectra were taken. The spectra corresponding to these locations are shown in Figure 3-6 and Figure 3-7. The former cross-references the different spots with the YBO_3 reference compound showing that the crystallites are indeed comprised of $B_3O_9^{9-}$ rings as XRD suggested. Figure 3-7 highlights the borate units observable in the vitreous regions as well as the position of the Y – O stretching band.

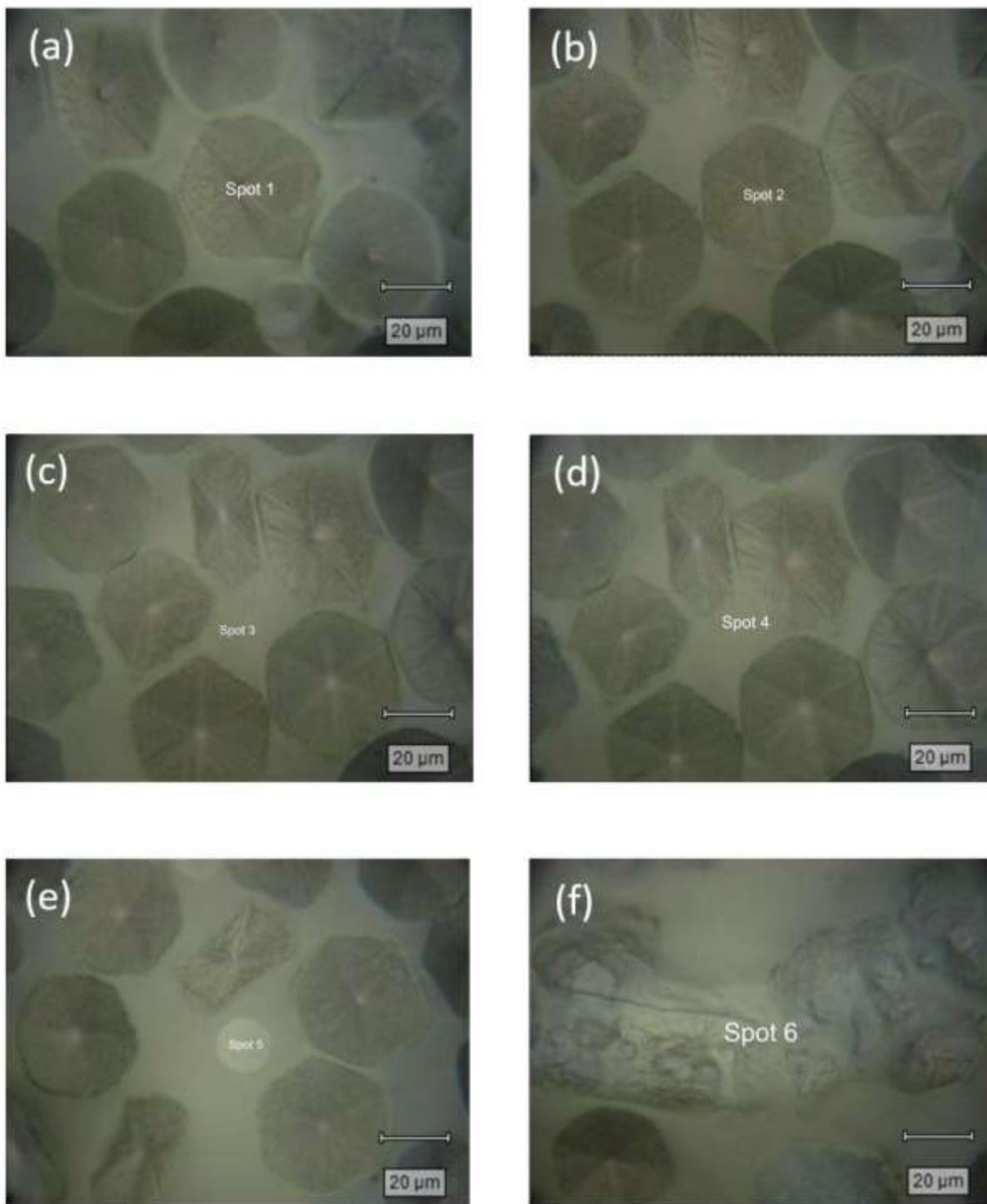


Image 2 (a – f). Spots of partially crystallized glass corresponding to locations that the Raman spectra in Figure 3-6 and Figure 3-7 were recorded at.

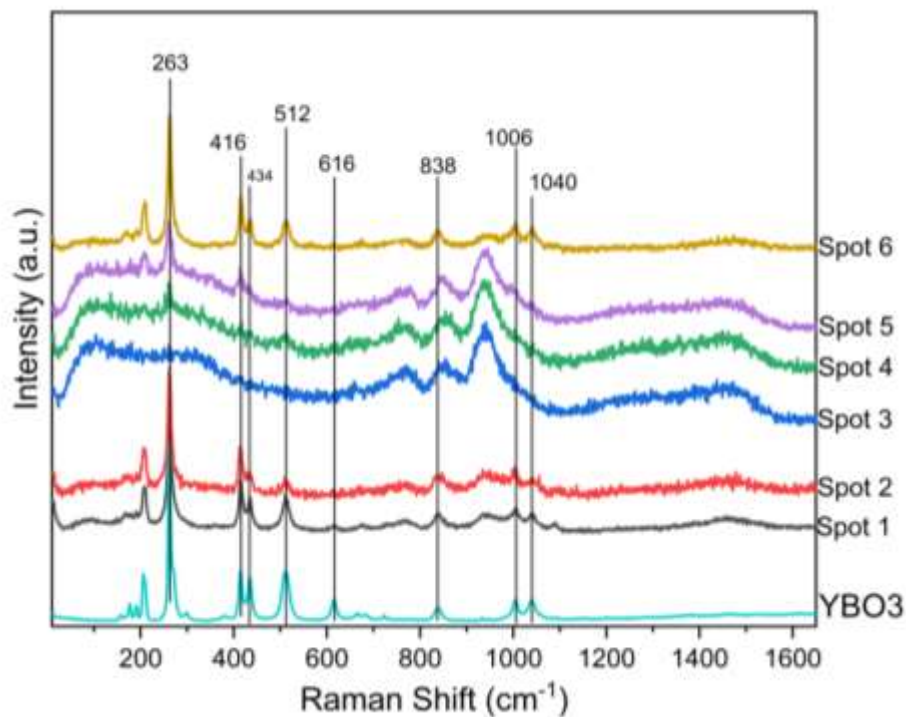


Figure 3-6. Raman spectra of spots in Image 1 with respect to YBO₃ reference material spectra.

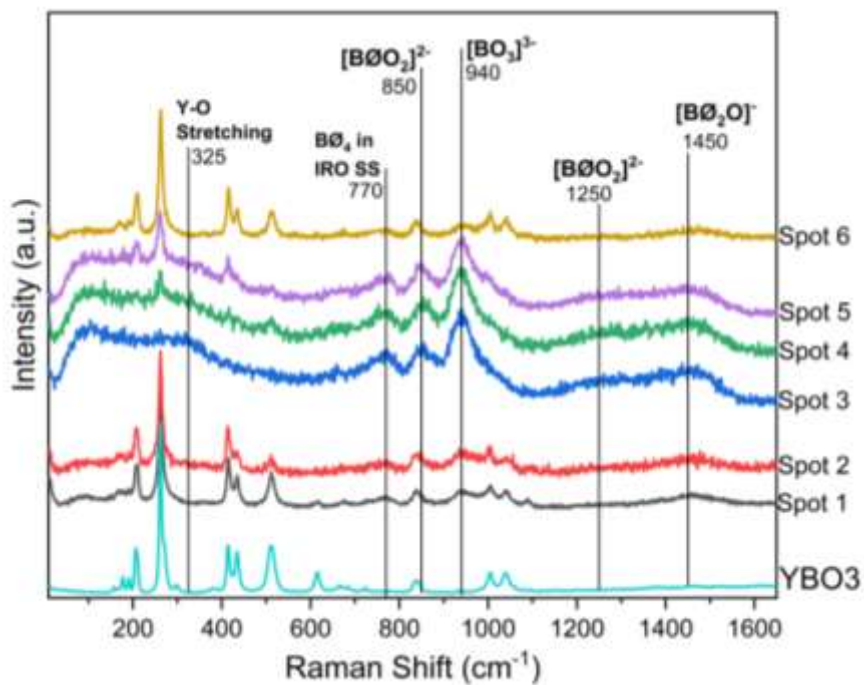


Figure 3-7. Raman spectra of spots in Image 1 with borate units identified.

3.2.2 LYB glasses

The Raman spectra for some lithium yttrium borate glasses approaching and at the orthoborate stoichiometry are shown in Figure 3-8 compared to the spectra for LaBO_3 and YBO_3 . The melts partially crystallized upon cooling and the spectra of the crystallization is also shown.

The spectrum of glass for the composition of O:B = 2.75 contains peaks due to the presence of trigonal orthoborate species (940 cm^{-1} , 755 cm^{-1} , and 640 cm^{-1}) as well as trigonal pyroborate units (840 cm^{-1} , 1250 cm^{-1}) [111]. Trigonal pyroborate units may exist as terminal units of larger borate configurations, such as metaborate chains, or as $\text{B}_2\text{O}_5^{4-}$ units referred to as pyroborate dimers. The $\text{B}_2\text{O}_5^{4-}$ unit persists after the borate network has been depolymerized and has a characteristic feature in the Raman spectra at around 840 cm^{-1} resulting from the symmetric B – O – B stretch. The absence of any band at 840 cm^{-1} in the glassy spectra of the compositions with O:B = 3, along with the remaining features associated with BO_3^{3-} units indicate that at O:B = 3, the glassy LYB consists of only trigonal orthoborate units. Thus, at O:B = 3, the high frequency envelope is only made up of contributions from the asymmetric stretch of BO_3^{3-} units.

The crystallization product in the sample of O:B = 2.75 appears to be $\text{B}_3\text{O}_9^{9-}$ rings, the same as for the sample discussed in Section 3.2.1. The crystallization in the 30 mol% Y_2O_3 orthoborate contains the characteristic ring & terminal modes of the $\text{B}_3\text{O}_9^{9-}$ orthoborate ring as well as a sharp peak at 940 cm^{-1} characteristic of BO_3^{3-} orthoborate triangles.

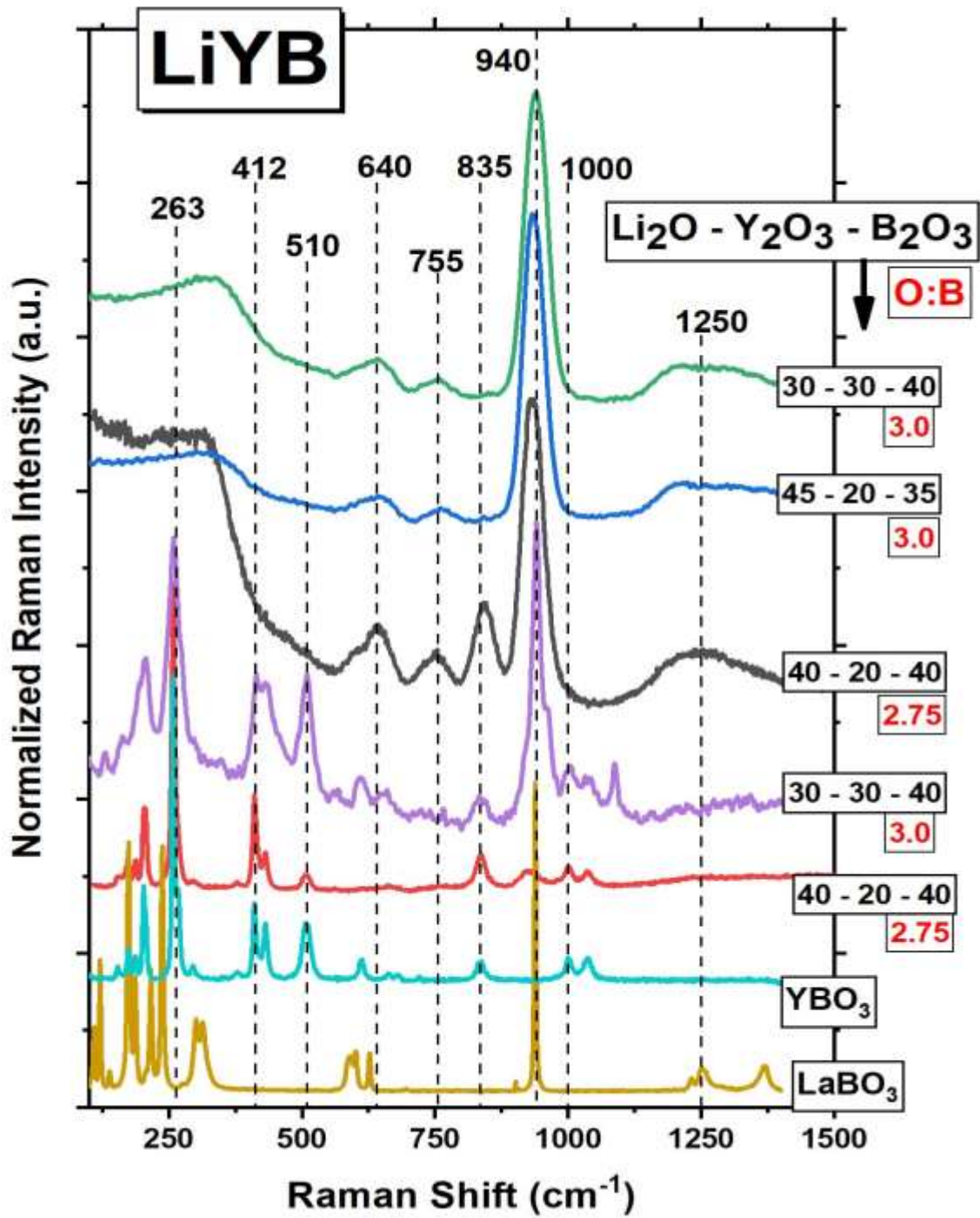


Figure 3-8. Raman spectra of lithium yttrium borate glasses and their crystallization encountered during quenching compared to LaBO₃ and YBO₃ reference material spectra.

The infrared absorption coefficient spectra for the orthoborate glasses in Figure 3-8 are compared to the absorption coefficient spectrum of LaBO₃ in Figure 3-9. The spectra have three main features easily identified in common – a band of medium intensity at 745 cm⁻¹, a very weak feature at 935 cm⁻¹, and high frequency envelope between 1100-1400 cm⁻¹. These features agree with the Raman spectra in that these glasses are composed entirely of trigonal borate units. At lower frequencies, the glasses have a broad envelope with strong activity at 380 cm⁻¹ and 500 cm⁻¹ associated with the Y³⁺ and Li⁺ motion, respectively [68, 111]. The high frequency shoulder of the cation motion band contains the in-plane bending mode BO₃³⁻, designated at 640 cm⁻¹ here and observed at around 612 cm⁻¹ in the spectra of LaBO₃ in Figure 3-3.

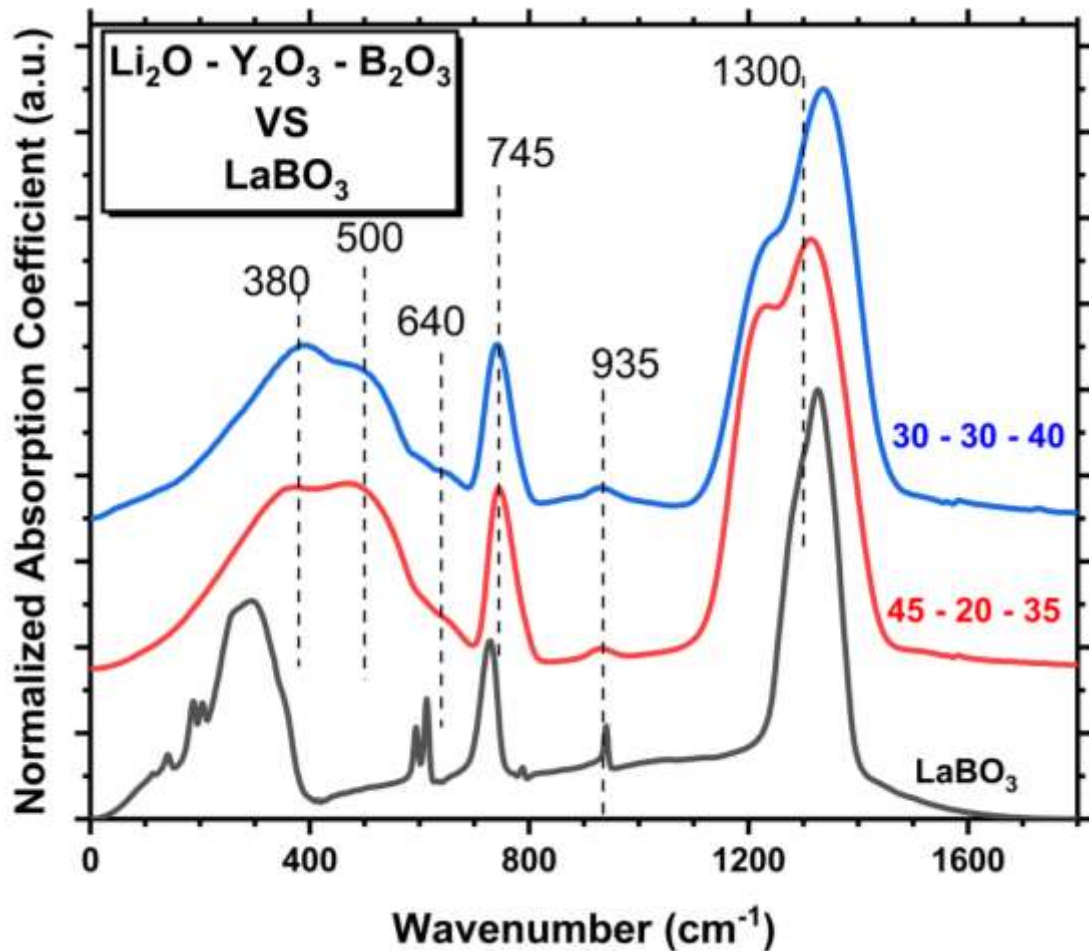


Figure 3-9. IR absorption coefficient spectra of lithium yttrium orthoborate glasses compared to LaBO₃ reference compound.

The Raman spectra for the orthoborate glasses in Figure 3-8 are compared to the Raman spectra of LaBO_3 in Figure 3-10. The spectra are characterized by their sharp band at 940 cm^{-1} . Activity around 640 cm^{-1} is observed in both the LYB glasses and the LaBO_3 spectra while the weak feature at around 760 cm^{-1} is only seen in the spectra of the LYB glasses. The two high frequency bands in the LaBO_3 compound are observed in the glasses as broad, continuous overlapping bands. In the LYB orthoborate glasses, the weak feature $\sim 1550\text{ cm}^{-1}$ is likely due an overtone of the out-of-plane mode [59] as if it were indeed an asymmetric stretch feature, the IR band would extend out to this frequency region but it does not. The $\sim 1550\text{ cm}^{-1}$ band in the Raman spectra could also be a combination band arising from the in-plane bending mode at 640 cm^{-1} and the symmetric stretching mode at 940 cm^{-1} .

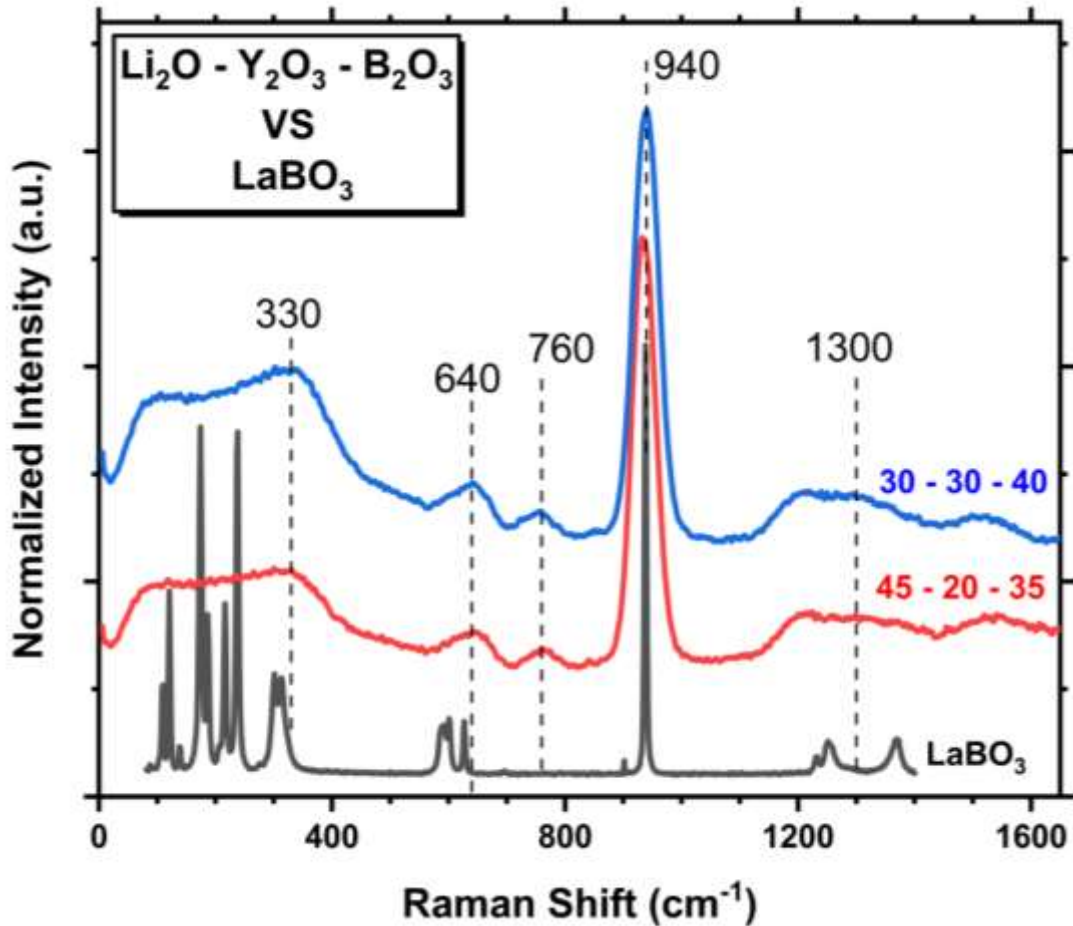


Figure 3-10. Raman spectra of lithium yttrium orthoborate glasses compared to LaBO_3 reference material.

3.3 Strontium Yttrium Borates (SYB)

3.3.1 Strontium Europium Orthoborate (SEB)

The primary objective of this investigation was to produce diamagnetic glasses, thus suitable for NMR spectroscopy, containing tetrahedral borate units with non-bridging oxygen ions. Earlier work provided evidence for $B_3O_9^{9-}$ rings in strontium europium borates melted in a reducing atmosphere, by using a silicon carbon (SiC) crucible. A SEB composition was melted with $25 Eu_2O_3 - 37.5 SrO - 37.5 B_2O_3$ (O:B = 3) in a platinum crucible to not reduce any europium to the paramagnetic Eu^{2+} form. The melt was splat quenched rapidly and most of the melt crystallized. A thin layer of glass on the surface was obtained. The Raman spectrum was recorded and is compared in Figure 3-11 to almost the same composition melted in a reducing environment. It is noted that spectrum in the top of Figure 3-11 (black) corresponds to an X-Ray amorphous sample from the literature [111] while bulk crystallization occurred in the sample prepared in this study using a platinum crucible, bottom of Figure 3-11 (red). The glass layer obtained from melting the strontium europium orthoborate composition in a platinum crucible is comprised of only trigonal orthoborate species. The spectrum can readily be explained by the four fundamental vibrations of the BO_3^{3-} unit as indicated in the figure. An infrared spectrum could not be measured for the SEB glass prepared in this study due to the very small sample obtained, its irregular geometry, and the lack of access to a micro-IR instrument.

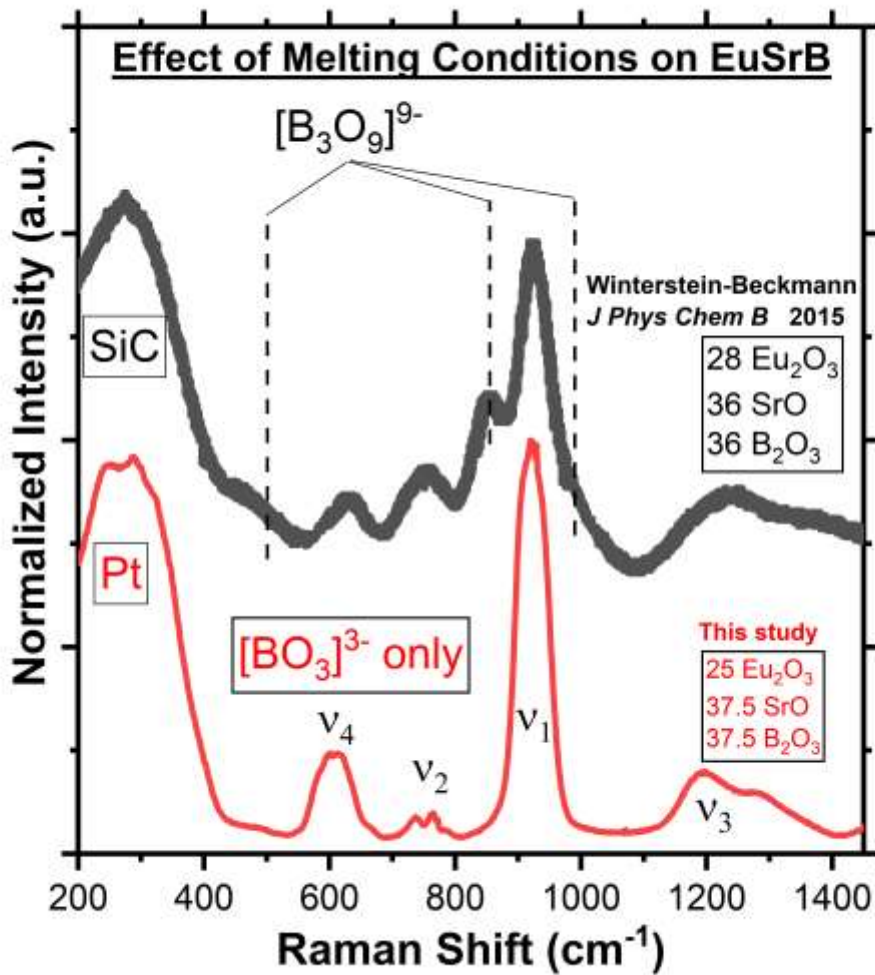


Figure 3-11. Spectra of strontium europium orthoborates melted under different atmospheric conditions and in different crucibles.

3.3.2 Strontium Yttrium Borates (SYB)

The normalized Raman spectra of the glasses obtained from melting the compositions in Table 1 are shown in Figure 3-12. In the mid-frequency region, the band at 762 cm^{-1} loses intensity with increasing yttria content. At the same time, bands at 840 cm^{-1} and 930 cm^{-1} appear and the latter becomes the dominant band in this region at high yttria content, signaling the depolymerization of the borate network into charged trigonal pyro- and ortho-borate units. In the high frequency region, the asymmetric $B_3 - O$ stretch band shifts down in frequency from a maximum at 1450 cm^{-1} to a maximum at 1255 cm^{-1} . In the low frequency region, a shoulder at around 305 cm^{-1} develops as Y_2O_3 is added corresponding to $Y - O$ stretching.

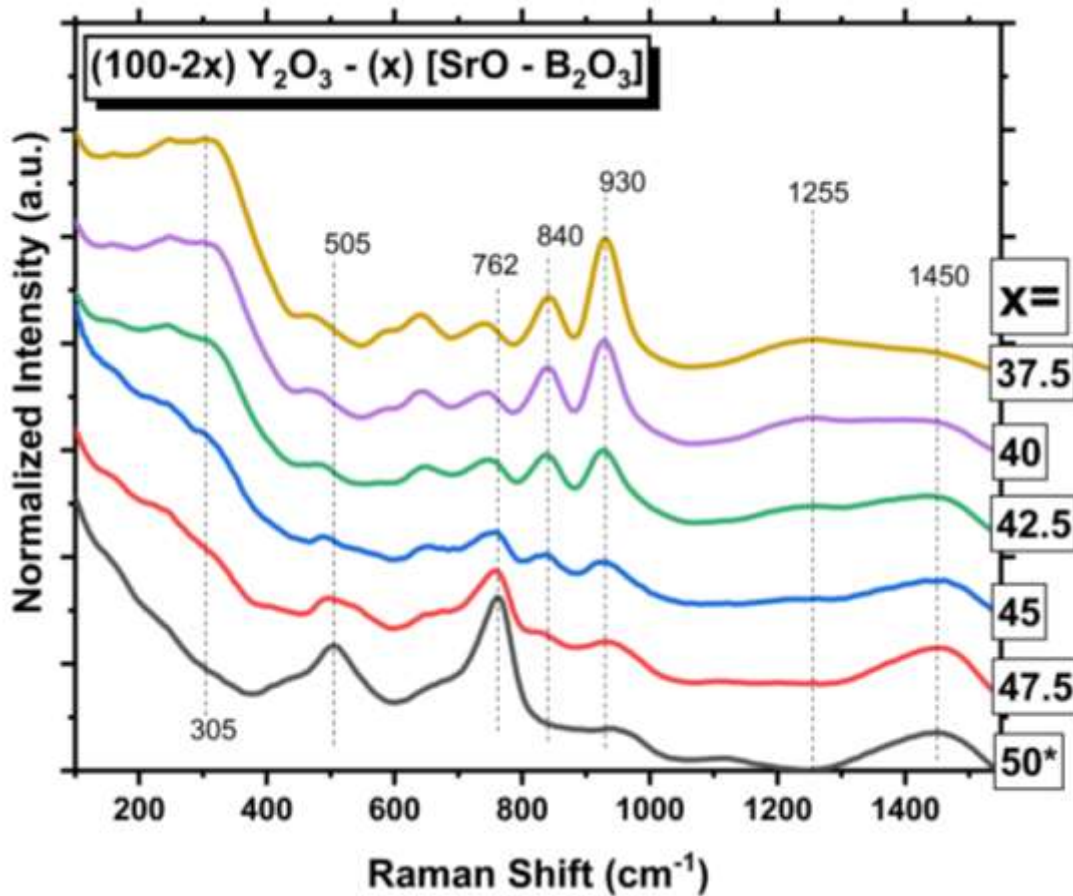


Figure 3-12. Normalized Raman spectra of strontium yttrium borate glasses.

The normalized infrared absorption coefficient spectra of the glasses obtained from melting the compositions in Table 1 are shown in Figure 3-13. The band between 800-1200

cm^{-1} in $x = 50^*$ marked at 1005 cm^{-1} continuously loses relative intensity indicating the destruction of tetrahedral $[\text{B}\text{O}_4]^-$ borate species as Y_2O_3 is added [64]. The high frequency envelope downshifts from 1394 cm^{-1} in $x=50^*$ to a maxima at 1347 cm^{-1} with a shoulder at $\sim 1226 \text{ cm}^{-1}$ in $x=37.5$. The band at 715 cm^{-1} in the yttria free glass shifts to higher frequencies while yttria is added and reaches 733 cm^{-1} for 25 mol% Y_2O_3 . A small feature at 640 cm^{-1} develops as the oxygen to boron ratio is increased. Finally, the cation motion band shifts from 180 cm^{-1} in the yttria free glass to 323 cm^{-1} as the population of Sr^{2+} atoms decreases and the number of Y^{3+} atoms increases.

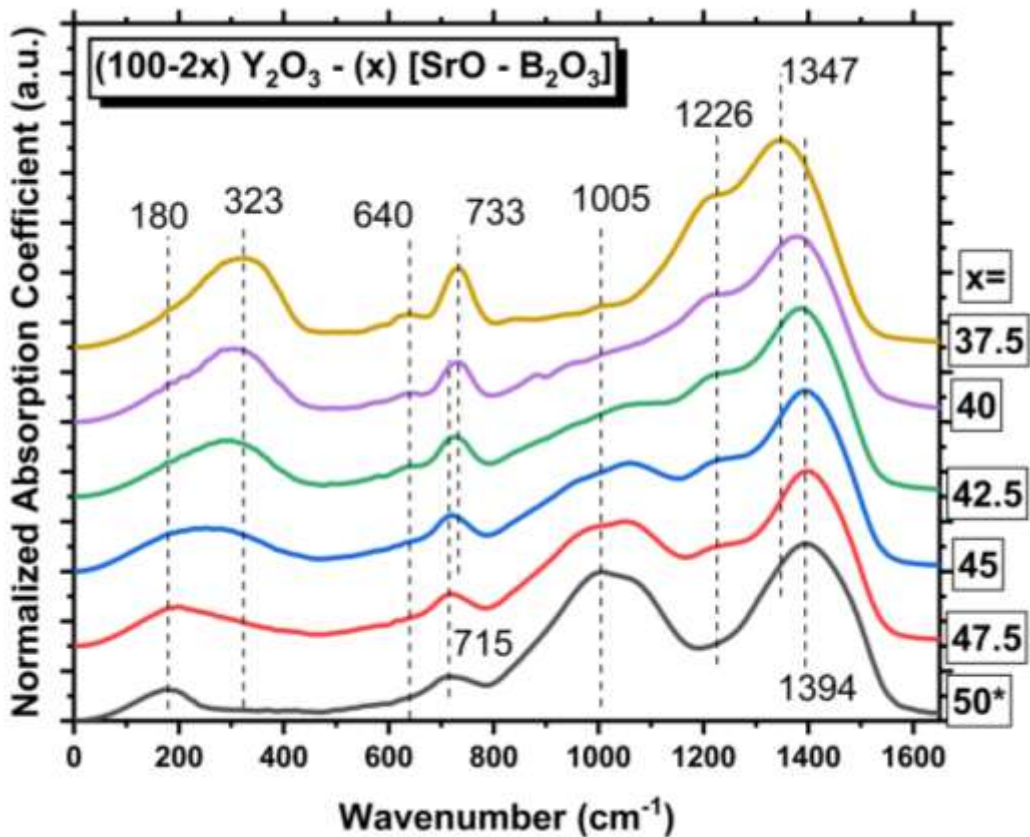


Figure 3-13. Normalized infrared absorption coefficient spectra of strontium yttrium borate glasses.

In the previous studies of SrMnB [112] and SrEuB [111], as Mn or Eu were added to the SrB, the glass transition temperature decreased initially and then increased at higher modifier loads, parallel to the presence of tetrahedral orthoborates, $[\text{B}\text{O}_2\text{O}_2]^{3-}$,

reestablishing connectivity between boron atoms. The step size for increasing the modifier content in this study was smaller than in the SrEuB study. The intention was to provide a greater number of data points to track ‘anomalous’ glass transition temperature behavior related to the connectivity of the borate network. It is recalled here that the glass transition temperature is not only dependent on the degree of polymerization of the network formers, but also on the strength of the modifier-oxygen bonds.

For the strontium yttrium borate glasses of this study, the heat flow as a function of temperature measured by differential scanning calorimetry is shown in Figure 3-14 over the temperature range 500-1000 °C. The first endotherm signifying the glass transition occurred in the interval 600-700 °C for all glasses and is highlighted in Figure 3-15. The glass transition temperature is seen to stay about the same for glasses containing 5, 10, and 15 mol% Y_2O_3 and then increases for both 20 and 25 mol% Y_2O_3 glasses. (See A2 for details)

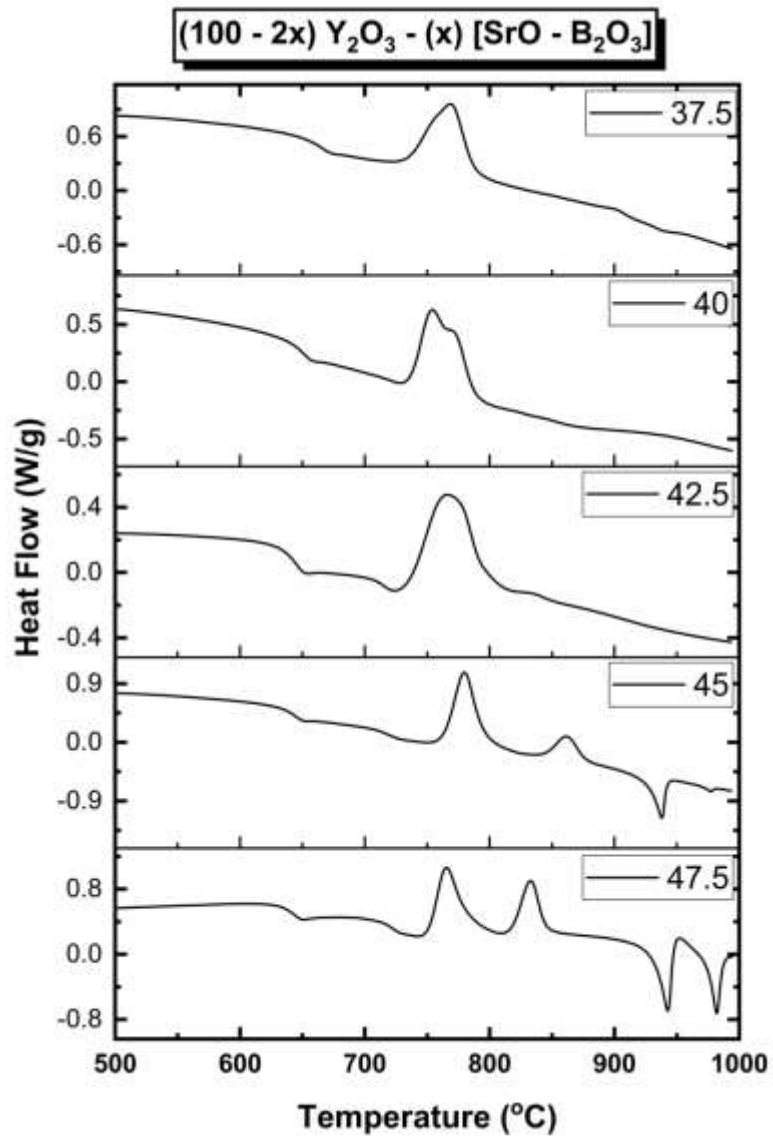


Figure 3-14. Differential scanning calorimetry data for strontium yttrium borate glasses over the range 500-1000 °C.

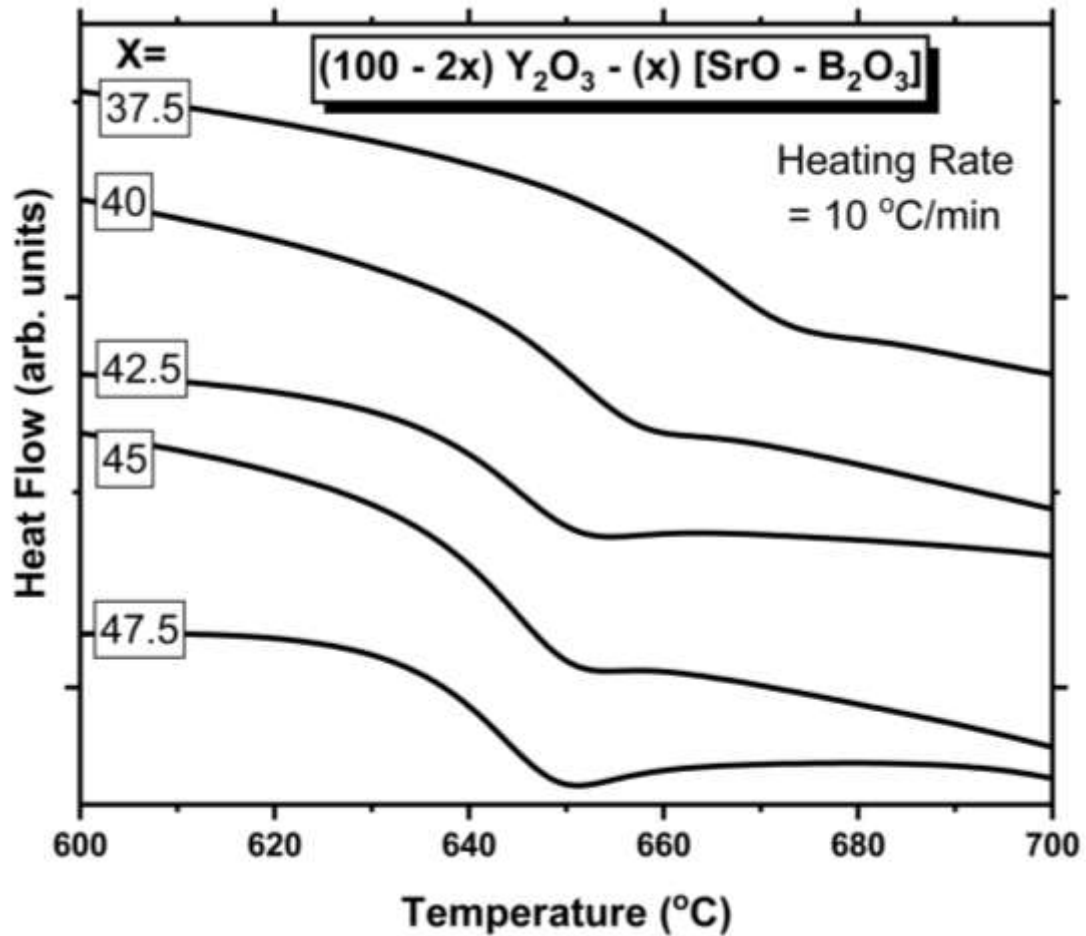


Figure 3-15. Differential scanning calorimetry data for strontium yttrium borate glasses over the range 600-700 °C.

3.3.3 Overmodified Strontium Yttrium Borates (*om-SYB*)

The orthoborate composition in 3.3.2 was “ $x=37.5$ ”. The batch needed the highest temperature accessible in order to melt. Even at 1550 °C, a fully homogenous melt was not achieved. The resulting glass is apparently undermodified given the presence of pyroborate units, possibly due to the fact that not all the Y_2O_3 melted congruently or that YO_n clusters might have formed. The sample obtained was also partially crystallized. It was noted that the Raman spectra of SYB $x=37.5$ resembled the SEB melted under reducing conditions.

The presence of tetrahedral boron in the previous work on Mn/Eu Strontium Borates appeared at oxygen to boron ratios above the orthoborate stoichiometry. With the equipment on hand, obtaining a SYB glass as in Section 3.3.2 with more than 25 mol% Y_2O_3 was doubtful. A different route to overmodify the system was needed to see if the

system would change its course of modification for higher oxygen to boron ratios and yttria content.

Consideration was given to the observed clustering of Mn in the SrMnB series as well the multiple valence states of Eu in the SrEuB series. Taking into account the ‘confusion principle’ thought to assist glass formation in ionic or multicomponent metallic glasses, it was thought that creating a highly modified composition might reveal the nature of how the SYB system will evolve with high Y_2O_3 content and oxygen to boron ratio beyond the orthoborate composition. Glasses obtained from compositions with oxygen to boron ratios of 3.1 and 3.4 (Table 2) were studied from predominantly crystallized melts. The Raman (Figure 3-16) and IR (Figure 3-17) spectra possess the same characteristic features discussed for the LYB orthoborate glasses (Fig 3-9 & 3-10).

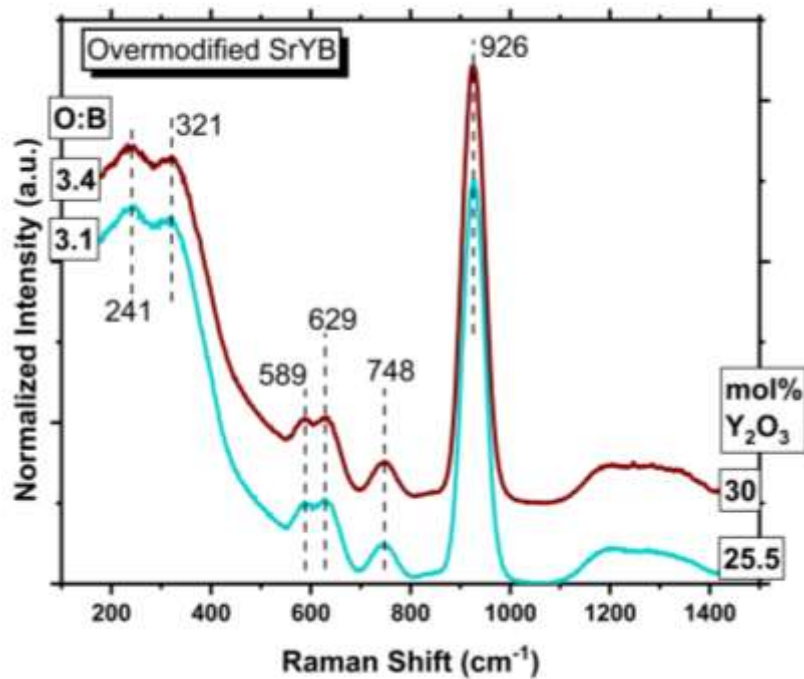


Figure 3-16. Raman spectra of overmodified strontium yttrium borates.

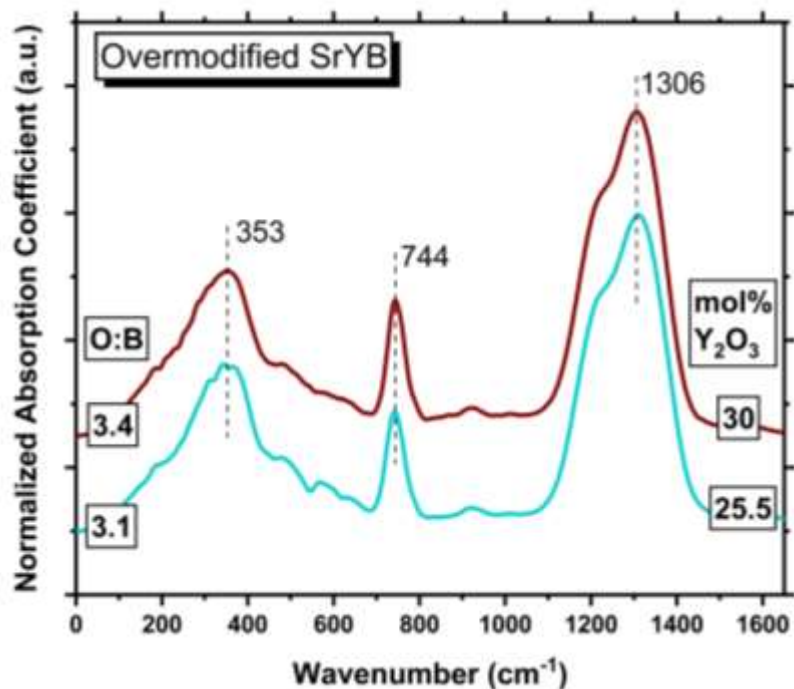


Figure 3-17. Infrared spectra of overmodified strontium yttrium borates.

3.4 Orthoborate $\text{Li}_2\text{O} - \text{R}_2\text{O}_3 - \text{B}_2\text{O}_3$ (LRB)

To investigate the generality of the observed behavior of Y^{3+} cations in Sr^{2+} and Li^+ borate glasses, orthoborate glasses ($\text{O/B}=3$) were prepared with composition $45 \text{Li}_2\text{O} - 20 \text{R}_2\text{O}_3 - 35 \text{B}_2\text{O}_3$ for $\text{R} = \text{Y}, \text{La}, \text{Gd}, \text{Eu},$ and Yb . The Raman (Figure 3-18) and IR (Figure 3-19) show that the borate speciation, BO_3^{3-} , at the orthoborate composition investigated, is independent of the type of R^{3+} cation. Multiple quenches of the La_2O_3 containing melt were attempted and crystallization took place every time. This is well observed in the sharp bands of the Raman and IR spectra, particularly in the low frequency ranges.

Tb^{3+} has been suggested to be a sensitive structural probe in borate and borosilicate glasses [125]. The fluorescence decay of Tb^{3+} doped samples ($\text{Y}, \text{La}, \text{Gd}$) are shown in Figure (3-20). The decays are mono-exponential as seen in the linear nature with the logarithmic y-axis. The lifetime τ is approximately 2.2 milliseconds for all samples supporting the independence of the borate structure on the R^{3+} cation.

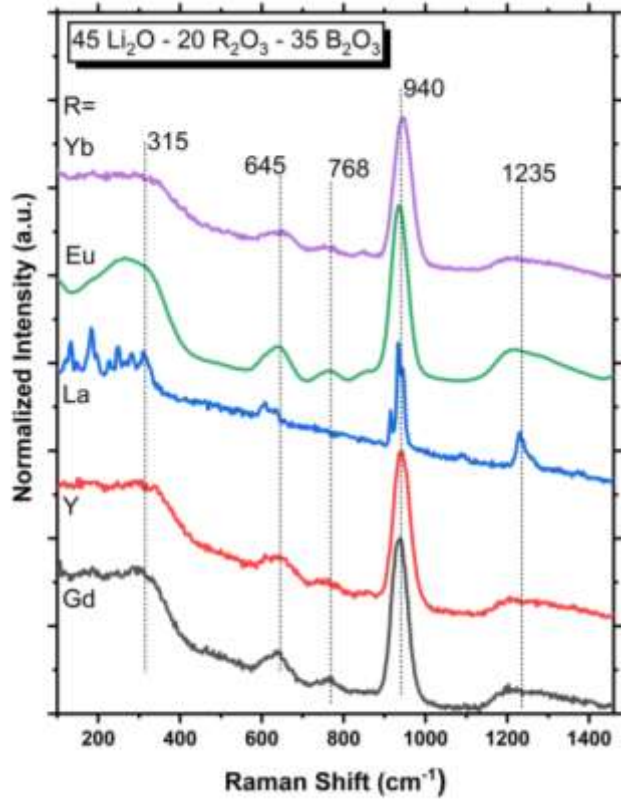


Figure 3-18. Raman spectra of $45 \text{Li}_2\text{O} - 20 \text{R}_2\text{O}_3 - 35 \text{B}_2\text{O}_3$ orthoborates.

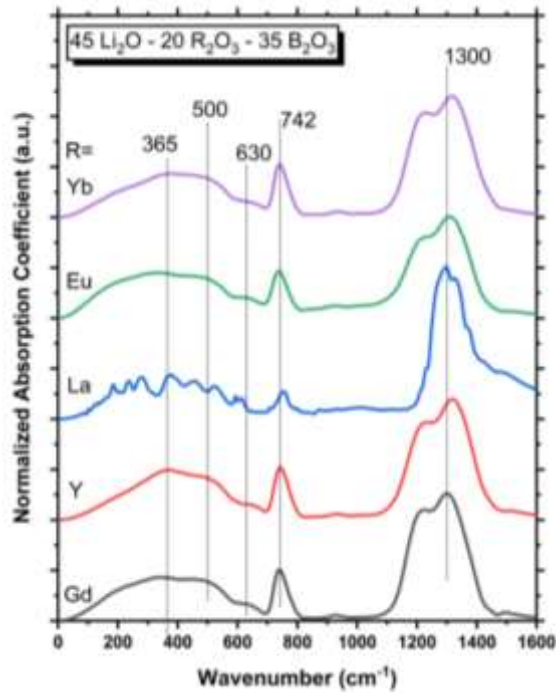


Figure 3-19. Infrared spectra of $45 \text{Li}_2\text{O} - 20 \text{R}_2\text{O}_3 - 35 \text{B}_2\text{O}_3$ orthoborates.

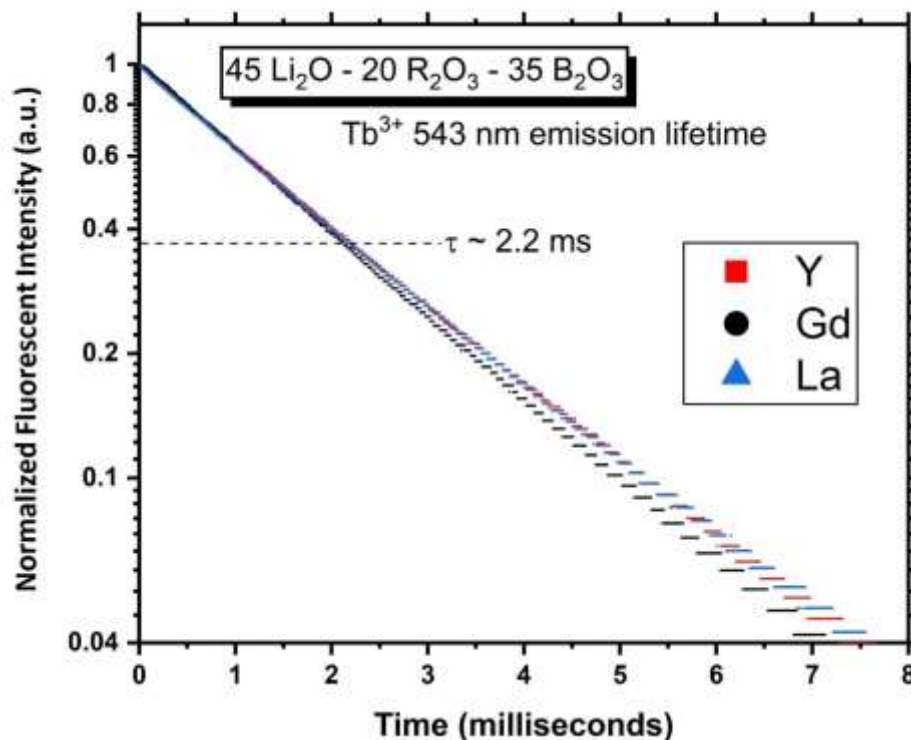


Figure 3-20. Fluorescence decay of Tb^{3+} doped $\text{Li}_2\text{O} - \text{R}_2\text{O}_3 - \text{B}_2\text{O}_3$ samples.

4. Discussion

4.1 Lithium Yttrium Borates

The Raman spectra in Figures 3-7 and 3-8 display the stark difference between the vitreous and crystallization tendencies of yttrium in lithium borate glass that was unexpected. The spectra show that the glassy state consists of only trigonal orthoborate units, while in glasses whose T_g is below the $\text{HT} \rightarrow \text{LT}$ phase transformation temperature of YBO_3 ($T = 596.5\text{ }^\circ\text{C}$) [116], tetrahedral orthoborate ring crystallites are found.

No evidence of tetrahedral orthoborate rings occurring in bulk quantity in the vitreous state is evident in Figures 3-9 and 3-10, noting also that – contrary to EuSrB glasses [111] - extensive over-modification was not possible without crystallization. Comparison of the glassy Raman and Infrared spectra of lithium yttrium orthoborate glasses with 20 or 30 mol% Y_2O_3 content with the Raman and Infrared spectrum of LaBO_3 indicates the short-range order of the three systems is identical. Interestingly, in both the

Raman and IR spectra for the vitreous lithium yttrium orthoborate, all fundamental modes of the BO_3^{3-} anion are observed. For the XY_3 structure, this is realized for trigonal configurations with much lower than D_{3h} symmetry indicating that the majority of the BO_3^{3-} units present in the glass are no longer planar. The lower site symmetry of the trigonal orthoborate anion in glasses and the subsequent Raman activity of four fundamental modes appears to be characteristic to vitreous orthoborates that contain only this species (see Figure 3-8, 3-10, 3-11, 3-16, 3-18).

4.2 Strontium Yttrium Borates

4.2.1 Borate Network – Raman Spectroscopy

First, attention is brought to Figure 3-11 which displays the influence of the melting conditions on the strontium europium borate system. The results affirm a previous study by Shafer [80] in europium borates prepared in carbon crucibles where it was found the presence of Eu^{2+} , formed by the reducing conditions, yielded a larger glass forming region than other rare earth elements. The fact that the bulk of the melt crystallized and only a surface layer of glass resulted from melting in a platinum crucible, while the carbon crucible melt from [111] resulted in an X-Ray amorphous glass, provides supporting evidence to this proposition.

In the SYB series, the glass transition temperature measured by differential scanning calorimetry stayed approximately the same for 5, 10, and 15 mol% Y_2O_3 content then rose for 20 mol% Y_2O_3 and again for 25 mol% yttria. This is telling of the strong crosslinking ability of yttria in the strontium borate system. The increase in T_g coincides with the complete depolymerization of the borate network observable in Figure 4-1 and will be discussed in detail now.

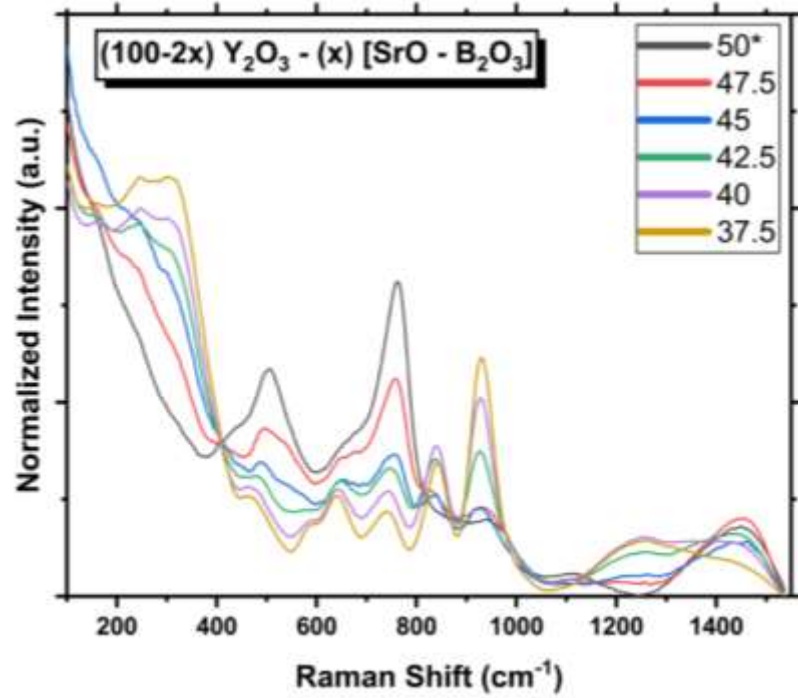


Figure 4-1. Overlapped normalized Raman spectra of Strontium Yttrium Borate glasses.

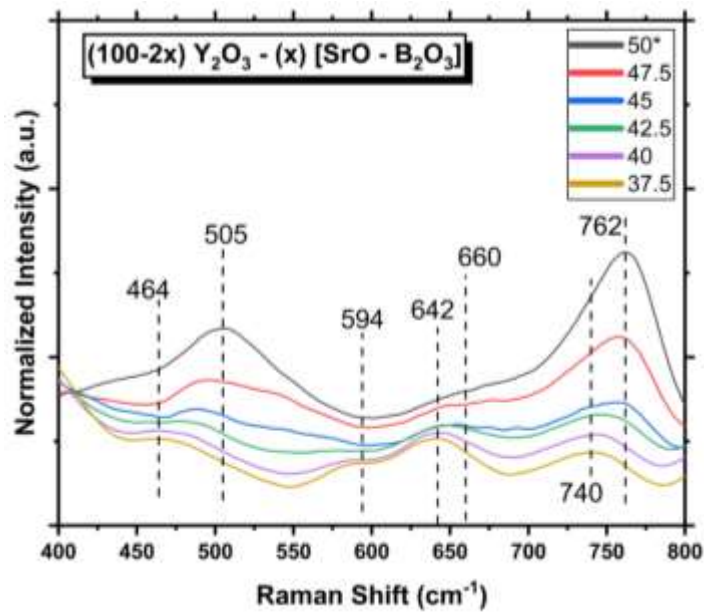


Figure 4-2. Raman spectra, overlapped and normalized, of Strontium Yttrium Borate glasses over the interval 400 – 800 cm^{-1} .

The decrease in the relative intensity of the band at 762 cm^{-1} signals the destruction of 6-membered rings containing tetrahedral boron units (Figure 4-2). The shoulder of this feature in 50^* at 700 and 660 cm^{-1} can be attributed to the deformation of trigonal metaborate chains [117]. These features give way to the bending modes of BO_3^{3-} units as features develop at 740 cm^{-1} (out-of-plane bending) and 642 cm^{-1} (in-plane bending). The shoulder of the 642 cm^{-1} band at 594 cm^{-1} may arise from the mixture of the two modifying cations or band splitting. According to Drago [121], the ν_4 vibrational mode of a trigonal polyhedron with low symmetry is expected to split into two bands.

The feature at 505 cm^{-1} is associated with tetrahedral boron [59]. The 505 cm^{-1} band together with the 762 cm^{-1} band as well as the features at 950 cm^{-1} (Figure 4-3) and 1125 cm^{-1} (Figure 4-4) are likely diborate rings, $[\text{B}_4\text{O}_7]^{2-}$, consisting of two linked BO_4 that share two BO_3 units [72]. The band at 505 cm^{-1} gives way to a feature at 464 cm^{-1} that is attributed to remaining loose B_4 units, that is, tetrahedral boron not participating in any intermediate range order units but linking other network segments together.

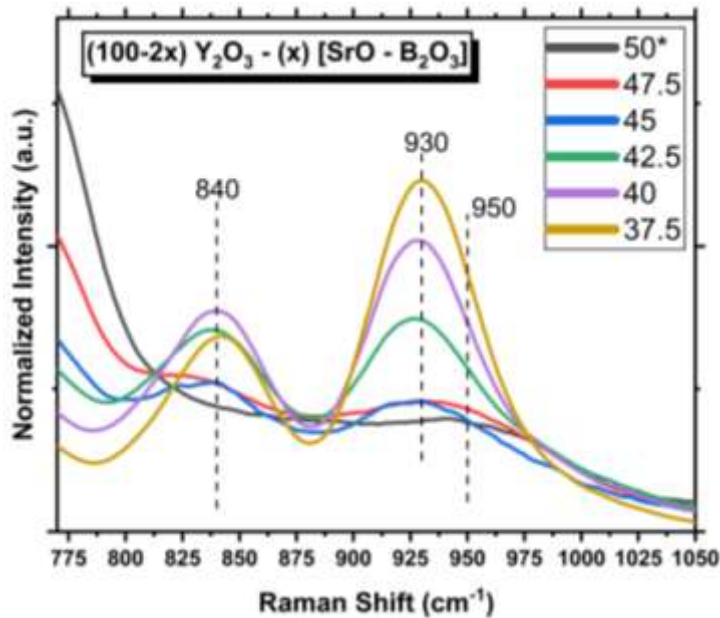


Figure 4-3. Raman spectra of Strontium Yttrium Borate glasses over the interval $770 - 1050\text{ cm}^{-1}$.

Figure 4-3 highlights the progression of borate species disconnected from any percolating network. In going from 50^* to 47.5 , a feature appears at 840 cm^{-1} belonging to

the symmetric B-O-B stretch of pyroborate dimers, $[\text{B}_2\text{O}_5]^{4-}$. At the same time, the symmetric stretch of BO_3^{3-} units brings about a decrease in the frequency of the diborate related feature at 950 cm^{-1} . These features become distinct and increase in relative intensity (Figure 4-1 and 4-3) as the yttria content increases. The 840 cm^{-1} band reaches a maximum intensity at $x=40$ while the 930 cm^{-1} expectedly reaches its maximum at $x=37.5$. The remaining pyroborate units and loose B_4 (Figure 4-2) at $x=37.5$ indicate the glasses are under-modified with respect to their nominal composition, possibly because of incomplete melting of the Y_2O_3 at the temperatures used. Nonetheless, the growth of the features associated with molecular borate entities in Figure 4-3 paralleling the destruction of metaborate chains and borate groups (Figure 4-2) clearly shows that the addition of yttrium oxide to the strontium borate system abolishes the dimensionality of the borate network resulting in disconnected species crosslinked by Sr^{2+} and Y^{3+} cations.

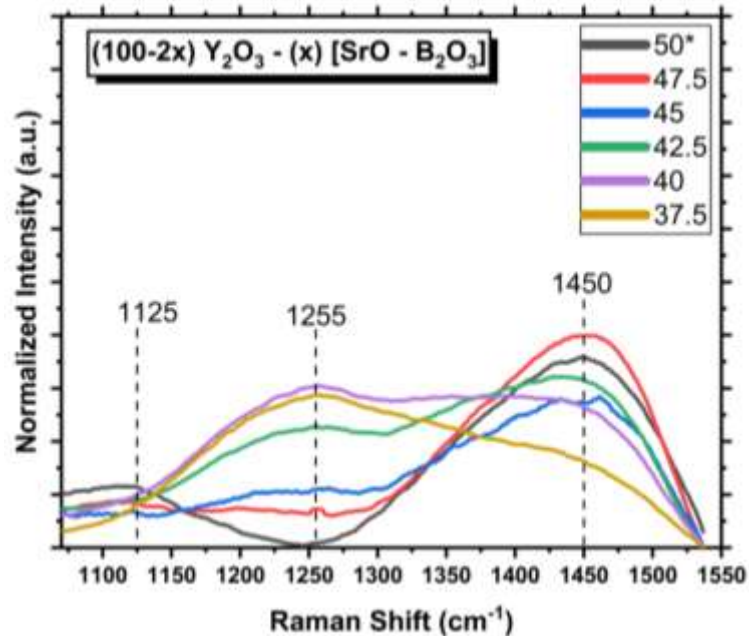


Figure 4-4. Raman spectra of Strontium Yttrium Borate glasses over the interval $1075 - 1550\text{ cm}^{-1}$.

As previously mentioned, the feature at 1125 cm^{-1} in Figure 4-4 is characteristic of diborate units and loses relative intensity with increasing yttria content. The high frequency envelope ($1150 - 1550\text{ cm}^{-1}$) arises from the asymmetric stretch of $\text{B}_3 - \text{O}$ bonds. This

spectral region of the x=50* glass consists of an envelope spanning 1250 – 1525 cm⁻¹ with a maximum at 1450 cm⁻¹ that is characteristic of trigonal metaborate units in chain arrangements. The band at 1450 cm⁻¹ attains a maximum relative intensity at 5 mol% yttria where the oxygen to boron ratio is above the metaborate stoichiometry. This, together with the subtle appearance of BO₃³⁻ units at the same composition can be explained by a disproportionation reaction:



The feature at 1255 cm⁻¹ is known to belong to the asymmetric B₃ – O stretch of trigonal pyroborate units and the activity in the high frequency region trends with activity of the 840 cm⁻¹ band in Figure 4-3.

4.2.2 Borate Network – Infrared Spectroscopy

Attention is now turned to the Infrared spectra of the same SYB glasses, overlaid in Figure 4-5. As discussed in the Background, the Infrared spectra of borate glasses can usually be broken down into 3 regions. Bending modes of B₃ appear between 600-800 cm⁻¹, B₄ modes appear between 800-1150 cm⁻¹ and B₃ asymmetric stretching occurs between 1150 – 1600 cm⁻¹ [58, 59, 68].

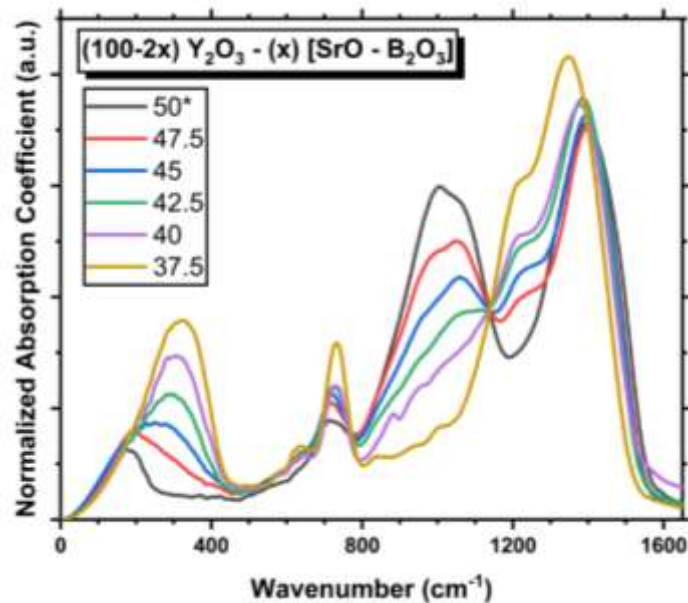


Figure 4-5. Overlapped Infrared absorption coefficient spectra of Strontium Yttrium Borate glasses.

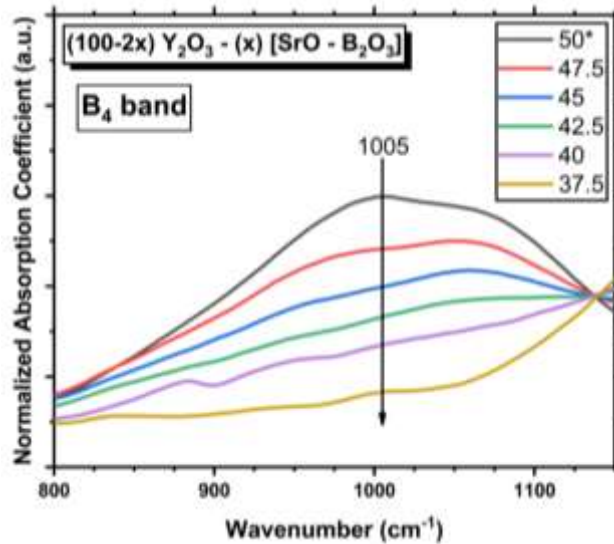


Figure 4-6. Tetrahedral boron IR band in Strontium Yttrium Borates.

Figure 4-6 highlights the continuous destruction of tetrahedral boron, $[\text{B}\text{O}_4]^-$, with increasing yttria content. In binary borate glasses, quantification of the fraction of tetrahedral boron can be made by comparing the area of the region $800\text{--}1150\text{ cm}^{-1}$ (A_4) to the trigonal boron band between $1150\text{--}1550\text{ cm}^{-1}$ (A_3) (Figure 4-7) [65]. Precise quantification requires NMR data for scaling, though an approximate trend may be made with the Infrared spectra alone. Figure 4-8 plots the A_4 values against yttria content and the trend that is observable in Figure 4-6 is seen, that is, a decrease in B_4 with increasing modification. Though the limits of integration for A_4 and A_3 provide excellent agreement with NMR data for stoichiometries up to metaborate, their applicability to borate glasses containing a high fraction of BO_3^{3-} units is questionable. This is because the band attributable to the asymmetric stretch of the trigonal orthoborate anion in glasses extends down to 1100 cm^{-1} (Figure 3-9, 3-17, 3-19). Logically, this would imply that the aforementioned limits of integration would yield an overestimation of tetrahedral boron in glasses containing significant quantities of trigonal orthoborate entities. Moreover, the terminal stretch of $\text{B}_4\text{--O}$ in $\text{B}_3\text{O}_9^{9-}$ rings extends up to 1200 cm^{-1} in both YBO_3 and GdBO_3 (Figure 3-3) pointing to the potential for overlap at the intersection of trigonal and tetrahedral orthoborate units.

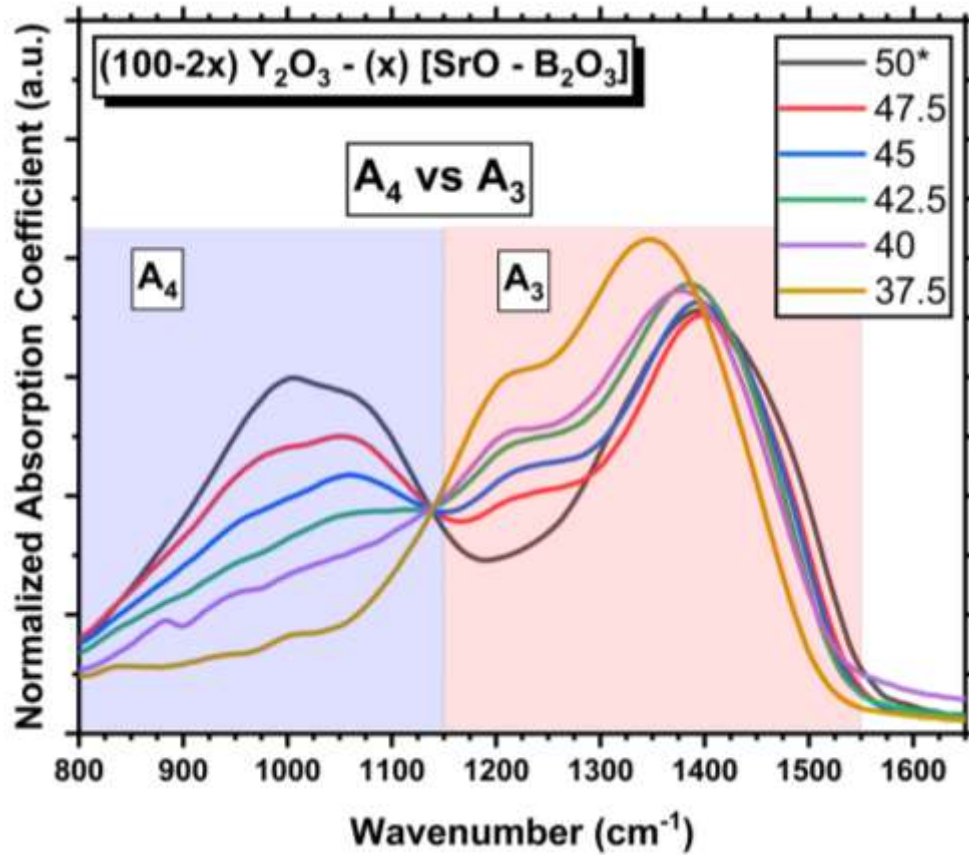


Figure 4-7. A_4 vs A_3 in Infrared spectra of Strontium Yttrium Borate Glasses shown over 800-1650 cm^{-1} .

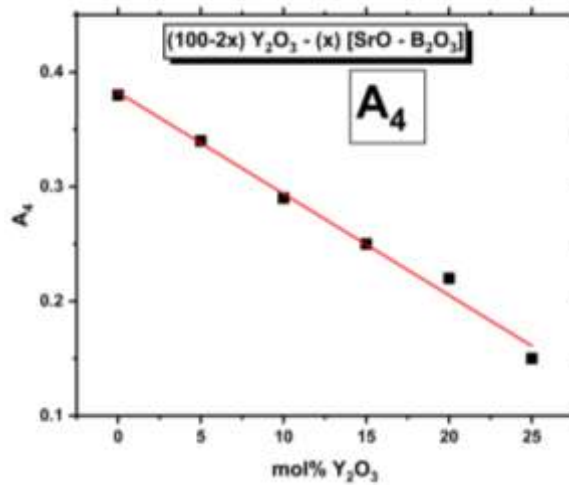


Figure 4-8. Plot of A_4 vs Y_2O_3 content of Strontium Yttrium Borate Glasses. Line is drawn as a guide for the eye.

4.2.3 Metal Cations – Vibrational Spectroscopy

The far infrared band, well separated from the borate network bands, contains information of the metal cation environments. Figure 4-9 displays the overlaid IR absorption coefficient spectra from 0-600 cm^{-1} . For $x=50^*$, the Sr^{2+} band is seen at 180 cm^{-1} . The cation motion band shifts to higher frequencies with increasing Y_2O_3 content (Figure 4-10). In the glass with 25 mol% Y_2O_3 the cation motion band reaches a maximum at 323 cm^{-1} . It is observed that the shift to higher frequencies agree very well with the low frequency band in the Raman spectra where the Y – O stretching band around 305 cm^{-1} becomes prominent as Y_2O_3 content increases (Figure 4-11).

Higher M-O vibrational frequencies are associated with lower cation mass and higher force constants which are proportional to the strength of the bond [72]. Considering that Sr and Y have similar atomic masses (87.62 vs 88.91), the low frequency regions of the vibrational spectra tell that the Y^{3+} – O bond is stronger than the Sr^{2+} – O bond due to their difference in cation charge. Addition of Y_2O_3 results in strong Y-O-B bonds and so, despite the breakdown of a continuous borate network, the strong cross-linking ability of Y^{3+} results in the T_g increase at high Y_2O_3 content.

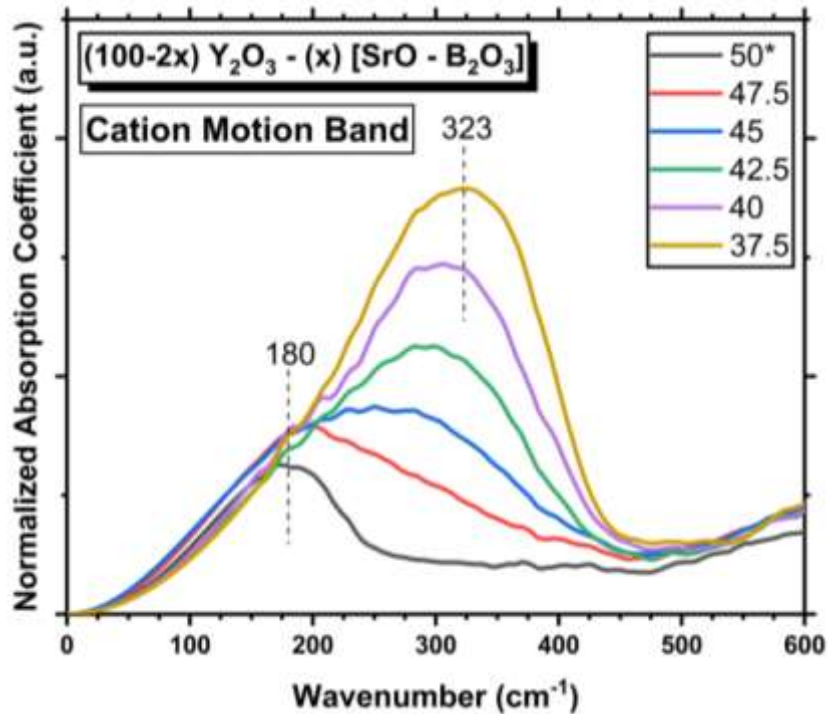


Figure 4-9. Cation motion bands in Strontium Yttrium Borate glasses.

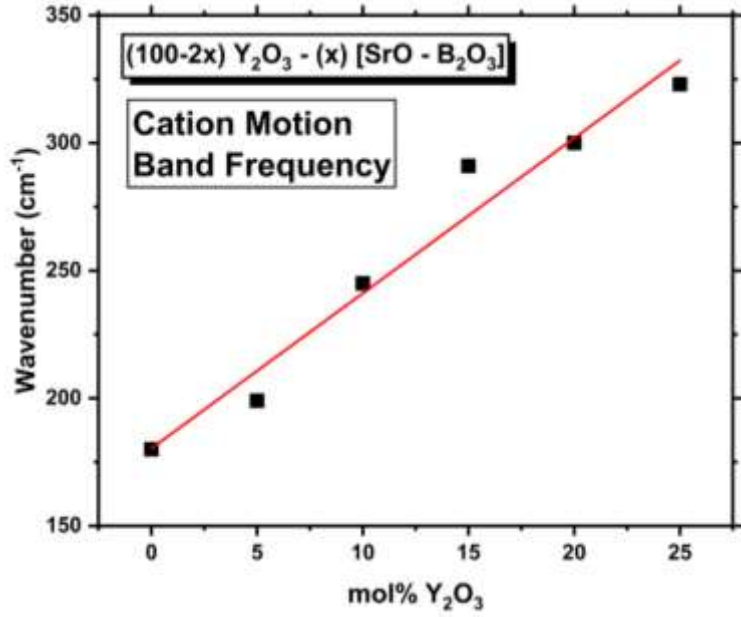


Figure 4-10. Plot of apparent (combined Sr²⁺/Y³⁺) cation motion band maximum vs Y₂O₃ content. Line is drawn as a guide for the eye.

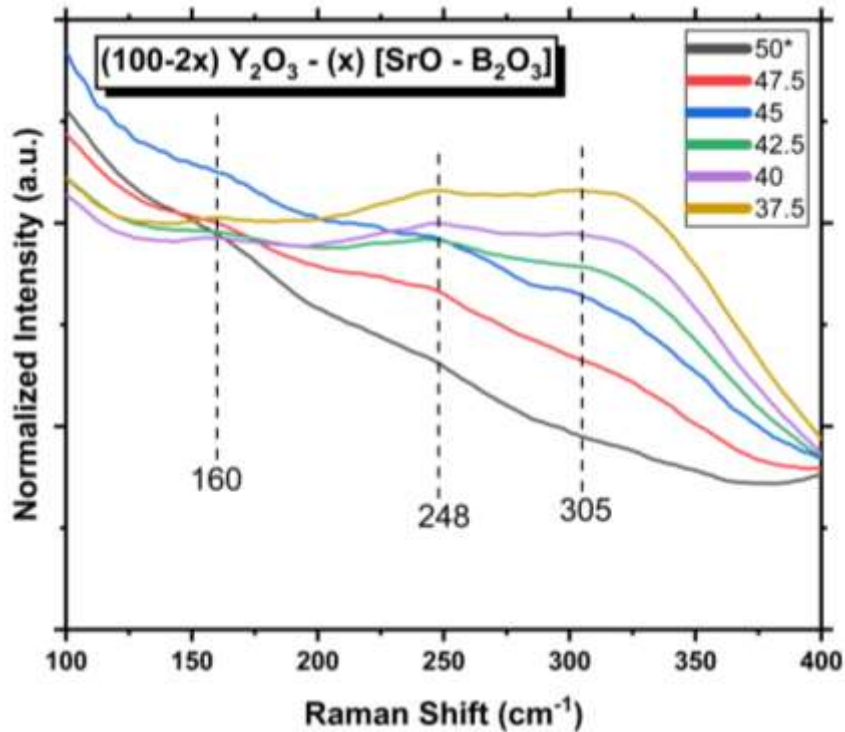


Figure 4-11. Low frequency range (100-400 cm⁻¹) of the Raman spectra for Strontium Yttrium Borate glasses.

4.3 Overmodified Strontium Yttrium Borates

The om-SYB glass spectra in Section 3.3.3 can be readily explained in terms of BO_3^{3-} units. In Figure 3-16, the Raman spectra display a well-defined low frequency band with local maxima at 241 and 321 cm^{-1} due to M – O stretching. The in-plane bending feature at 589 and 629 cm^{-1} may, as discussed before result from either the mixture of Sr^{2+} and Y^{3+} crosslinking the O-B-O segments to different degrees or from non-planar BO_3^{3-} units. The in-plane bending is obscured in the IR spectra in Figure 3-17, perhaps due to poor measurement signal from the small, unpolished, splat quenched glass. The out-of-plane bending is seen at 748 cm^{-1} and 744 cm^{-1} in the Raman and Infrared, respectively. The symmetric stretch of the BO_3^{3-} anion dominates the Raman spectra at 926 cm^{-1} and the same mode's very weak IR activity can be seen at roughly the same frequency. In both the Raman and IR, the asymmetric stretch of the BO_3^{3-} units results in the envelope spanning 1100-1450 cm^{-1} . No modification beyond the orthoborate stoichiometry is observed.

4.4 Orthoborate $\text{Li}_2\text{O} - \text{R}_2\text{O}_3 - \text{B}_2\text{O}_3$

The Raman and Infrared spectra in Figure 3-18 and 3-19 show the relative insensitivity of the BO_3^{3-} bands to different R^{3+} elements. The indicated lines are intended to draw attention to the general positions where characteristic vibrations are observed. In the Raman spectra of Figure 3-18, the $\text{R}^{3+} - \text{O}$ stretching is seen around $\sim 300\text{-}315 \text{ cm}^{-1}$ for all glass samples. The in-plane (ν_4) and out-of-plane (ν_2) bending modes are seen at around $\sim 645 \text{ cm}^{-1}$ and $\sim 768 \text{ cm}^{-1}$, respectively. The symmetric stretch (ν_1) mode has a characteristic sharp band at $\sim 940 \text{ cm}^{-1}$. The asymmetric stretch (ν_3) mode has broad band of moderate relative intensity over the interval 1100 – 1450 cm^{-1} with a soft maximum between 1200 – 1225 cm^{-1} .

In the Infrared spectra, the same vibrations are seen at similar frequencies. The R^{3+} motion bands contribute between 200-400 cm^{-1} while the Li^+ motion band is seen at $\sim 500 \text{ cm}^{-1}$ in all glasses. The in-plane bending is enveloped by the FIR band but gives a distinct shoulder feature around $\sim 630 \text{ cm}^{-1}$. The out-of-plane bending has a maximum at $\sim 742 \text{ cm}^{-1}$. Due to the reduced symmetry of the BO_3^{3-} species in the vitreous state, the BO_3^{3-} symmetric stretch mode (ν_1) acquires weak IR activity as can be seen at $\sim 935 \text{ cm}^{-1}$. The asymmetric B – O stretch is the most prominent feature of the IR spectra and covers a range

between 1100 – 1450 cm^{-1} . The band appears to consist of two components, one around 1210 – 1230 cm^{-1} and one around 1300 – 1330 cm^{-1} .

The isostructural nature of the $\text{Li}_2\text{O} - \text{R}_2\text{O}_3 - \text{B}_2\text{O}_3$ glass studied is not only seen in the vibrational spectra but is supported by the evidence obtained by the measured lifetime fluorescence of Tb^{3+} probe ions. As seen in the study of the reference materials (Section 3.1) of YBO_3 , GdBO_3 , and LaBO_3 the structures of the crystalline compounds differ fundamentally. The glass forming ability of the different R^{3+} cations is apparent in the crystallization of the La^{3+} containing lithium borate compared to the glasses obtained with Y^{3+} and Gd^{3+} . Despite this, the prepared samples all displayed nearly equivalent fluorescent lifetimes for the Tb^{3+} 543 nm emission.

The measured lifetime of Tb^{3+} in the $\text{Li}_2\text{O} - \text{R}_2\text{O}_3 - \text{B}_2\text{O}_3$ orthoborate glasses is approximately the same as the lifetime of Tb^{3+} recorded in binary zinc borates (~2.3 ms) by Hermann *et al.*[125]. The binary zinc borate has a window of glass formation ranging from 50 – 67 mol% ZnO. All glasses in this range contain highly charged trigonal pyro- and orthoborate units due to the high disproportionation of metaborate species induced by Zn^{2+} discussed in detail by Möncke [60, 72]. In Herrmann's investigation, it was observed that the lifetime of Tb^{3+} in zinc borates did not change for 0.1 – 10 wt% doping of Tb_2O_3 . Considering the presence of highly charged units across the entire zinc borate glass forming range, it may reasonably be assumed that similar structural entities are present in ZnB:Tb for all Tb dopant concentrations that permit homogenous glass formation. Bringing together Hermann's results and those presented here, it appears that the fluorescent lifetime of Tb^{3+} in highly modified borate glasses that offer non-bridging oxygen ligands belonging to trigonal pyro- or orthoborate units is between ~2.2-2.3 ms.

5. Conclusion

It is concluded that tetrahedral boron with non-bridging oxygen ions do not form in the SrYB ternary for the glass-forming range achieved here and under the ambient pressure conditions the melts were heated and cooled under, unlike the SrMnB and SrEuB systems prepared in a reducing atmosphere and with larger values of the O/B ratio. In the SrYB system, it was observed that despite the depolymerization of the network into highly charged isolated borate species, the melting temperature and glass transition temperature correlated. This suggests that the crosslinking strength of trivalent Y^{3+} is high, in agreement with its theoretical role as an intermediate cation in the framework of Dietzel's concept of field strength.

The formation of the $B_3O_9^{9-}$ ring structure in the LiYB system and its absence in the SrYB system is believed to be intimately related to the glass transition temperature with respect to the phase transformation temperature of the yttrium-orthoborate crystalline compound. For the $x=18$ sample discussed in section 3.2.1 the T_g was measured by DSC to be 465 °C. This is well below the reported [116] phase transformation temperature of YBO_3 for the HT \rightarrow LT transition of 596.5 °C, that is the $3 [BO_3^{3-}] \rightarrow B_3O_9^{9-}$ transition. The SrYB system shows the formation of only trigonal orthoborate units and the T_g values were all greater than 630 °C.

The study of LRB glasses indicates that lithium borates containing 20 mol% of Group 3 or Lanthanide series elements, at the orthoborate stoichiometry, consist of trigonal orthoborate units. This was observed in the vibrational spectra and supported by time-dependent fluorescence measurements. It is interesting to observe that the R^{3+} cations that do have polymorphic RBO_3 crystalline compounds (i.e. Y, Gd, Eu) formed glasses though only one type of borate structure could be observed. Similar to how pure B_2O_3 consists of only neutral trigonal borate units linked together, the LRB glasses studied here consist of only charged trigonal borate units linked together by the cross-linking metal cations.

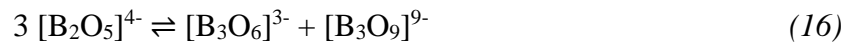
It is concluded that tetrahedral orthoborate rings might be formed in the vitreous state for yttrium containing glasses where the glass transition temperature is below the threshold of the phase transformation temperature; however, no current evidence suggests

that this happens in *bulk* quantities for *melt quenched glasses*. For yttrium containing glasses, if the fictive temperature is above the HT \rightarrow LT phase transformation temperature, the yttrium ions will only be coordinated with trigonal borate species as in the HT crystal phase.

6. Outlook

LYB glasses with relatively high yttria content may function as host materials for doping with fluorescent ions. An examination of whether the REBO₃ (RE=rare earth element) crystallite size can be controlled by thermal treatment and the impact this has on optical and mechanical properties may be worthwhile.

Non-ambient pressure experiments indicate the formation of dense borate units and tetrahedral boron structures is favored at high pressure [126]. Given the observation of the B₃O₉⁹⁻ crystallites in the low T_g LYB glasses, it is hypothesized that if yttria containing alkali borate glasses with an oxygen to boron ratio higher than metaborate (O:B = 2) are subject to high pressure conditions, a mixture of metaborate and orthoborate ring types may result from the disproportionation of pyroborate units by the expression



This hypothesis requires the assumption that no other exotic species are formed such as edge or face sharing borate polyhedra or oxygen with coordination number greater than 2 as seen in molecular dynamics simulation [127].

During the study of 45 Li₂O – 20 R₂O₃ – 35 B₂O₃ glasses, a glass was made with R = Bi³⁺. The vibrational spectra for this glass differ greatly to the glasses where R is a Group 3 or Lanthanide series element. Bismuth borate crystals are known to contain tetrahedral boron with non-bridging oxygen ions. On the other hand, BiO_n pseudo-phases have also been observed to occur in bismuth borate glasses giving an under modified borate network. Given the preliminary spectral data and considering the multiple potential explanations, a systematic investigation such as that carried out here but using diamagnetic Bi₂O₃ seems promising.

While the studies performed herein do not provide evidence for B₄ with nbOs occurring in the vitreous state, several potential candidate systems have been ruled out. Further, the vibrational spectra acquired through the course of this investigation should provide good reference material for identifying a modification route that does not consist solely of the formation of highly charged trigonal borate units.

7. REFERENCES

1. Zachariasen, W.H., *The Atomic Arrangement in Glass*. Journal of the American Chemical Society, 1932. **54**(10): p. 3841-3851.
2. Warren, B.E., *X-Ray Determination of the Structure of Glass*. Journal of the American Ceramic Society, 1934. **75**: p. 5-10.
3. Krogh-Moe, J., *The Structure of Vitreous and Liquid Boron Oxide*. Journal of Non-Crystalline Solids, 1969. **1**: p. 269-284.
4. Wright, A.C., *Borate Structures: Crystalline and Vitreous*. Physics and Chemistry of Glasses: European Journal of Glass Science and Technology Part B, 2010. **51**(1): p. 1-39.
5. Goubeau, J. and H. Keller, *RAMAN- Spektren und Struktur von Boroxol-Verbindungen*. Z. anorg. allg. Chem, 1953. **272**: p. 303-312.
6. Bray, P.J., *Structural Models for Borate Glasses*. Journal of Non-Crystalline Solids, 1985. **75**: p. 29-36.
7. Bray, P.J., et al., *B¹⁰ NMR Studies of the Structure of Borate Glasses*. Journal of Non-Crystalline Solids, 1980. **38-39**: p. 93-98.
8. Feller, S.A., W.J. Dell, and P.J. Bray, *¹⁰B NMR Studies of Lithium Borate Glasses*. Journal of Non-Crystalline Solids, 1982. **51**: p. 21-30.
9. Jellison, G.E., Jr. and P.J. Bray, *A Structural Interpretation of B¹⁰ and B¹¹ NMR Spectra in Sodium Borate Glasses*. Journal of Non-Crystalline Solids, 1978. **29**: p. 187-206.
10. Jellison, G.E., Jr., et al., *Determinations of Structure and Bonding in Vitreous B₂O₃ by Means of B¹⁰, B¹¹, and O¹⁷ NMR*. The Journal of Chemical Physics, 1977. **66**(2): p. 802-812.
11. Yun, Y.H. and P.J. Bray, *B¹¹ Nuclear Magnetic Resonance Studies of Li₂O-B₂O₃ Glasses of High Li₂O Content*. Journal of Non-Crystalline Solids, 1981. **44**: p. 227-237.
12. Windisch, C.F. and W.M. Risen, *Vibrational Spectra of Oxygen- and Boron-Isotopically Substituted B₂O₃ Glasses*. Journal of Non-Crystalline Solids, 1982. **48**(2): p. 307-323.
13. Hannon, A.C., et al., *Boroxol Groups in Vitreous Boron Oxide: New Evidence from Neutron Diffraction and Inelastic Neutron Scattering Studies*. Journal of Non-Crystalline Solids, 1994. **177**: p. 299-316.

14. Hannon, A.C., et al., *Phonon Spectra of Vitreous B₂O₃*. Journal of Non-Crystalline Solids, 1988. **106**: p. 116-119.
15. Huppertz, H. and D.A. Keszler, *Borates: Solid-State Chemistry*, in *Encyclopedia of Inorganic and Bioinorganic Chemistry*. 2014. p. 1-12.
16. Wright, A.C., *My Borate Life: An Enigmatic Journey*. International Journal of Applied Glass Science, 2015. **6**(1): p. 45-63.
17. Neuville, D.R., D. De Ligny, and G.S. Henderson, *Advances in Raman Spectroscopy Applied to Earth and Material Sciences*. Reviews in Mineralogy and Geochemistry, 2014. **78**(1): p. 509-541.
18. Krogh-Moe, J. and M. Ihara, *The Crystal Structure of Caesium Enneaborate, Cs₂O·9 B₂O₃*. Acta Crystallographica, 1967. **23**: p. 427-430.
19. Ferlat, G., et al., *Hidden Polymorphs Drive Vitrification in B₂O₃*. Nat Mater, 2012. **11**(11): p. 925-9.
20. Ehrt, D., *The Effect of ZnO, La₂O₃, PbO, and Bi₂O₃ on the Properties of Binary Borate Glasses and Melts*. Physics and Chemistry of Glasses: European Journal of Glass Science and Technology Part B, 2006. **47**(6): p. 669-674.
21. Shibata, M., et al., *The Density of Lithium Borate Glasses Related to Atomic Arrangements*. Journal of Non-Crystalline Solids, 1986. **85**(1-2): p. 29-41.
22. Donohoe, L.M. and J.E. Shelby, *Formation and Properties of Soda-Lime Borate Glasses*. Physics and Chemistry of Glasses: European Journal of Glass Science and Technology Part B, 2005. **47**(1): p. 16-21.
23. Jaccani, S.P. and L. Huang, *Understanding Sodium Borate Glasses and Melts from Their Elastic Response to Temperature*. International Journal of Applied Glass Science, 2016. **7**: p. 452-463.
24. Yoshida, S., et al., *Indentation Induced Densification of Sodium Borate Glasses*. European Journal of Glass Science and Technology Part B Physics and Chemistry of Glasses, 2009. **50**(1): p. 63-70.
25. Ehrt, D., *Zinc and Manganese Borate Glasses - Phase Separation, Crystallisation, Photoluminescence, and Structure*. European Journal of Glass Science and Technology Part B Physics and Chemistry of Glasses, 2013. **54**(2): p. 65-75.
26. Brauer, D.S. and D. Möncke, *Structure of Bioactive Silicate, Phosphate and Borate glasses*, in *Bioactive Glasses: Fundamentals, Technology and Applications*, A.R. Boccaccini, D.S. Brauer, and L. Hupa, Editors. 2016, Royal Society of Chemistry p. 61-88.
27. Liu, X., et al., *In Vitro Degradation and Conversion of Melt-Derived Microfibrous Borate (13-93B3) Bioactive Glass Doped with Metal Ions*. Journal of the American Ceramic Society, 2014. **97**(11): p. 3501-3509.
28. Yao, A., et al., *In Vitro Bioactive Characteristics of Borate-Based Glasses with Controllable Degradation Behavior*. Journal of the American Ceramic Society, 2007. **90**(1): p. 303-306.
29. Galeener, F.L. and A. Geissberger, *Raman Studies of B₂O₃ Glass Structure: 10B->11B Isotopic Substitution*. Journal de Physique Colloques, 1982. **43**(C9): p. 343-346.
30. Bengisu, M., *Borate Glasses for Scientific and Industrial Applications: A Review*. Journal of Materials Science, 2015. **51**(5): p. 2199-2242.

31. Zhao, S., et al., *Wound Dressings Composed of Copper-Doped Borate Bioactive Glass Microfibers Stimulate Angiogenesis and Heal Full-Thickness Skin Defects in a Rodent Model*. *Biomaterials*, 2015. **53**: p. 379-91.
32. Kamitsos, E.I., *Infrared Studies of Borate Glasses*. *Physics and Chemistry of Glasses*, 2003. **44**(2): p. 79-87.
33. Bray, P.J., et al., *NMR Studies of Fluoride and Fast Ion Conducting Glasses*. *Journal of Non-Crystalline Solids*, 1983. **56**: p. 27-32.
34. Kim, K.S. and P.J. Bray, *B^{11} NMR Studies of Glasses in the System $MgO-Na_2O-B_2O_3$* . *Physics and Chemistry of Glasses*, 1974. **15**(2): p. 47-51.
35. Deters, H., et al., *Structural Characterization of Rare-Earth Doped Yttrium Aluminoborate Laser Glasses Using Solid State NMR*. *Journal of Physical Chemistry*, 2009. **113**: p. 16216-16225.
36. Deters, H., et al., *Structural Models for Yttrium Aluminum Borate Laser Glasses: NMR and EPR Studies of the System $(Y_2O_3)_{0.2} - (Al_2O_3)_x - (B_2O_3)_{0.8-x}$* . *Phys Chem Chem Phys*, 2011. **13**: p. 16071-16083.
37. Eckert, H., *Structural Characterization of Noncrystalline Solids and Glasses Using Solid State NMR*. *Progress in Nuclear Magnetic Resonance Spectroscopy*, 1992. **24**(3): p. 159-293.
38. Kroeker, S., et al., *Alkali Dependence of Tetrahedral Boron in Alkali Borate Glasses*. *Physics and Chemistry of Glasses: European Journal of Glass Science and Technology Part B*, 2006. **47**(4): p. 393-396.
39. Möncke, D., et al., *Connectivity of Borate and Silicate Groups in a Low-Alkali Borosilicate Glass by Vibrational and 2D NMR Spectroscopy*. *Journal of Chemical Technology and Metallurgy*, 2015. **50** (4): p. 381-386.
40. Svenson, M.N., et al., *Volume and Structural Relaxation in Compressed Sodium Borate Glass*. *Phys Chem Chem Phys*, 2016. **18**(43): p. 29879-29891.
41. Goetschius, K.L., et al., *Dissolution Behavior of Ternary Alkali-Alkaline Earth-Borate Glasses in Water*. *Journal of Non-Crystalline Solids*, 2018. **487**: p. 12-18.
42. Bischof, J. and B.E. Warren, *X-Ray Diffraction Study of Soda-Boric Oxide Glass*. *Journal of the American Ceramic Society*, 1938. **21**: p. 287-293.
43. Karki, A., et al., *The Density of Sodium-Borate Glasses Related to Atomic Arrangements*. *Journal of Non-Crystalline Solids*, 1987. **92**(1): p. 11-19.
44. Velez, M.H., H.L. Tuller, and D.R. Uhlmann, *Chemical Durability of Lithium Borate Glasses*. *Journal of Non-Crystalline Solids*, 1982. **49**(1-3): p. 351-362.
45. Lower, N.P., et al., *Physical Properties of Alkaline-Earth and Alkali Borate Glasses Prepared Over and Extended Range of Compositions*. *Journal of Non-Crystalline Solids*, 2001. **293-295**: p. 559-675.
46. Kamitsos, E.I., G.D. Chryssikos, and M.A. Karakassides, *Glass Transition Phenomena and Cation Vibrations in Alkali Borate Glasses*. *Physics and Chemistry of Glasses*, 1988. **29**(3): p. 121-126.
47. Vogel, W., *Glass Chemistry*. 2nd ed. 1992: Springer-Verlag.
48. Shartsis, L., W. Capps, and S. Spinner, *Viscosity and Electrical Resistivity of Molten Alkali Borates*. *Journal of the American Ceramic Society*, 1953. **36**(10): p. 319-326.

49. Jellison, G.E., Jr., et al., *Determinations of Structure and Bonding in Vitreous B₂O₃ by Means of B₁₀, B₁₁, and O₁₇ NMR*. The Journal of Chemical Physics, 1977. **66**: p. 802-812.
50. Mauro, J.C., P.K. Gupta, and R.J. Loucks, *Composition Dependence of Glass Transition Temperature and Fragility. II. A Topological Model of Alkali Borate Liquids* The Journal of Chemical Physics, 2009. **130**: p. 234503.
51. Vedishcheva, N.M., I.G. Polyakova, and A.C. Wright, *Short and Intermediate Range Order in Sodium Borosilicate Glasses: A Quantitative Thermodynamic Approach*. European Journal of Glass Science and Technology Part B Physics and Chemistry of Glasses, 2014. **55**(6): p. 225-236.
52. Bodker, M.S., et al., *Statistical Mechanical Modeling of Borate Glass Structure and Topology: Prediction of Superstructural Units and Glass Transition Temperature*. J Phys Chem B, 2019. **123**(5): p. 1206-1213.
53. Takeda, W., et al., *Topological Constraint Model of High Lithium Content Borate Glasses*. Journal of Non-Crystalline Solids: X, 2019. **3**.
54. Ehrt, D., H. Reiß, and W. Vogel, *Mikrostrukturuntersuchungen an CoO-haltigen Na₂O-B₂O₃-SiO₂-Gläsern*. Silikattechnik, 1977. **28**(12): p. 359-364.
55. Affatigato, M., et al., *The Glass Transition Temperature of Lithium and Lithium-Sodium Borate Glasses Over Wide Ranges of Composition*. Phys. Chem. Glasses, 1990. **31**: p. 19-24.
56. Chryssikos, G.D. and E.I. Kamitsos, *Borate Structures by Vibrational Spectroscopy*, in *Borate Glasses, Crystals, and Melts*, A.C. Wright, S.A. Feller, and A.C. Hannon, Editors., Soc. Glass Technology. p. 128-139.
57. Kamitsos, E.I., M.A. Karakassides, and G.D. Chryssikos, *Vibrational Spectra of Magnesium-Sodium-Borate Glasses. 2. Raman and Mid-Infrared Investigation of the Network Structure*. Journal of Physical Chemistry, 1987. **91**: p. 1073-1079.
58. Kamitsos, E.I., A.P. Patsis, and G.D. Chryssikos, *Infrared Reflectance Investigation of Alkali Diborate Glasses*. Journal of Non-Crystalline Solids, 1993. **152**: p. 246-257.
59. Kamitsos, E.I. and G.D. Chryssikos, *Borate Glass Structure by Raman and Infrared Spectroscopies*. Journal of Molecular Structure, 1991. **247**: p. 1-16.
60. Möncke, D., et al., *Transition and Post-Transition Metal Ions in Borate Glasses: Borate Ligand Speciation, Cluster Formation, and Their Effect on Glass Transition and Mechanical Properties*. J Chem Phys, 2016. **145**(12): p. 124501.
61. Othman, H., et al., *Spectroscopic Study of the Role of Alkaline Earth Oxides in Mixed Borate Glasses - Site Basicity, Polarizability and Glass Structure*. Journal of Non-Crystalline Solids, 2020. **533**.
62. Kamitsos, E.I., M.A. Karakassides, and G.D. Chryssikos, *Cation-Network Interactions in Binary Alkali Metal Borate Glasses. A Far-Infrared Study*. Journal of Physical Chemistry, 1987. **91**: p. 5807-5813.
63. Kamitsos, E.I., C.P. Varsamis, and A. Vegiri, *Spectroscopic Studies of Mobile Cations in Glass*, in *Proceedings of the 19th International Congress on Glass, Invited Papers, Edinburgh, Scotland, Society of Glass Technology, Sheffield, UK, 2001, vol.1, pp. 234-246*.
64. Kamitsos, E.I., et al., *Structure-Property Correlation in Glasses by Infrared Reflectance Spectroscopy*. Journal of Non-Crystalline Solids, 1997. **222**: p. 59-68.

65. Yiannopoulos, Y.D., G.D. Chryssikos, and E.I. Kamitsos, *Structure and Properties of Alkaline Earth Borate Glasses*. Phys. Chem. Glasses, 2001. **42**(3): p. 164-172.
66. Vegiri, A., C.P. Varsamis, and E.I. Kamitsos, *Molecular Dynamics Investigation of Mixed-Alkali Borate Glasses: Short-Range Order Structure and Alkali-Ion Environments*. Physical Review B, 2009. **80**(18): p. 184202.
67. Möncke, D., et al., *On the Connectivity of Borate Tetrahedra in Borate and Borosilicate Glasses*. European Journal of Glass Science and Technology Part B Physics and Chemistry of Glasses, 2015. **56**(5): p. 203-211.
68. Kamitsos, E.I., et al., *Infrared Reflectance Spectra of Lithium Borate Glasses*. Journal of Non-Crystalline Solids, 1990. **126**(1-2): p. 52-67.
69. Kamitsos, E.I., *Modifying Role of Alkali-Metal Cations in Borate Glass Networks*. The Journal of Physical Chemistry, 1989. **93**(4): p. 1604-1611.
70. Kurudirek, M., *Heavy Metal Borate Glasses: Potential Use for Radiation Shielding*. Journal of Alloys and Compounds, 2017. **727**: p. 1227-1236.
71. Singh, N., et al., *Comparative Study of Lead Borate and Bismuth Lead Borate Glass Systems as Gamma-Radiation Shielding Materials*. Nuclear Instruments and Methods in Physics Research Section B: Beam Interactions with Materials and Atoms, 2004. **225**(3): p. 305-309.
72. Möncke, D., et al., *Transition and Post-Transition Metal Ions in Borate Glasses: Borate Ligand Speciation, Cluster Formation, and Their Effect on Glass Transition and Mechanical Properties*. The Journal of Chemical Physics, 2016. **145**(12): p. 124501.
73. Krogh-Moe, J. and P.S. Wold-Hansen, *The Crystal Structure of Hexalead Pentaborate, 6 PbO .5B₂O₃*. Acta Crystallographica, 1973. **B29**: p. 2242-2246.
74. Yao, Z.Y., et al., *Structure and Mechanical Properties of Copper-Lead and Copper-Zinc Borate Glasses*. Journal of Non-Crystalline Solids, 2016. **435**: p. 55-68.
75. Chakraborty, I.N., J.E. Shelby, and S.R.A. Condrate, *Properties and Structure of Lanthanum Borate Glasses*. Journal of the American Ceramic Society, 1984. **67**(12): p. 782-785.
76. Chakraborty, I.N. and D.E. Day, *Effect of R³⁺ Ions on the Structure and Properties of Lanthanum Borate Glasses*. Journal of the American Ceramic Society, 1985. **68**(12): p. 641-645.
77. Terashima, K., et al., *Structure and Nonlinear Optical Properties of Lanthanide Borate Glasses*. Journal of the American Ceramic Society, 1997. **80**(11): p. 2903-2909.
78. Chakraborty, I.N., et al., *Structure-Property Relations in Lanthanide Borate Glasses*. Journal of the American Ceramic Society, 1985. **68**(7): p. 368-371.
79. Shelby, J.E., *Rare Earths as Major Components in Oxide Glasses*. Key Engineering Materials, 1994. **94-95**: p. 1-42.
80. Shafer, M.W. and J.C. Suits, *Preparation and Faraday Rotation of Divalent Europium Glasses*. Journal of the American Ceramic Society, 1966. **49**(5): p. 261-264.
81. Chakraborty, I.N., H.L. Rutz, and D.E. Day, *Glass Formation, Properties, and Structure of Y₂O₃ - Al₂O₃ - B₂O₃ Glasses*. Journal of Non-Crystalline Solids, 1986. **84**: p. 86-92.

82. Tagiara, N.S., et al., *Synthesis, Thermal, and Structural Properties of Pure TeO₂ Glass and Zinc-Tellurite Glasses*. Journal of Non-Crystalline Solids, 2017. **457**: p. 116-125.
83. Tagiara, N.S., et al., *Short-Range Structure, Thermal, and Elastic Properties of Binary and Ternary Tellurite Glasses*. The Journal of Physical Chemistry B, 2019. **123**: p. 7905-7918.
84. Konidakis, I., C.P. Varsamis, and E.I. Kamitsos, *Effect of Synthesis Method on the Structure and Properties of AgPO₃ - Based Glasses*. Journal of Non-Crystalline Solids, 2011. **357**(14): p. 2684-2689.
85. Adamiv, V.T., et al., *Optical Properties of Alkali and Alkaline Earth Tetraborate Glasses Prepared in the Alumina Crucible*. Functional Materials, 2011. **18**(3): p. 298-303.
86. Stone, C.E., et al., *Structure of Bismuth Borate Glasses*. Physics and Chemistry of Glasses, 2000. **41**(6): p. 409-412.
87. Egorysheva, A.V., et al., *Vibrational Spectra of Crystals of Bismuth Borates*. Crystallography Reports, 2005. **50**: p. 127-136.
88. Walrafen, G.E., et al., *Low Frequency Raman Scattering from Vitreous and Molten B₂O₃*. The Journal of Chemical Physics, 1983. **79**: p. 3609-3620.
89. Hassan, A.K., et al., *Structural Changes of B₂O₃ Through the Liquid-Glass Transition Range: A Raman-Scattering Study*. Phys Rev B Condens Matter, 1992. **45**(22): p. 12797-12805.
90. Alderman, O.L., et al., *Liquid B₂O₃ up to 1700 K: X-Ray Diffraction and Boroxol Ring Dissolution*. J Phys Condens Matter, 2015. **27**(45): p. 455104.
91. Yano, T., et al., *Structural Investigation of Sodium Borate Glasses and Melts by Raman Spectroscopy*. Journal of Non-Crystalline Solids, 2003. **321**(3): p. 137-146.
92. Yano, T., et al., *Structural Investigation of Sodium Borate Glasses and Melts by Raman Spectroscopy. II. Conversion Between BO₄ and BO₂O - Units at High Temperature*. Journal of Non-Crystalline Solids, 2003. **321**(3): p. 147-156.
93. Yano, T., et al., *Structural Investigation of Sodium Borate Glasses and Melts by Raman Spectroscopy. III. Relation Between the Rearrangement of Super-Structures and the Properties of Glass*. Journal of Non-Crystalline Solids, 2003. **321**(3): p. 157-168.
94. Chryssikos, G.D., *Bond Length-Raman Frequency Correlations in Borate Crystals*. Journal of Raman Spectroscopy, 1991. **22**: p. 645-650.
95. Alderman, O.L.G., et al., *Temperature-Driven Structural Transitions in Molten Sodium Borates Na₂O-B₂O₃ : X-ray Diffraction, Thermodynamic Modeling, and Implications for Topological Constraint Theory*. The Journal of Physical Chemistry C, 2015. **120**(1): p. 553-560.
96. Kamitsos, E.I. and M.A. Karakassides, *Effect of Melt Temperature on Glass Structure*. Physics and Chemistry of Glasses, 1989. **30**(6): p. 235-236.
97. Kamitsos, E.I., *Infrared Spectroscopy of Glasses*, in *Modern Glass Characterization*, M. Affatigato, Editor. 2015, The American Ceramic Society and John Wiley & Sons, Inc. . p. 1-42.
98. Varsamis, C.P., A. Vegiri, and E.I. Kamitsos, *The Peculiar Role of Nonbridging Oxygen Atoms in Ionic Borate Glasses*. Physics and Chemistry of Glasses, 2004. **46**(2): p. 72-76.

99. Vegiri, A. and C.P. Varsamis, *Clustering and Percolation in Lithium Borate Glasses*. J Chem Phys, 2004. **120**(16): p. 7689-95.
100. Kamitsos, E.I., M.A. Karakassides, and A.P. Patsis, *Spectroscopic Study of Carbonate Retention in High-Basicity Borate Glasses*. Journal of Non-Crystalline Solids, 1989. **111**: p. 252-262.
101. Varsamis, C.P., E.I. Kamitsos, and G.D. Chryssikos, *Structure of Fast-Ion-Conducting AgI-doped Borate Glasses in Bulk and Thin Film Forms*. Physical Review B, 1999. **60**(6): p. 3885-3898.
102. Varsamis, C.P., E.I. Kamitsos, and G.D. Chryssikos, *Spectroscopic Investigation of AgI-doped Borate Glasses*. Solid State Ionics, 2000. **136-137**: p. 1031-1039.
103. Heyns, A.M., *The Vibrational Spectra of NbBO₄, TaBO₄, NaNb₃O₈, and NaTa₃O₈*. Spectrochimica Acta, 1990. **46A**(11): p. 1621-1628.
104. Ross, S.R., *The Vibrational Spectra of Some Minerals Containing Tetrahedrally Co-ordinated Boron*. Spectrochimica Acta, 1972. **28A**: p. 1555-1561.
105. Varsamis, C.P.E., et al., *Structural Investigation of Superionic AgI-Containing Orthoborate Glasses*. Journal of Non-Crystalline Solids, 2004. **345-346**: p. 93-98.
106. Button, D.P., et al., *Fast Li⁺ Ion Conductance in Chloroborate Glasses II - Diborates and Metaborates*. Solid State Ionics, 1981. **5**: p. 655-658.
107. Kamitsos, E.I. and M.A. Karakassides, *A Spectroscopic Study of Fluoride Containing Sodium Borate Glasses*. Solid State Ionics, 1988. **28-30**: p. 783-787.
108. Shinozaki, K., *Design of Crystallization of Oxyfluoride Glasses Based on the Local Structure of Fluorine*. Journal of the Ceramic Society of Japan, 2018. **126**(9): p. 684-692.
109. Kamitsos, E.I., M.A. Karakassides, and G.D. Chryssikos, *A Vibrational Study of Lithium Sulfate Based Fast Ionic Conducting Borate Glasses*. Journal of Physical Chemistry, 1986. **90**: p. 4528-4533.
110. Chryssikos, G.D., E.I. Kamitsos, and A.P. Patsis, *Effect of Li₂SO₄ On The Structure of Li₂O B₂O₃ Glasses*. Journal of Non-Crystalline Solids, 1996. **202**(3): p. 222-232.
111. Winterstein-Beckmann, A., et al., *Structure and Properties of Orthoborate Glasses in the Eu₂O₃-(Sr,Eu)O-B₂O₃ quaternary*. J Phys Chem B, 2015. **119**(7): p. 3259-72.
112. Winterstein-Beckmann, A., et al., *Structure–Property Correlations in Highly Modified Sr, Mn-Borate Glasses*. Journal of Non-Crystalline Solids, 2013. **376**: p. 165-174.
113. Denning, J.H. and S.D. Ross, *The Vibrational Spectra and Structure of Some Rare-Earth Borates*. Spectrochimica Acta, 1972. **28A**: p. 1775-1785.
114. Gu, G.X., et al., *In Situ Study on the Structural Transition in YBO₃ Through Raman Spectroscopy*. Materials Chemistry and Physics, 2011. **131**(1-2): p. 274-277.
115. Nair, R.G., et al., *Synthesis Conditions on the Nature of GdBO₃ Phase Formed*. ChemistrySelect, 2018. **3**(26): p. 7496-7506.
116. Plewa, J. and T. Jüstel, *Phase Transition of YBO₃*. Journal of Thermal Analysis and Calorimetry, 2007. **88**(2): p. 531.
117. Chryssikos, G.D., et al., *The Devitrification of Lithium Metaborate - Polymorphism and Glass-Formation*. Journal of Non-Crystalline Solids, 1990. **126**(1-2): p. 42-51.
118. Krogh-Moe, J.A.N., *Crystal Structure of Strontium Diborate*. Nature, 1965. **206**(4984): p. 613-613.

119. Ren, M., et al., *Structure and Phase Transition of GdBO₃*. Chemistry of Materials, 1999. **11**(6): p. 1576-1580.
120. Winterstein-Beckmann, A., et al., *Structure and Properties of Orthoborate Glasses in the Eu₂O₃–(Sr,Eu)O–B₂O₃ Quaternary*. The Journal of Physical Chemistry B, 2015. **119**(7): p. 3259-3272.
121. Drago, R.S., *Physical Methods in Inorganic Chemistry*. 1965, University of Illinois-Urbana: Reinhold Publishing Corp.
122. Zallen, R., *Optical and Electrical Properties*, in *The Physics of Amorphous Solids*. 1983, John Wiley & Sons, Inc. p. 252-296.
123. Ashcroft, N.W. and N.D. Mermin, *Solid State Physics*. 1976: Holt, Rinehart, and Winston
124. Möncke, D., *Metal Ions and their Interactions in Covalent to Ionic Glass Systems - a Spectroscopic Study*. 2017, Friedrich-Schiller-University Jena.
125. Herrmann, A., G. Völksch, and D. Ehrt, *Tb³⁺ as Probe Ion—Clustering and Phase Separation in Borate and Borosilicate Glasses*. Int. J. Appl. Glass Sci., 2019. **10**(4): p. 532-545.
126. Lee, S.K., et al., *Structure of Alkali Borate Glasses at High Pressure: B and Li K-edge Inelastic X-Ray Scattering Study*. Phys Rev Lett, 2007. **98**(10): p. 105502.
127. Vegiri, A. and E.I. Kamitsos, *Pressure-Induced Structural Transformations in Glass 0.3 Li₂O - 0.7 B₂O₃ : A Molecular Dynamics Study*. Physical Review B, 2010. **82**(5): p. 054114.
128. Colthup, N.B., L.H. Daly, and S.E. Wiberley, *CHAPTER 1 - VIBRATIONAL AND ROTATIONAL SPECTRA*, in *Introduction to Infrared and Raman Spectroscopy (Third Edition)*, N.B. Colthup, L.H. Daly, and S.E. Wiberley, Editors. 1990, Academic Press: San Diego. p. 1-73.
129. Nakamoto, K., *Theory of Normal Vibrations*, in *Infrared and Raman Spectra of Inorganic and Coordination Compounds*. 2008. p. 1-147.
130. Wilson, E.B., J.C. Decius, and P.C. Cross, *Molecular Vibrations : The Theory of Infrared and Raman Vibrational Spectra*. 1955, New York: McGraw-Hill.

Appendix

A1. Informal Derivation of Raman Intensity Expression [128-130]

The electric field component of a light wave incident on a molecule may be described by

$$E = E_o \text{Cos}(2\pi\nu t) \quad (17)$$

If the incident light induces a dipole in the molecule, the classical expression for the intensity of light scattered by the induced dipole is given by

$$I = \frac{16\pi^4}{3c^2} \nu^4 \mu_o^2 \quad (18)$$

Where c is the speed of light, ν is the frequency of the oscillation, and μ_o is the amplitude of the induced dipole μ

$$\mu = \mu_o \text{Cos}(2\pi\nu t) \quad (19)$$

The induced dipole, μ , is related to the electric field of the incident light by the polarizability, α , of the molecule

$$\mu = \alpha E \quad (20)$$

Substituting (17) into (20)

$$\mu = \alpha E_o \text{Cos}(2\pi\nu t) \quad (21)$$

The induced dipole arises from the molecule vibrating at a frequency ν_j . The frequency ν_j determines the displacement, q , of the nuclei at time t

$$q = q_o \text{Cos}(2\pi\nu_j t) \quad (22)$$

Where q_o is the amplitude of the vibration associated with frequency ν_j

During the process of the molecular vibration and hence change in the displacement q , the motion of the electrons may result in variation in the polarizability, α , which can be approximated linearly when the displacement is small

$$\alpha = \alpha_o + \left(\frac{\partial\alpha}{\partial q}\right) q \quad (23)$$

Inserting (22) into (23)

$$\alpha = \alpha_o + \left(\frac{\partial\alpha}{\partial q}\right) q_o \text{Cos}(2\pi\nu_j t) \quad (24)$$

Inserting (24) into (21)

$$\mu = \left(\alpha_o + \left(\frac{\partial\alpha}{\partial q}\right) q_o \text{Cos}(2\pi\nu_j t)\right) E_o \text{Cos}(2\pi\nu t) \quad (25)$$

Distributing the electric field expression across the polarizability expression

$$\mu = \alpha_o E_o \text{Cos}(2\pi\nu t) + \left(\frac{\partial\alpha}{\partial q}\right) q_o \text{Cos}(2\pi\nu_j t) E_o \text{Cos}(2\pi\nu t) \quad (26)$$

Rearranging terms in the 2nd term on the right-hand side and multiplying the quantity by 1 in the form of the fraction $\frac{2}{2}$,

$$\mu = \alpha_o E_o \text{Cos}(2\pi\nu t) + q_o E_o \left(\frac{\partial\alpha}{\partial q}\right) \frac{2}{2} \text{Cos}(2\pi\nu t) \text{Cos}(2\pi\nu_j t) \quad (27)$$

Applying the trigonometric identity $2 \text{Cos}(\theta)\text{Cos}(\phi) = \text{Cos}(\theta - \phi) + \text{Cos}(\theta + \phi)$ to (27)

$$\begin{aligned} \mu = & \alpha_o E_o \text{Cos}(2\pi\nu t) + \\ & q_o E_o \left(\frac{\partial\alpha}{\partial q}\right) \frac{1}{2} \{ \text{Cos}[2\pi(\nu - \nu_j) t] + \text{Cos}[2\pi(\nu + \nu_j) t] \} \end{aligned} \quad (28)$$

Distributing the term before the brackets

$$\begin{aligned} \mu = & \alpha_o E_o \text{Cos}(2\pi\nu t) + \\ & q_o E_o \left(\frac{\partial\alpha}{\partial q}\right) \frac{1}{2} \text{Cos}[2\pi(\nu - \nu_j) t] + q_o E_o \left(\frac{\partial\alpha}{\partial q}\right) \frac{1}{2} \text{Cos}[2\pi(\nu + \nu_j) t] \end{aligned} \quad (29)$$

The first term on the right-hand side corresponds to the light scattered at the same frequency as the incident light, that is, Rayleigh scattering. The second and third term correspond to Raman scattering where the light scattered is at a different frequency than the incident light. The second term, where the scattered frequency is lower than the incident frequency due to the molecule now vibrating in the j^{th} mode after being excited from a lower energy state is the Stokes scattering term. The third term, where the scattered frequency is higher than the incident frequency due to the molecule existing in an excited state prior to the event and returning to the ground state after the event, is the anti-Stokes term.

For spectroscopic measurements at room temperature, the number of Stokes scattering events is much greater than anti-Stokes due to *Maxwell-Boltzmann Statistics* dictating the majority of particles in a solid be in the ground state at room temperature. Thus, to investigate the vibrational modes of material through Raman scattering, the Stokes scattering portion of the intensity spectra should give the best signal due to the higher probability of a Stokes event occurring.

In a Raman spectrometer, filters are typically employed between the sample and the detector to block out the Rayleigh scattering due to the circumstance that the probability of a Raman scattering event occurring is on the order of 1 to 10^6 or less. So, if the attention

is focused only on the Stokes scattering, we can drop the 1st and 3rd term of (29) and write the induced dipole as

$$\mu_{Stokes\ scattering} = \frac{q_o E_o}{2} \left(\frac{\partial \alpha}{\partial q} \right) \text{Cos}[2\pi (\nu - \nu_j) t] \quad (30)$$

The classical expression in (18) describes the intensity of scattered light at the same frequency as the incident light (Rayleigh scattering). Let us ignore the constants in the relation that might change with the geometry of the instrument set-up and write simply,

$$I \propto \nu^4 \mu_o^2 \quad (31)$$

And then rewrite the expression in terms of Stokes scattering events

$$I_{Stokes} \propto (\nu - \nu_j)^4 \mu_o^2 \quad (32)$$

Considering (19) and (30) we have

$$\mu_o = \frac{q_o E_o}{2} \left(\frac{\partial \alpha}{\partial q} \right) \quad (33)$$

Inserting (33) into (32) we obtained

$$I_{Stokes} \propto (\nu - \nu_j)^4 \left(\frac{q_o}{2} \right)^2 E_o^2 \left(\frac{\partial \alpha}{\partial q} \right)^2 \quad (34)$$

The term $\left(\frac{q_o}{2} \right)^2$ is a constant and so can be dropped from the expression without voiding the validity.

Recall that E_o is the amplitude of the electric field of the incident radiation. The intensity of the incident radiation, I_o , is directly proportional to the square of the electric field amplitude. Incorporating this into (34) allows us to see the Raman scattering intensity is directly proportional to the incident light intensity.

$$I_{Stokes} \propto I_o (\nu - \nu_j)^4 \left(\frac{\partial \alpha}{\partial q} \right)^2 \quad (35)$$

In practice, an intensity measurement will include contributions of an ensemble of molecules present in a material. If there are N sites scattering at frequency ν_j then the measured intensity of the Stokes Raman scattering may be expressed

$$I \propto I_o (\nu - \nu_j)^4 N \left(\frac{\partial \alpha}{\partial q} \right)^2 \quad (36)$$

Where I_o is the intensity of the incident laser, ν is the frequency of the incident laser, ν_j is the frequency of the j^{th} vibrational mode, N is the number of sites scattering at frequency

ν_j , and $\left(\frac{\partial\alpha}{\partial q}\right)$ is the change in polarizability with respect to the normal coordinate. Moreover, expression (36) shows explicitly that the *change in polarizability* of a given vibrational mode determines its Raman activity, that is a mode is only Raman active when $\left(\frac{\partial\alpha}{\partial q}\right) \neq 0$. If for the j^{th} vibrational mode, $\left(\frac{\partial\alpha}{\partial q}\right) = 0$, then $I = 0$ and the mode is not Raman active.

A2. Glass Transition Temperature Determination in SYB Glasses

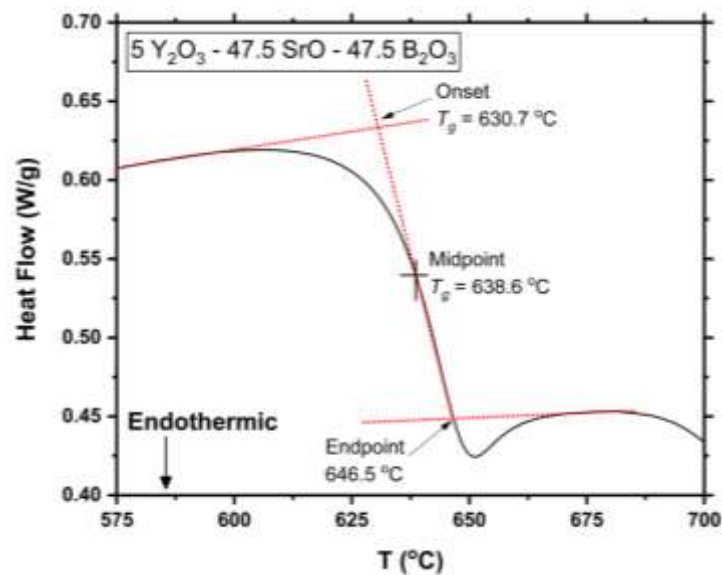


Figure A-1. T_g SYB with 5 mol% Y₂O₃

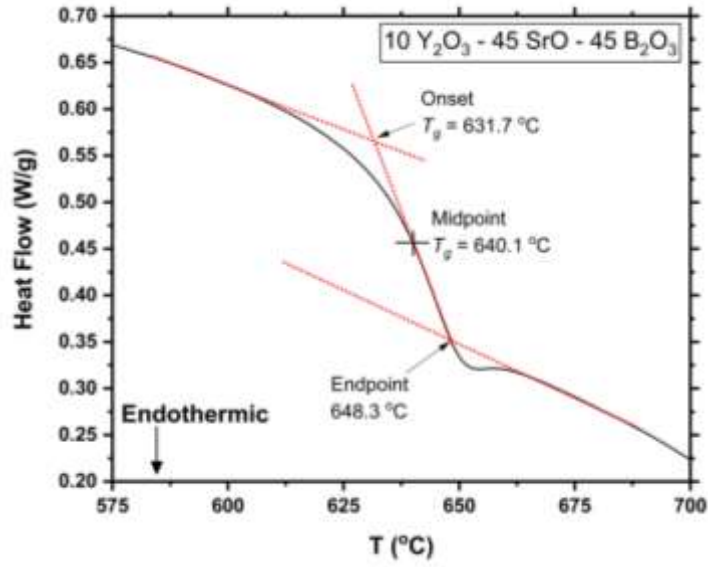


Figure A-2. T_g SYB with 10 mol% Y₂O₃

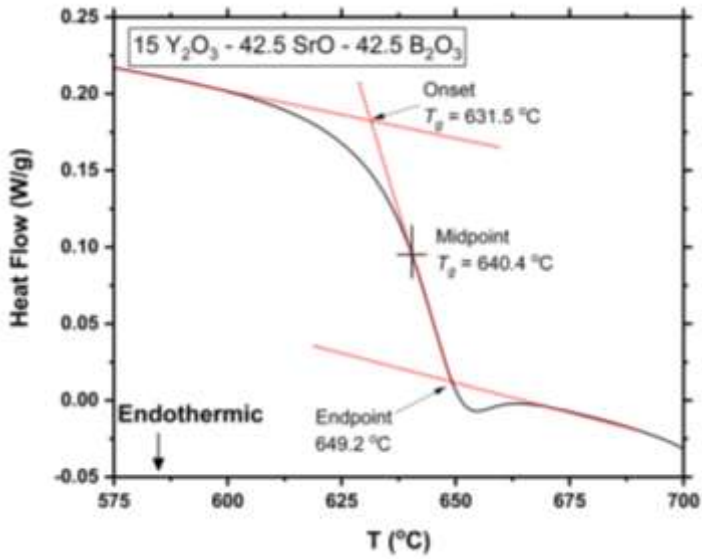


Figure A-3. T_g SYB with 15 mol% Y₂O₃

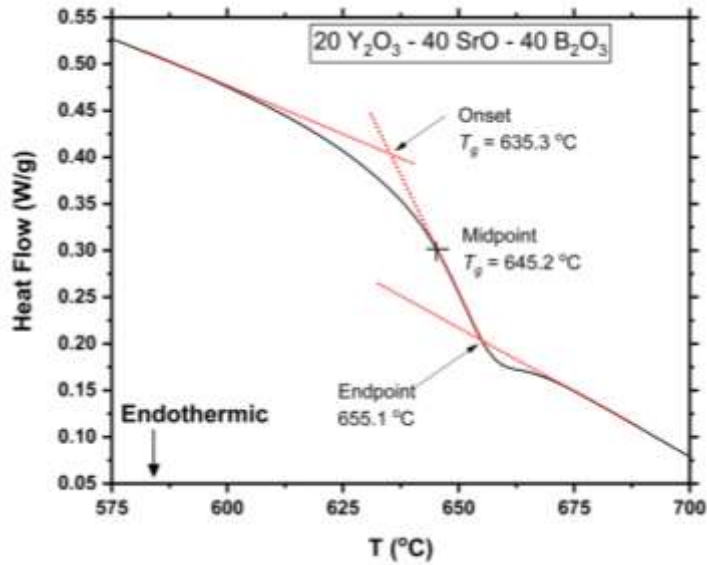


Figure A-4. T_g SYB with 20 mol% Y₂O₃

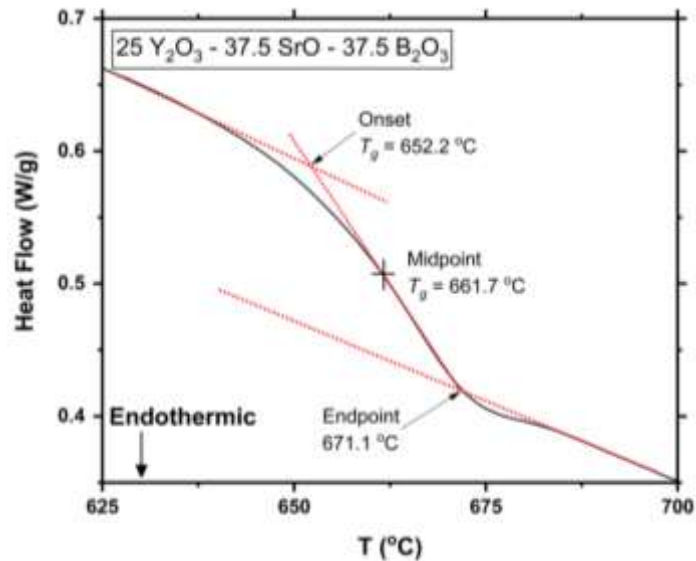


Figure A-5. T_g SYB with 25 mol% Y₂O₃

The trend observed using the intercept method was questioned due to the variation in the slope of the signal before and after the endothermic transition. To justify that the transition temperature increases with increasing yttria content and that the result cannot be due to any error associated with the changing slope of the signal, the derivatives of the DSC signal measurements were made (Figure A-6). The minimum in the derivative

corresponds to the inflection point of the endothermic transition and is therefore a strictly mathematical identification of the event. The values obtained in this way are compared to the intercept method values in Figure A-7. It is observed that, in all interpretations, the glass transition temperature increases.

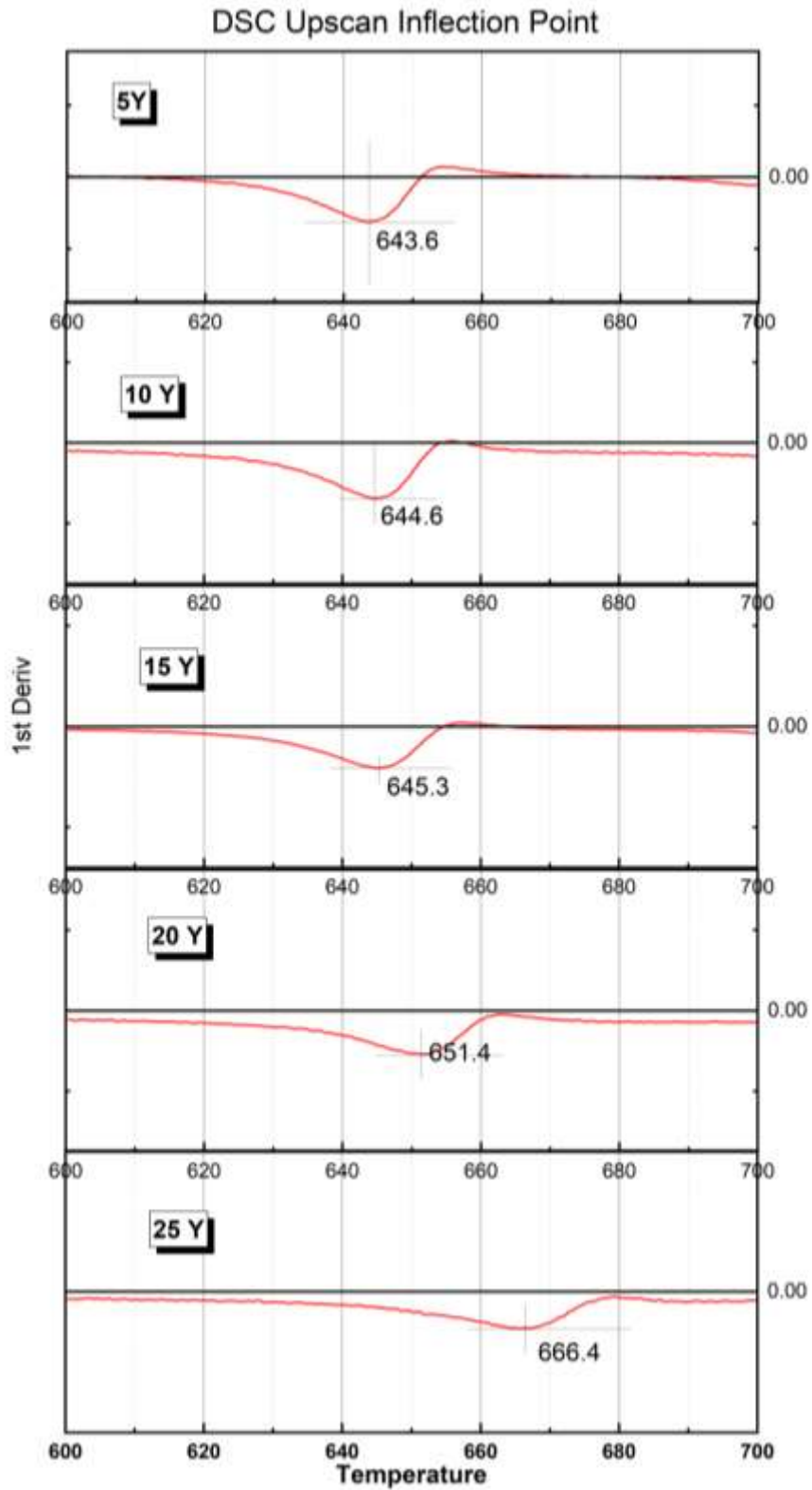


Figure A-6. First derivative of DSC signal for SYB glasses.

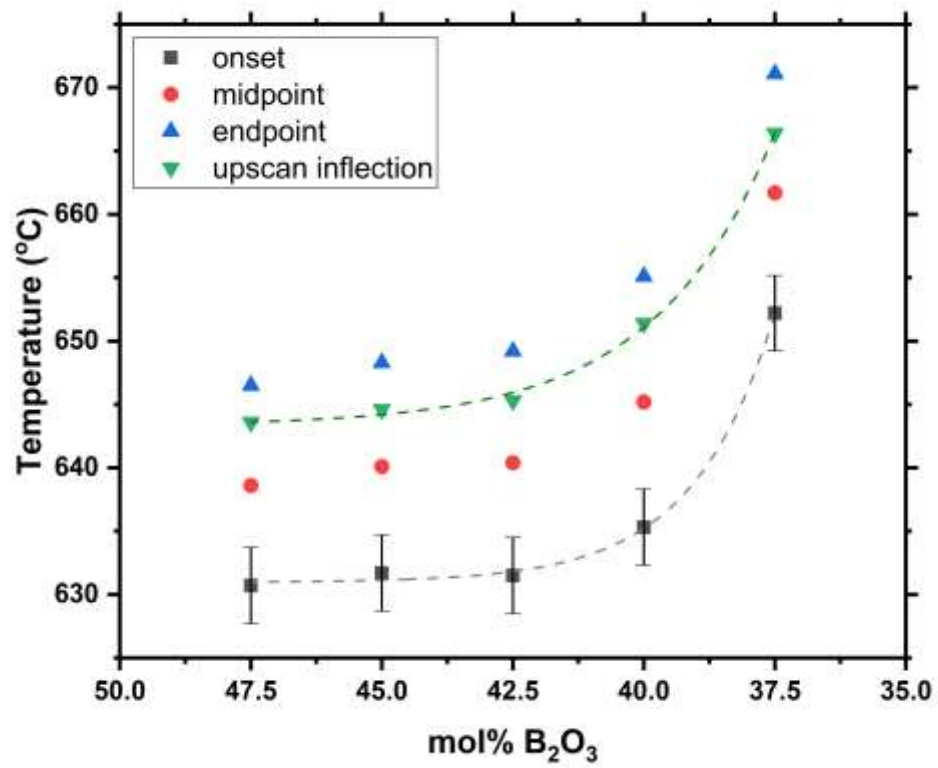


Figure A-7. Plot of different T_g values in strontium yttrium borate glasses. Error of ± 3 °C displayed on 'onset' data points.

A3. Contamination of Li_2CO_3

The lithium carbonate was contaminated with sodium-barium silicate glass particles. These elements are also observed in the LYB glasses in small quantities. The yttria and boric acid used do not show any impurities, the YBO_3 reference compound was analyzed and did not contain anything foreign.

Lithium Carbonate Contamination

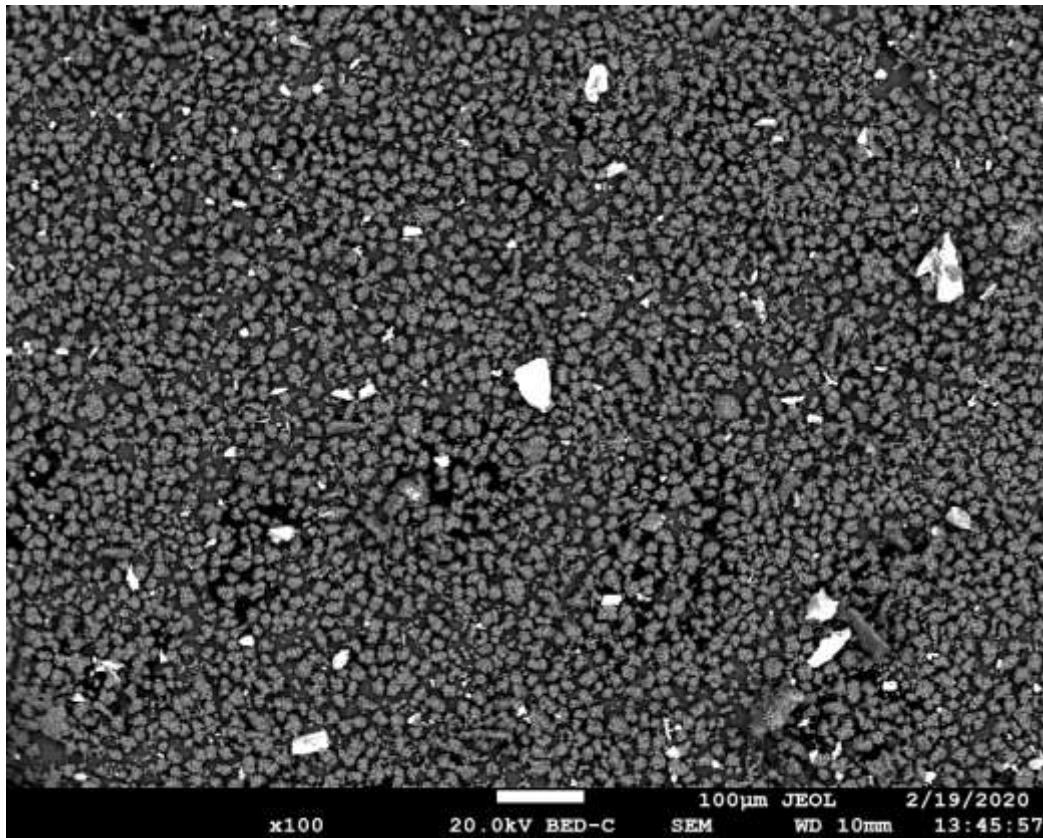


Figure A-8. Back Scatter image of the contaminated lithium carbonate raw material. The grey spots are lithium carbonate and the white spots are an impurity.

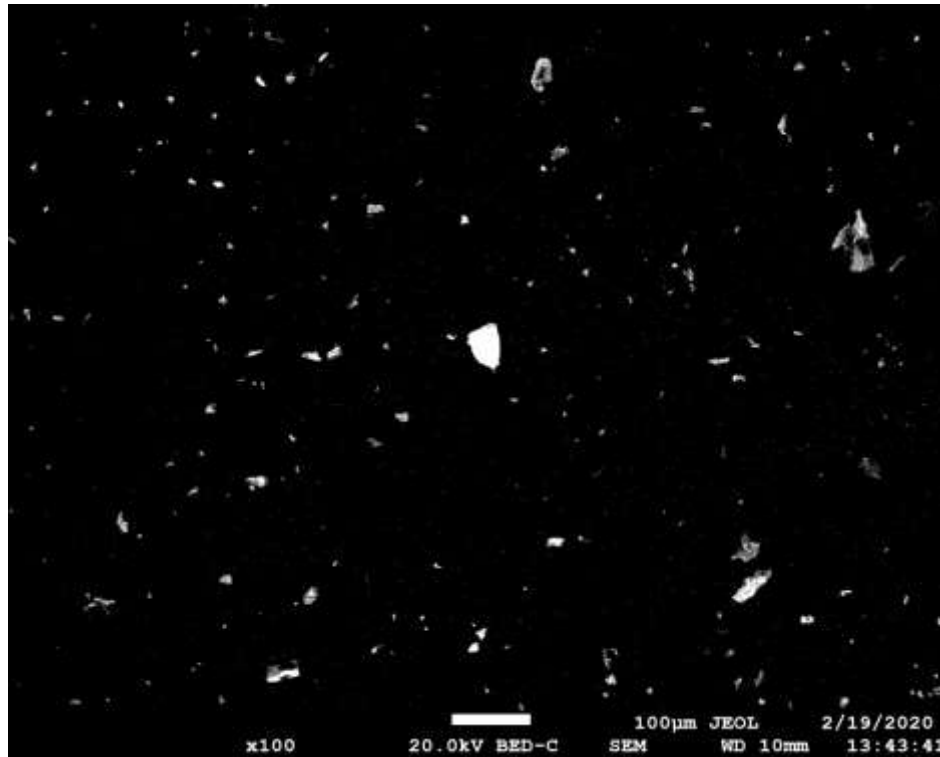


Figure A-9. Location of Figure A-8 with increased contrast to show impurity population.

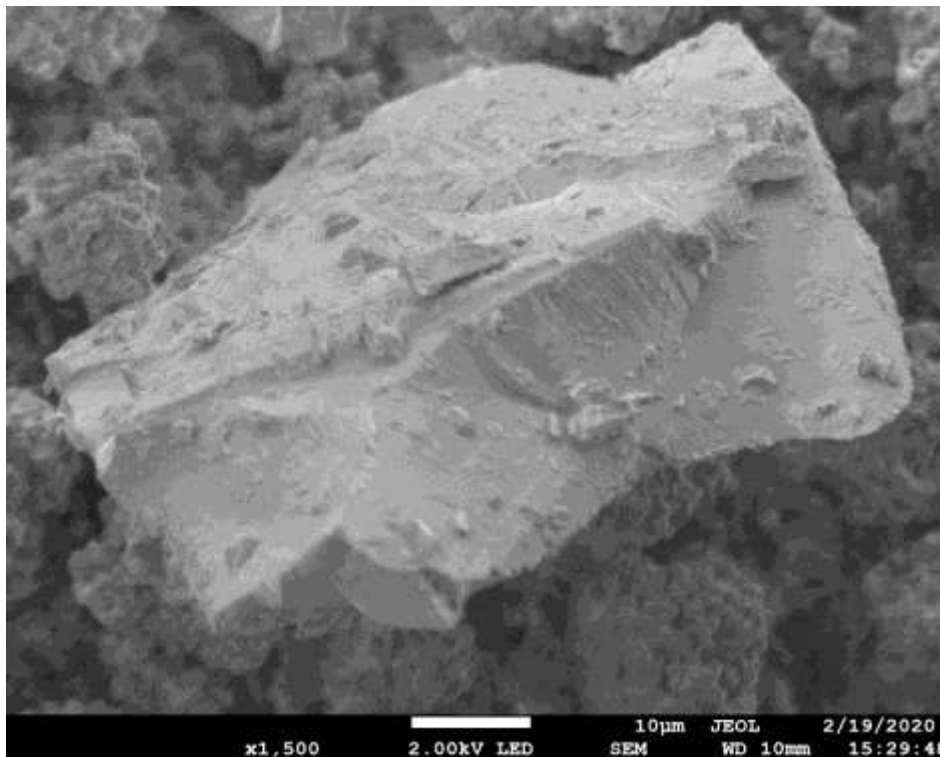


Figure A-10. SEM image of one of the larger impurities seen in Figure A-8.

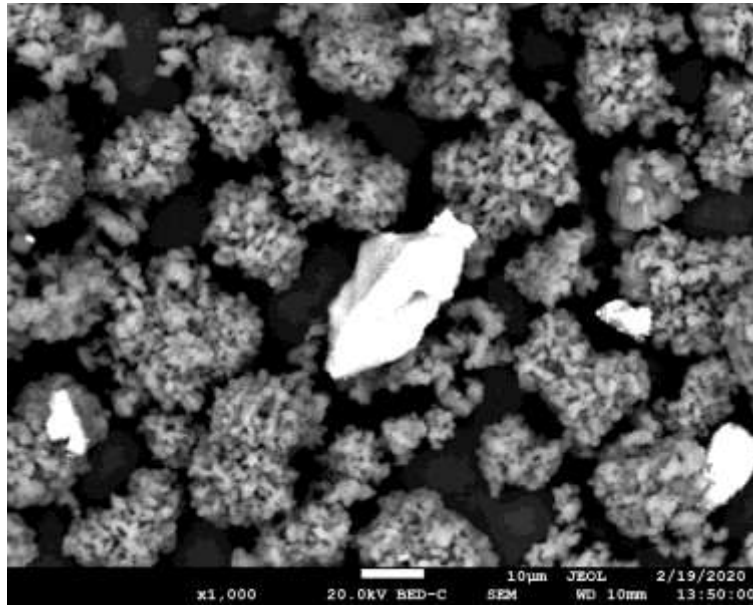


Figure A-11. Back Scatter image of typical contaminant (lithium carbonate is grey).

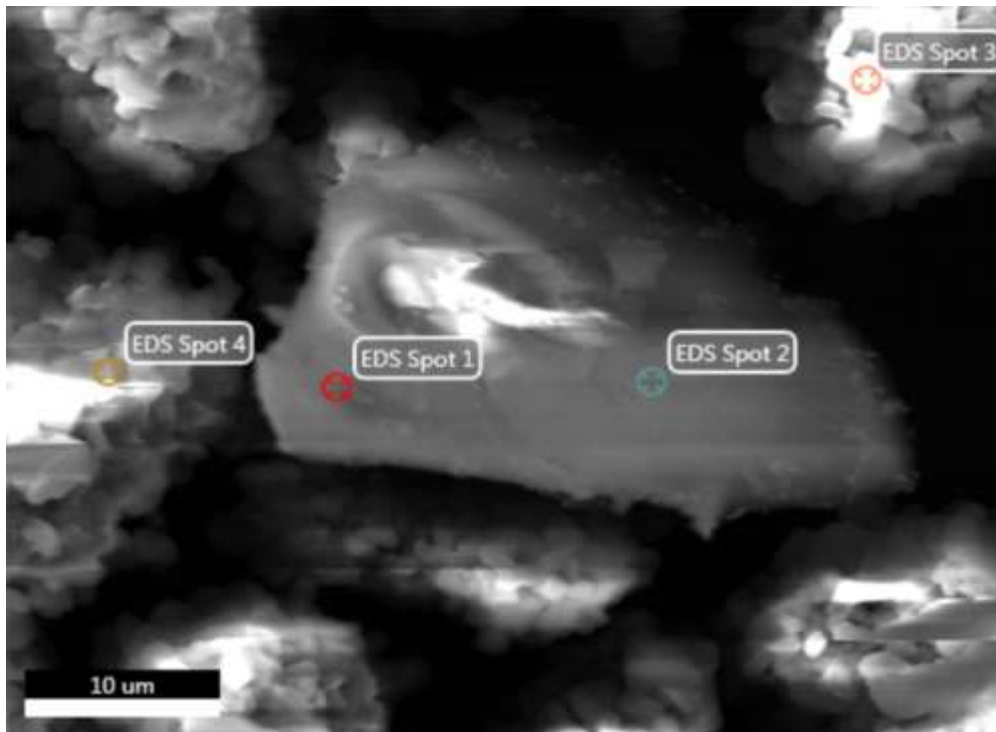


Figure A-12. EDS Site - Spot 1 and 2 are on one of the 'bright spots' observed in Figure A-11. Spots 3 and 4 are on the bulk of the material.

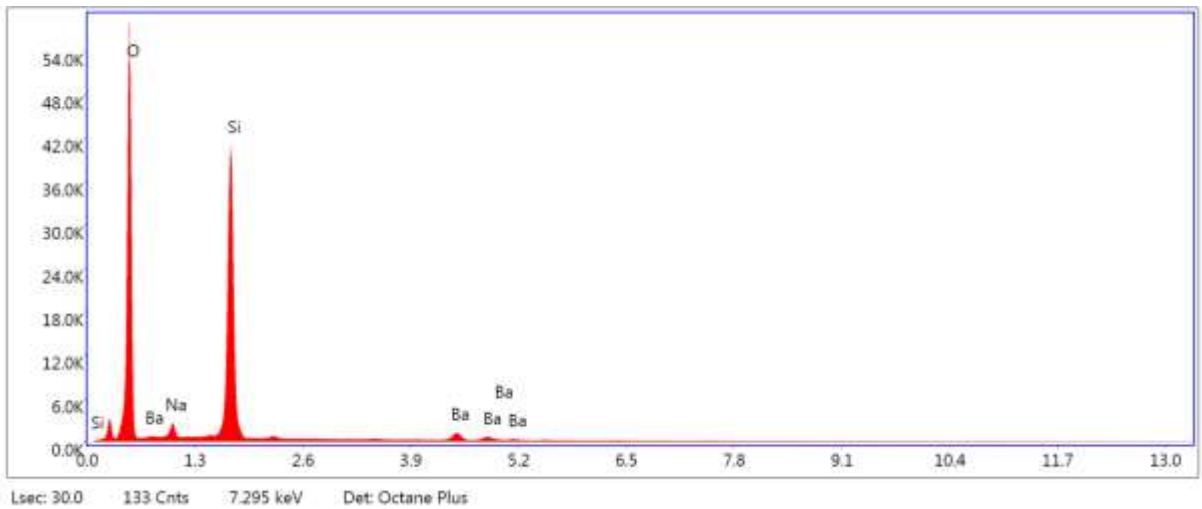


Figure A-13. EDS spectra for impurity site. EDS was performed on multiple spots and multiple sites) all showing the same elements of Si, O, Ba, Na.

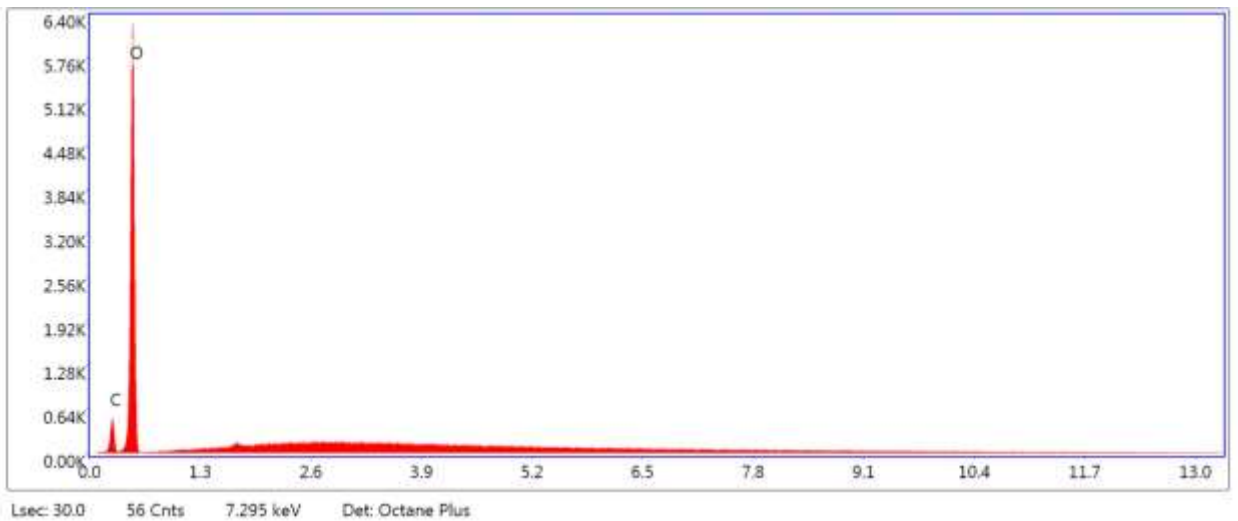


Figure A-14. EDS spectra for the majority of the material. The presence of only carbon and oxygen are taken as indication that this represents a lithium carbonate site.

LYB Glass Contamination

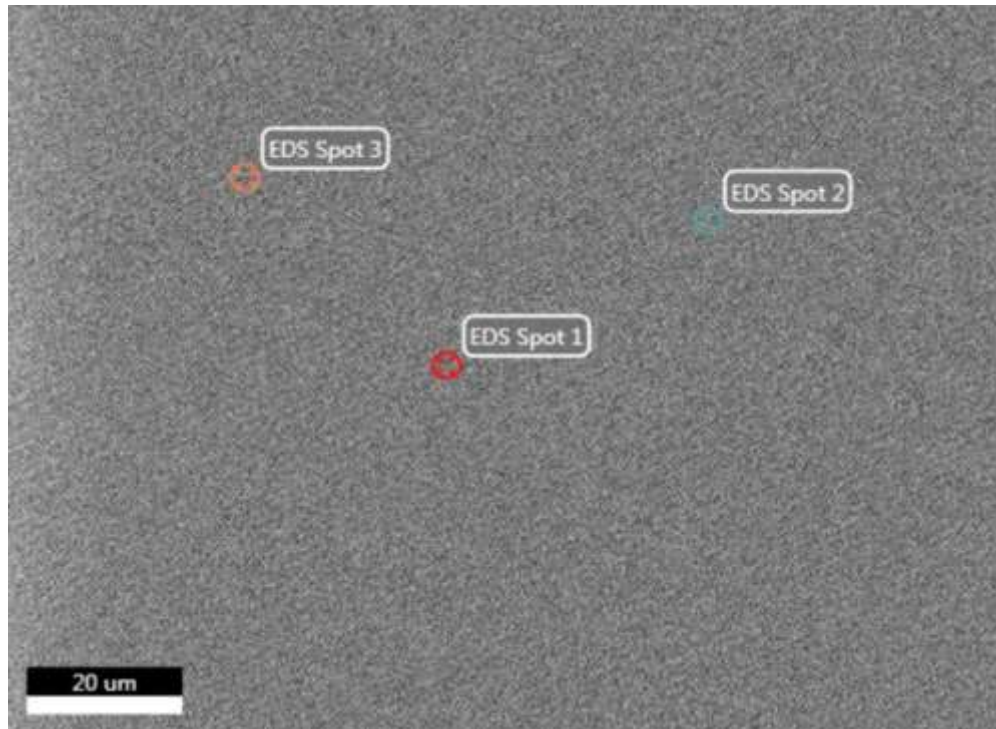


Figure A-15. Spots for EDS in LYB with nominal composition $57 \text{Li}_2\text{O} - 12 \text{Y}_2\text{O}_3 - 31 \text{B}_2\text{O}_3$

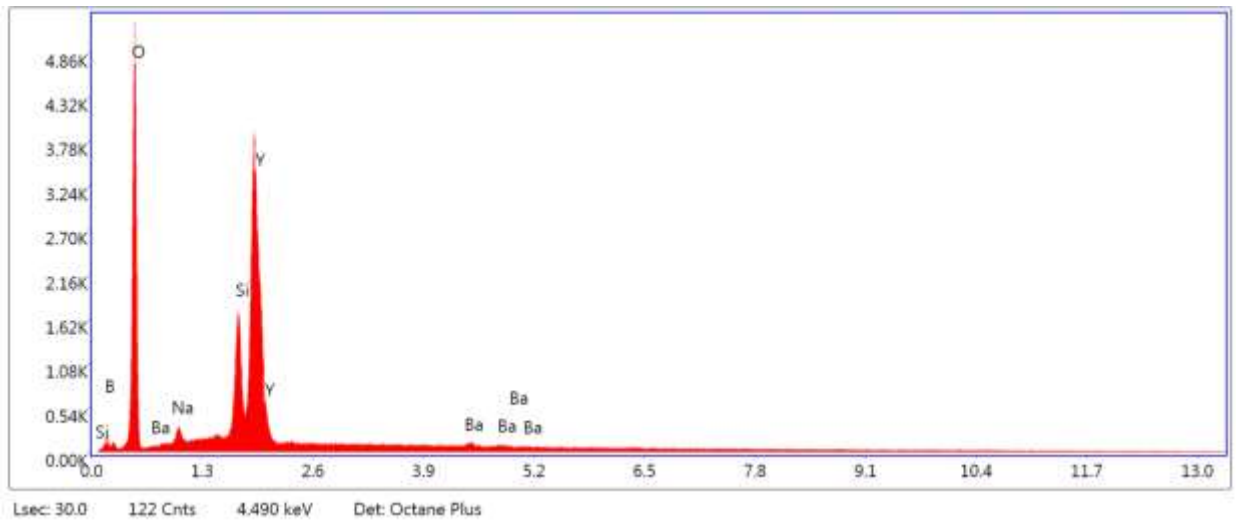


Figure A-16. All three spots had an EDS spectrum as the one shown above. The program quantified the atomic percentage of the impurities as Na= ~1%, Ba = 0.1%, Si = ~2-2.5%. Keep in mind the lithium content is not taken into consideration and no standards were prepared for this analysis.

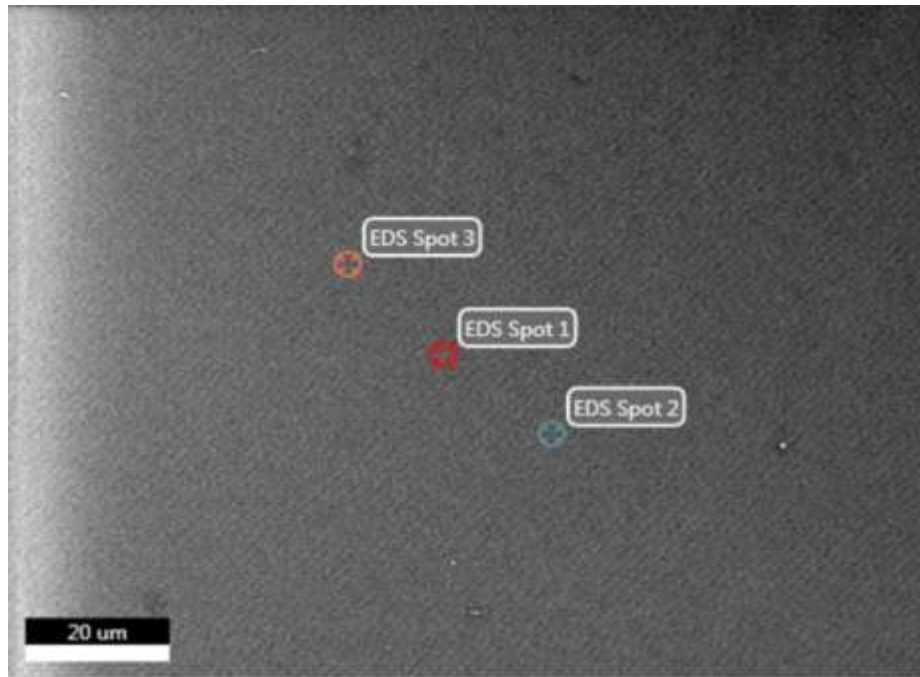


Figure A-17. Spots for EDS in LYB glass with nominal composition $48 \text{ Li}_2\text{O} - 18 \text{ Y}_2\text{O}_3 - 34 \text{ B}_2\text{O}_3$

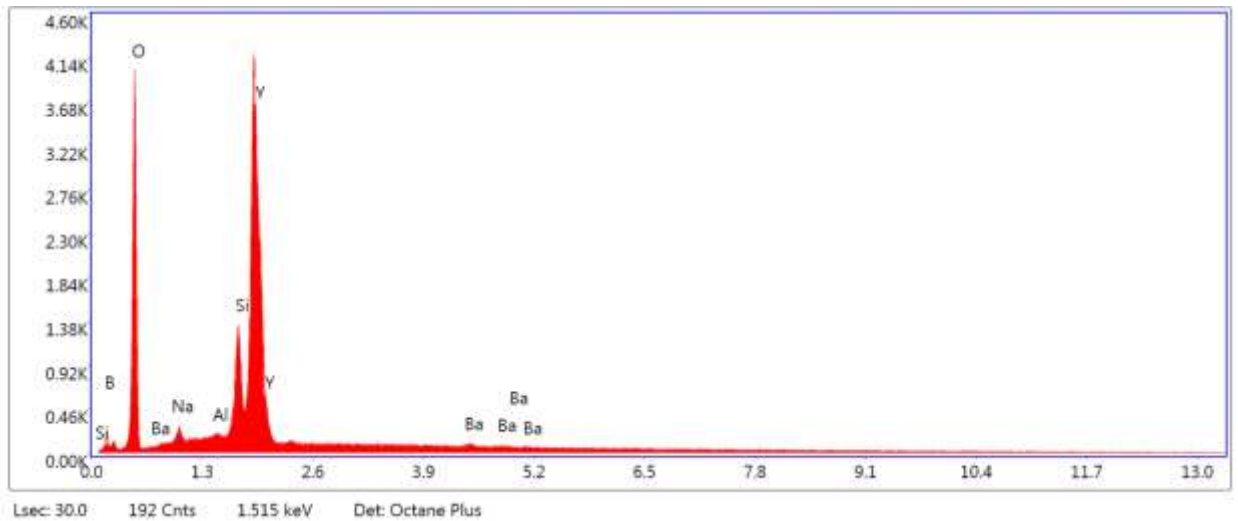


Figure A-18. All three spots had an EDS spectrum as the one shown above. The quantified impurity concentrations were slightly lower than the glass in Fig A-16 & A-16 which agrees with the lower Li_2CO_3 used in preparation of the glass. Additionally, a trace amount of aluminum was observed, on the order of 0.1 atomic%.

YBO₃

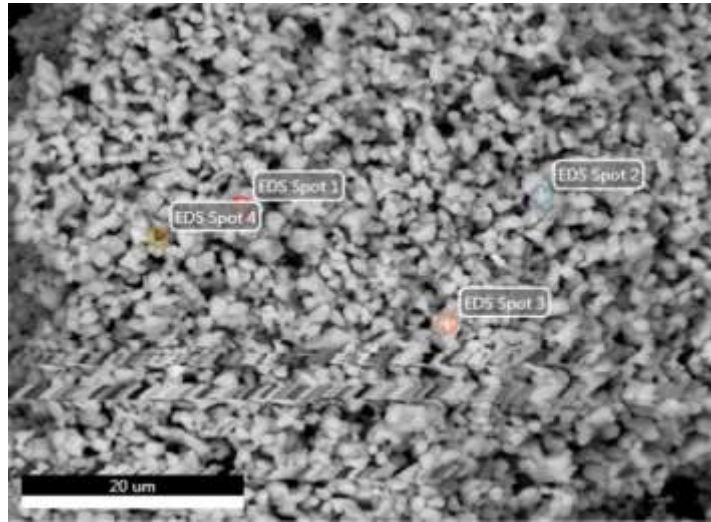


Figure A-19. YBO₃ crystalline compound for EDS. Closer investigations revealed the material to be homogenous. There was a small population of structures that appeared different than the bulk population. EDS at these locations showed the same spectra as the bulk so it was concluded these apparently different sites were YBO₃ with trigonal structure. Indeed, an NMR measurement of the material quantified about 5% of the borate units to be trigonally configured.

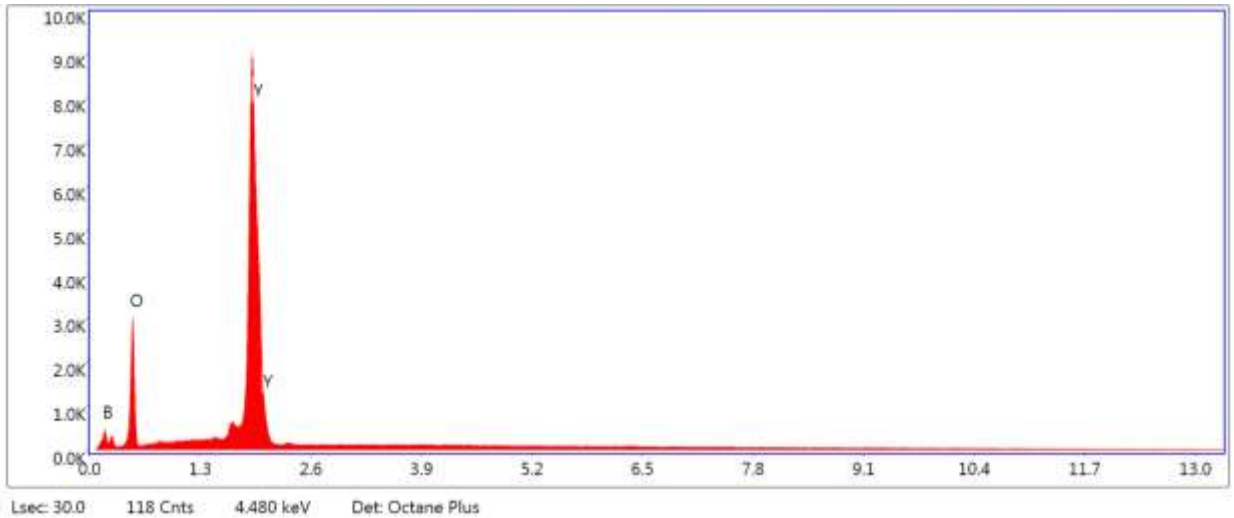


Figure A-20. EDS spectra that appeared at all spots investigated. No contaminants present- only B, O, and Y were detected at multiple sites. The boric acid and yttria used in the preparation of this compound were the same as used for the glasses.

A4. IR Spectra of Glasses with Contaminated Li_2CO_3

The normalized absorption coefficient spectra of the LYB glasses discussed in Section 3.2.1 are presented in Figure A-21. The deviation from the expected spectra lies in the fixed position of the tetrahedral boron band as the band loses relative intensity. The IR spectra of binary lithium borates has been digitized from their original publication and is shown in Figure A-22. In the binary lithium borate spectra, the 800-1150 cm^{-1} band merges into the 1150 – 1550 cm^{-1} .

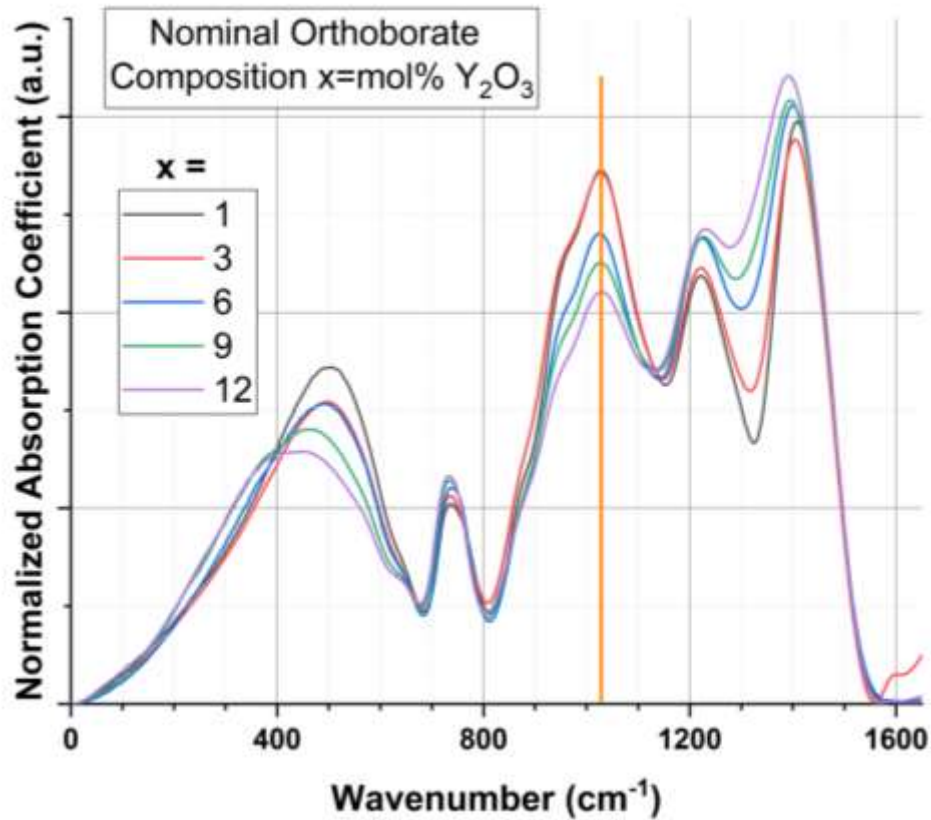


Figure A-21. IR spectra of contaminated LYB glasses.

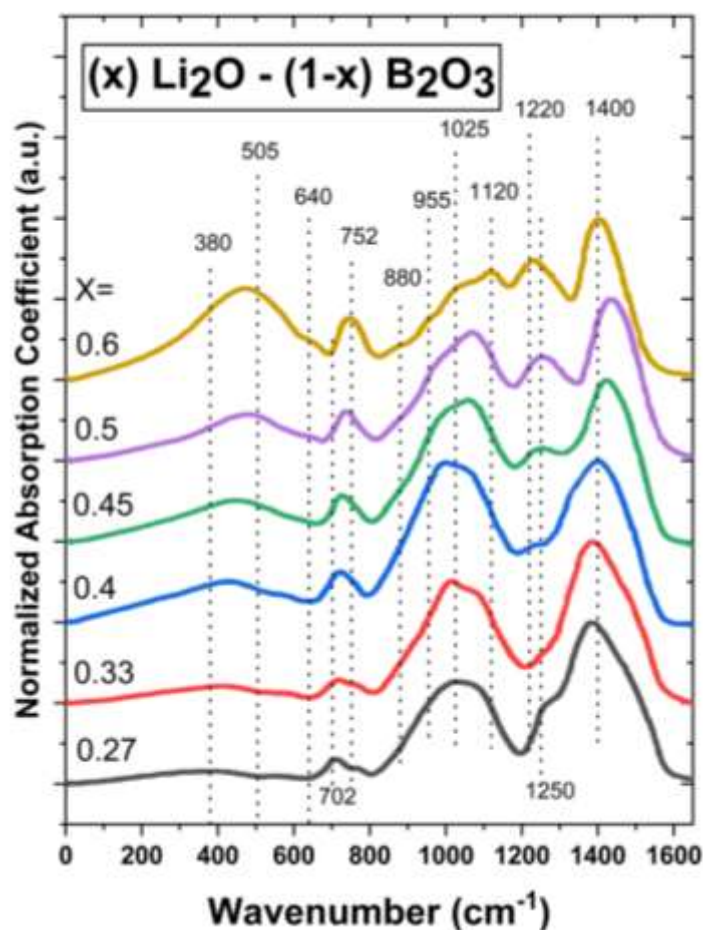


Figure A-22. IR spectra of binary lithium borate glasses from Kamitsos [68] .

Not only did this series show deviation from the expected modification route, but so too did a series of glasses (also made with the contaminated Li_2CO_3) where the nominal amount of Y_2O_3 was held constant and the Li_2O content was increased. Figure A-23 shows the IR spectra over the full frequency range and the tetrahedral band is highlighted in Figure A-24. In these spectra, it is seen that tetrahedral boron band shifts to lower frequencies with increasing modification as it loses relative intensity. Astonishingly though, for the highest Li_2O content, the relative intensity of the band increases. The characteristic bands of YBO_3 are highlighted in Figure A-24.

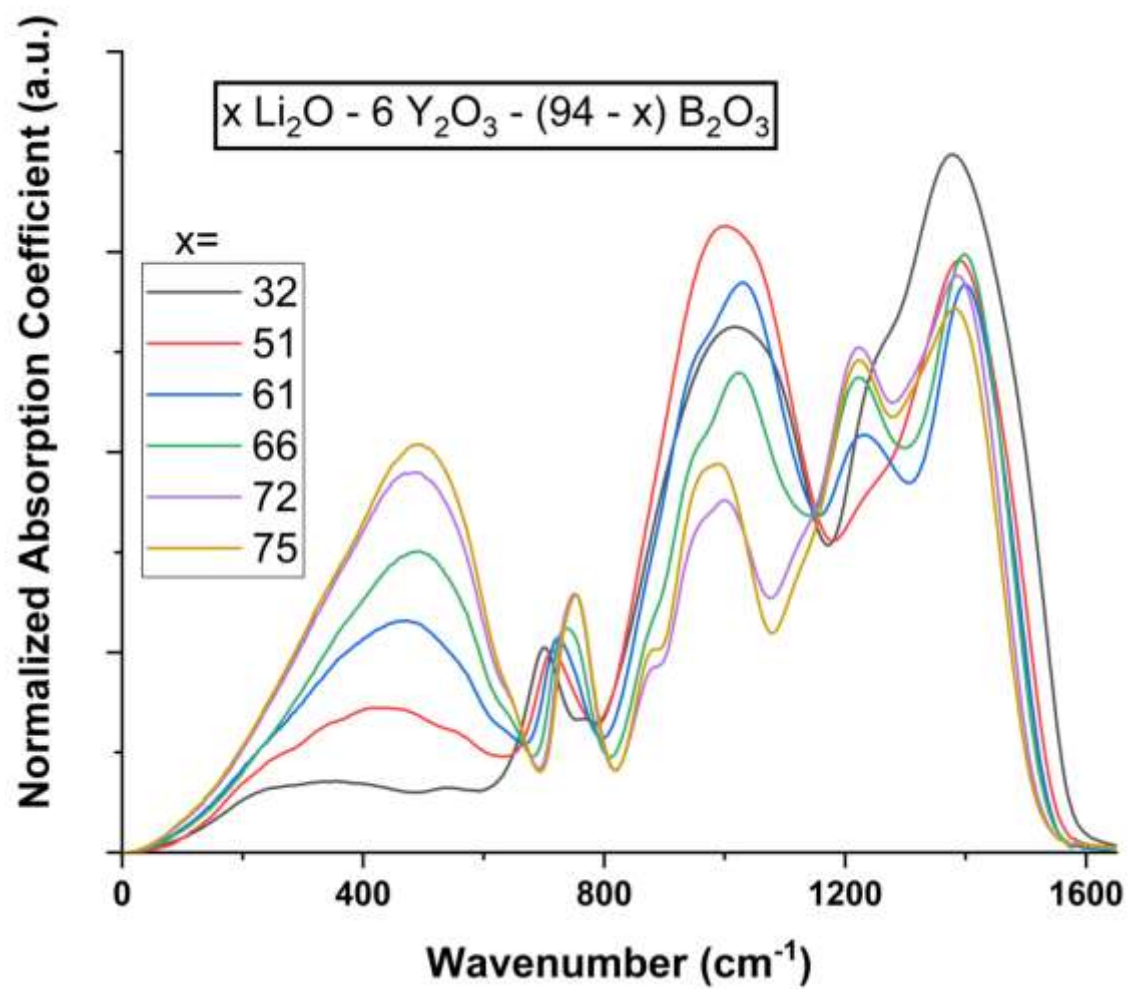


Figure A-23. IR spectra of a series of LYB glasses with constant Y_2O_3 in the nominal composition.

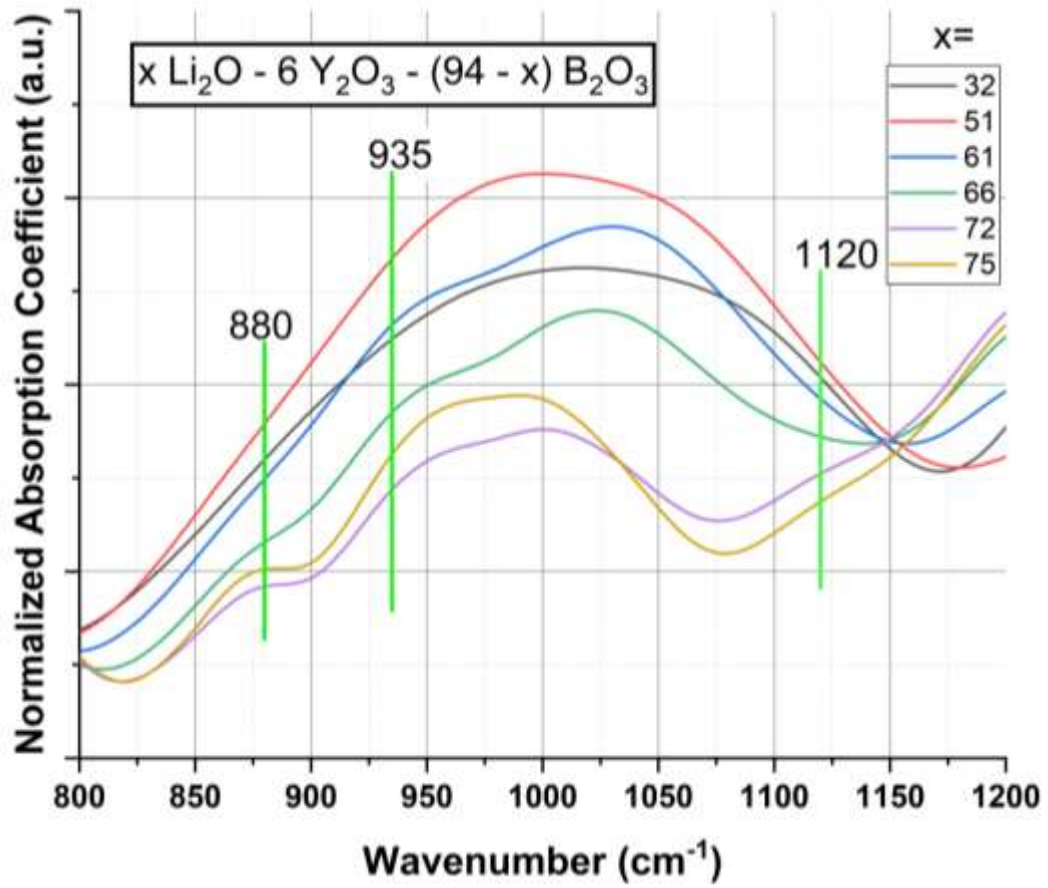


Figure A-24. IR spectra of a series of LYB glasses with constant Y_2O_3 in the nominal composition shown over the range 800-1200 cm^{-1} .